A Study of Two High Efficiency Energy Conversion Processes:

Semiconductor Photovoltaics and Semiconductor Luminescence Refrigeration

by

Songnan Wu

A Dissertation Presented in Partial Fulfillment
of the Requirements for the Degree
Doctor of Philosophy

Approved August 2010 by the
Graduate Supervisory Committee:

Yong-Hang Zhang, Chair
Jose Menendez
Fernando Ponce
Andrei Belitsky
Dieter Schroder

ARIZONA STATE UNIVERSITY

December 2010

ABSTRACT

As the world energy demand increases, semiconductor devices with high energy conversion efficiency become more and more desirable. The energy conversion consists of two distinct processes, namely energy generation and usage. In this dissertation, novel multi-junction solar cells and light emitting diodes (LEDs) are proposed and studied for high energy conversion efficiency in both processes, respectively.

The first half of this dissertation discusses the practically achievable energy conversion efficiency limit of solar cells. Since the demonstration of the Si solar cell in 1954, the performance of solar cells has been improved tremendously and recently reached 41.6% energy conversion efficiency. However, it seems rather challenging to further increase the solar cell efficiency. The state-of-the-art triple junction solar cells are analyzed to help understand the limiting factors. To address these issues, the monolithically integrated II-VI and III-V material system is proposed for solar cell applications. This material system covers the entire solar spectrum with a continuous selection of energy bandgaps and can be grown lattice matched on a GaSb substrate. Moreover, six four-junction solar cells are designed for AM0 and AM1.5D solar spectra based on this material system, and new design rules are proposed. The achievable conversion efficiencies for these designs are calculated using the commercial software package Silvaco with real material parameters.

The second half of this dissertation studies the semiconductor luminescence refrigeration, which corresponds to over 100% energy usage

efficiency. Although cooling has been realized in rare-earth doped glass by laser pumping, semiconductor based cooling is yet to be realized. In this work, a device structure that monolithically integrates a GaAs hemisphere with an InGaAs/GaAs quantum-well thin slab LED is proposed to realize cooling in semiconductor. The device electrical and optical performance is calculated. The proposed device then is fabricated using nine times photolithography and eight masks. The critical process steps, such as photoresist reflow and dry etch, are simulated to insure successful processing. Optical testing is done with the devices at various laser injection levels and the internal quantum efficiency, external quantum efficiency and extraction efficiency are measured.

To my wife and my parents

ACKNOWLEDGMENTS

I would like first to express my appreciation to my research supervisor, Dr. Yong-Hang Zhang for his guidance and supervision throughout my PhD study. I would also like to show my profound obligation to Dr. Ding Ding, Dr. Shuiqing Yu and Dr. Shane Johnson, for their generosity of time, valuable advice, and insightful discussions. I also wish to thank my other committee members, Dr. José Menéndez, Dr. Fernando Ponce, Dr. Andrei Belitsky, and Dr. Dieter Schroder for having interest in my work and giving me valuable advice. I would also like thank Dr. Dragica Vasileska for her valuable time and advice.

Over the years, I enjoyed and benefited from the generous help and friendship of my colleagues and co-workers. I want to thank them all for their team-support, numerous discussions, and valuable comments. I am indebted to Dr. Shumin Wang, Mr. Junliang Chen, Dr. Wei Du, Mr. Benjamin Green, Mr. Jin Fan, and Dr. Jin-Hui Tan. Furthermore, I would like to acknowledge CSSER's staff for their generous effort in providing a class cleanroom facility to students to carry out their research work.

Finally, I wish to especially thank my wife Yan whose love, support, and understanding enabled me to complete this work. I am also very grateful to my parents for showing me their love and affection throughout my life.

TABLE OF CONTENTS

LIST OF TABLES

Table Page

LIST OF FIGURES

Figure Page

Figure Page

Figure Page

Figure Page

Figure Page

Figure Page

Figure Page

PART I

I. INTRODUCTION OF SOLAR CELLS

This chapter briefly reviews the history of solar cells. Then the various types of solar cells are discussed based on their technology and material. The efficiency records and market shares for common solar cells are included. The fundamental loss mechanisms of p-n junction solar cells are analyzed and various approaches to decrease the losses are discussed.

1.1 History of Solar Cells

A solar cell is a device that converts sunlight into electricity through the photovoltaic effect, which is the generation of voltage by the device when it is exposed to light [1]. Although the photovoltaic effect was first discovered by French physicist A. E. Becquerel early in 1839 [2], it was not until 1954 when Chapin et al. invented the first practical Si single crystal based p-n junction solar cell with a ~6% conversion efficiency [3]. The first spacecraft equipped with the solar panels was the US satellite Vanguard 1, launched in March 1958 [4]. The solar cells used on Vanguard 1 had an efficiency of 9% and provided less than 1 watt power with six cells of 5×5 cm each [4, 5]. The solar cells on Vanguard 1 lasted for six years while the mercury battery lasted for just sixteen days [4], proving solar cells to be both practical and reliable. Since its first success on space satellite, the demand for solar cells has been tremendous and great efforts

have been devoted to reducing their cost and improving the efficiencies. To date, solar cells have been made using various technologies and employing different materials from organic thin films to single crystal semiconductors.

1.2 Various Types of Solar Cells and Their Efficiencies

At present, there are many types of solar cells made of various materials and the achievements in energy conversion efficiencies for different technologies in the past are summarized in Ref. 6. This section only tries to summarize the more popular solar cells, which can be divided into three different groups: i) single junction, ii) multi-junction, and iii) nano-structured cells.

1.2.1 Single Junction Solar Cell

Single junction solar cells have been investigated for a long time. Many different materials, such as single crystal, poly crystal and amorphous materials, have been used for single junction solar cells. Single crystalline Si is the most widely used and most successful material for solar cell applications. This is because of the good balance between material cost and energy conversion efficiency [1]. Although semiconductor-grade Si wafers are expensive, this type of solar cells typically has high efficiencies and good reliability. GaAs single crystal has also been used for single junction solar cell applications in the early years. In 1970 the first highly effective GaAs hetero-structure solar cells were

created by Zhores Alferov and his team in the USSR [7]. Although its efficiency is higher than that of crystalline Si based cells, GaAs single junction solar cells can hardly compete in the market due to higher substrate cost. And it was quickly replaced by the more efficient GaAs or Ge based multi-junction solar cells.

Although single crystalline solar cells are both efficient and reliable, they share one common drawback: high cost for the wafers and cell growth. Therefore, polycrystalline material based cells are being actively investigated due to their low material and manufacturing cost. Polycrystalline Si wafers made by sawing square Si cast or drawing flat thin films from molten silicon are the two most popular technologies used by the industry. However, cells made from polycrystalline Si usually have much lower efficiencies than their single crystalline counterpart. Besides polycrystalline Si, several amorphous materials have also been investigated due to their low cost, such as Si, CdTe, CIS (copper indium diselenide), and CIGS (copper indium gallium selenide). In this technology, the cost of semiconductor substrates is further reduced by depositing materials directly onto coated glass or stainless steel sheets in the form of thin films. Although the thin film cells have lower efficiencies compared with single and poly crystalline cells, they feature low cost and light weight. Moreover,

some of them are even flexible. But crystalline Si cells still dominate market with 80% market share compared with less than 20% market share of thin film cells [8]. And among the thin film cells, amorphous CdTe dominates the market [9]. Table 1.1 summaries the efficiencies achieved by various single junction solar cell technologies under 1 sun AM1.5G condition.

Table 1.1. The efficiencies achieved by various single junction solar cell technologies under 1 sun AM1.5G condition.

Technology	Research cell efficiency (%)	Commercial cell efficiency (%)
Single-crystalline Si	24.4 [10]	11-16 [8]
Ploy-crystalline Si	20.4 [11]	14 [12]
Amorphous Si thin film	9.5 [13]	5-6 [9]
Mono-crystalline GaAs	26.1 [14]	N.A.
CdTe thin film	16.5 [15]	11 [9]
CIGS thin film	19.9 [16]	10 [8]

1.2.2 Multi-Junction Solar Cell

The idea of multi-junction (MJ) cells was proposed by Jackson in 1955

and Wolf in 1960 [17, 18]. In a MJ cell, several single junction solar cells are vertically stacked together with decreasing bandgaps from the top. In 1982, the first monolithically integrated AlGaAs/GaAs double junction solar cell made by Research Triangle Institute (RTI) demonstrated a 15.1% efficiency [19]. At present, the efficiency records are held by the Ge- and GaAs-based triple junction solar cells. The inverted metamorphic InGaP/GaAs/InGaAs cell reaches 33.8% efficiency under 1 sun AM0 condition [20], while the lattice matched GaInP/InGaAs/Ge cell reaches 41.6% efficiency under 364 suns AM1.5D condition [21]. InP and Si substrates are also being actively investigated for MJ cells. For example, Si based double junction solar cells have been made using amorphous Si with bandgap about 1.7 eV and poly-crystalline Si with bandgap about 1.1 eV and conversion efficiency of 13.1% has been achieved [22].

Most of the high quality MJ cells today are grown by various epitaxial techniques on single crystalline substrates such as Ge or GaAs. The production and material cost can be extremely high compared with crystalline Si cells and other thin film cells. Therefore, these MJ cells were originally only used for space applications where the cost of the cells was just a small fraction of the total project cost. Recently, by the use of concentrating mirrors or lenses, the necessary surface area of the cells is greatly reduced and substituted by cheap

plastic. Therefore, the final cost of power production can be potentially lower than traditional single crystalline Si cells or even thin film cells if the conversion efficiency of MJ cells and solar concentration are both high enough. Therefore, MJ cells are among the most promising candidates for both ultra high conversion efficiency and low cost if used under high solar concentration.

1.2.3 Nano-Structured Solar Cell

Nano-structured solar cells have drawn a lot of attention for the past few years due to their promising low cost fabrication and high efficiency. At present, various nano-structures have been incorporated with many different solar cell technologies, such as traditional single and multi-junction cells, and the relatively new Schottky-barrier, dye-sensitized, organic, polymer cells. Among these different nano-structures, quantum well and quantum dot solar cells are the more popular types. Quantum well solar cells incorporate multiple quantum wells inside the intrinsic region of a p-i-n structure solar cell to enhance the absorption of longer wave length photons and therefore increase the current of the host cell. But usually the wells have negative effect on the working voltage due to lower band gap of the well material than the host material. Therefore, whether the conversion efficiency can be increased or not is a trade-off between increased working current and decreased voltage. Several different materials and

structures are being actively investigated, such as AlGaAs/GaAs, GaAsP/InGaAs, GaInP/GaAs, and InP/InGaAs, which are usually grown by various epitaxial techniques [23-25]. At present, the GaAsP/InGaAs strain balanced quantum well solar cell has achieved 26% efficiency under 200 suns AM1.5D condition [25].

Semiconductor quantum dots are utilized in solar cells in three major ways: i) Schottky-barrier solar cell; ii) polymer-semiconductor hybrid solar cell; iii) quantum dot sensitized solar cell [26]. The advantages of using quantum dots include: i) ability to tune the photo response and band offsets by tuning the quantum dot size [27]; ii) utilization of hot electrons before they thermally relax [28]; iii) generation of multiple carriers by a single photon to achieve quantum efficiency over unity and reduce thermal relaxation loss [29, 30]. With the advantages mentioned above, quantum dot solar cells may have the potential to exceed the 32% Shockley-Queisser efficiency limit of single junction solar cell [31]. Although the future of nano-structured solar cells is promising, the research is still at its infancy and the industrial production is far away.

1.3 Fundamental Theories of Single Junction Solar Cells

Although there are many kinds of solar cells as introduced in the previous chapter, they share two common principles: i) absorption of photons to create

electron-hole pairs; ii) separation of electron-hole pairs to generate voltage. Figure 1.1 schematically illustrates the band diagram of a p-n junction solar cell under solar radiation. The junction or active region has an energy bandgap of E_g. Photons with energy equal or above E_g can be absorbed to excite electron-hole pairs. Under the internal electric field, electron-hole pairs are separated and then extracted from n and p contacts, respectively.

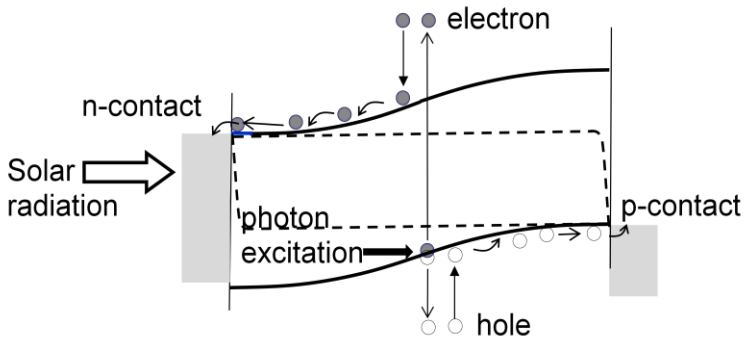

Fig. 1.1. Band diagram of p-n junction solar cell under solar illumination.

An equivalent circuit of the above p-n junction solar cell is shown in Fig. 1.2, where the constant current source I_L represents the photo-generated electrons/holes and is referred as to photocurrent [1]. Therefore, the ideal solar cell current is just the diode current subtracted by the photo current I_L given as [1]

$$I = I_s\left[\exp\left(\frac{qV}{kT}\right)-1\right]-I_L \quad , \tag{1.1}$$

where I_s is the dark current [1], given by

$$I_s = AqN_CN_V\left(\frac{1}{N_A}\sqrt{\frac{D_n}{\tau_n}}+\frac{1}{N_D}\sqrt{\frac{D_p}{\tau_p}}\right)\exp\left(-\frac{E_g}{kT}\right) \quad , \tag{1.2}$$

where A represents the cross-sectional area, N_C the conduction band density of states, N_V the valance band density of states, N_A the accepter concentration, N_D the donor concentration, D_n the electron diffusion coefficient, D_p the hole diffusion coefficient, τ_n the electron life-time, and τ_p the hole life-time.

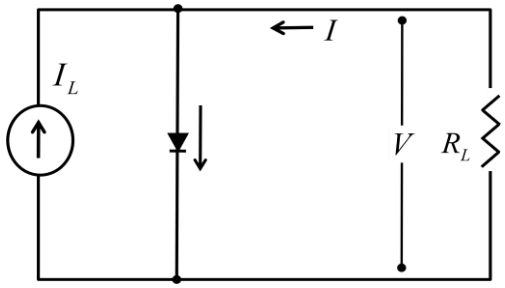

Fig. 1.2. Equivalent circuit of p-n junction solar cell under solar illumination.

This ideal solar cell I-V relation is plotted in Fig. 1.3 using Eq. 1.1, which shows several important quantities including short circuit current, open circuit voltage, optimum working current, optimum working voltage, and fill factor. When the output voltage is zero, the maximum output current is realized and

named short circuit current I_{sc}. Moreover, the recombination is negligible under short circuit condition and the short circuit current I_{sc} is just slightly smaller than the photo current I_L. When the output current is zero, the maximum output voltage is realized and named open circuit voltage V_{oc}. From Eq. 1.1, V_{oc} can be expressed as,

$$V_{oc} = \frac{kT}{q} \ln\left(\frac{I_L}{I_s} + 1\right) \quad . \tag{1.3}$$

From Eq. 1.3, V_{oc} can be increased either by increasing I_L or decreasing I_s. Increasing I_L means increasing the illumination intensity or in other words increasing the solar concentration. The dark current I_s can be affected by many factors and is expressed in Eq. 1.2. The material bandgap E_g and solar cell working temperature T play the most important roles in changing the dark current, since they are in the exponential.

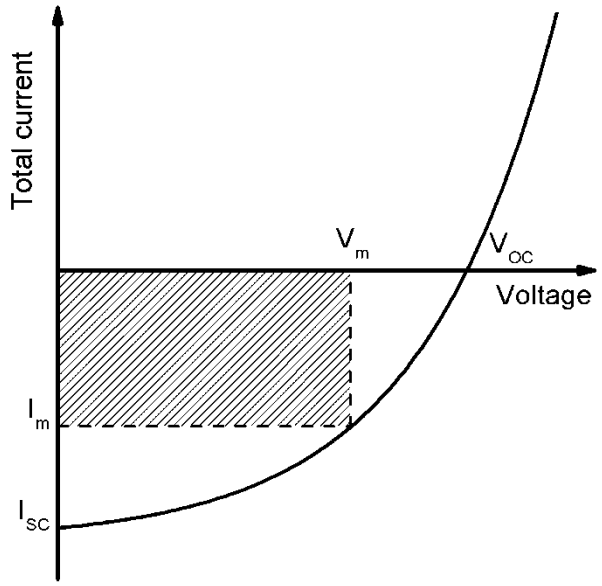

Fig. 1.3. I-V characteristic of an ideal solar cell under illumination.

It should be noted that no power could be extracted at short or open circuit conditions. Thus, by changing the load resistance, optimum working current I_m and voltage V_m can be achieved to give the largest power output

$$P\big|_{V=V_m, I=I_m} = -IV = I_L V - I_s V\left[\exp\left(\frac{qV}{kT}\right)-1\right] \quad . \tag{1.4}$$

At this optimum working condition, one has

$$\left.\frac{dP}{dV}\right|_{V=V_m} = I_L - I_s\left[\exp\left(\frac{qV_m}{kT}\right)-1\right] - I_s V_m \frac{q}{kT}\exp\left(\frac{qV_m}{kT}\right) = 0 \quad . \tag{1.5}$$

And V_m can be solved from Eq. 1.5. It is obvious that the largest power output is smaller than the product of I_{sc} and V_{oc}. The ratio $I_m V_m / I_{sc} V_{oc}$ is defined as the fill factor η and usually a large value is desired for high efficiency solar

cells.

1.4 Impact of Solar Spectrum and Energy Bandgap

In the above discussions the photo current is represented by a constant I_L, which oversimplifies the situation. Assuming one electron-hole pair is generated per absorbed photon, the photo current depends on the number of absorbed photons, which is related to solar concentration, air mass condition, material bandgap, absorption coefficient, cell thickness and reflection. Sun light is attenuated by the earth atmosphere before it reaches the ground and the degree of this attenuation is described by the "air mass". The "air mass" is defined as the secant of the angle between the sun and the zenith and measures the atmospheric path length relative to the minimum path length when the sun is directly overhead [1]. Figure 1.4 shows four spectra including AM0, AM1.5G, AM1.5D, and blackbody radiation at 5800K [32]. AM0 condition is close to the blackbody radiation at 5800K and represents the spectrum outside the earth atmosphere, which is used for space applications. AM1.5 (sun at 45^{o} above the horizon) condition represents a satisfactory energy-weighted average for terrestrial applications [1]. Moreover, AM1.5G and AM1.5D conditions describe the parallel and focused sun beams, which are relevant to un-concentrated and concentrated AM1.5 spectrum. Clearly due to the intensity difference, different

solar spectra will produce different photo currents. And the total illumination intensity is also different when calculating the conversion efficiency. For example, the intensity is 1360 W/cm^2 and 1000 W/cm^2 for AM0 and AM1.5G condition, respectively. The difference is mainly due to the absorption of the infrared region of solar radiation by the atmosphere. And solar cells usually have higher efficiencies under AM1.5G condition because the infrared part of solar radiation is absorbed by the air.

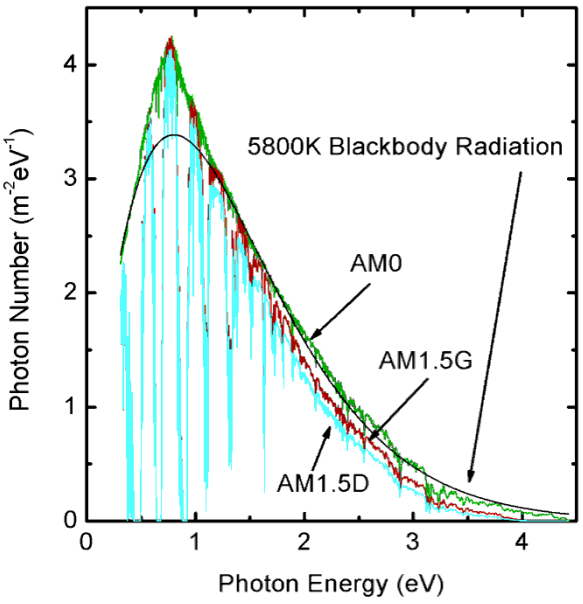

Fig. 1.4. Various solar spectra for different air mass conditions (AM0, AM1.5G, AM1.5D, blackbody radiation at 5800K) [32].

The solar cell bandgap determines the number of photons that could be

absorbed. Cells with smaller bandgaps produce more photo current but smaller working voltage while cells with larger bandgaps produce less photo current but higher working voltage. Therefore, an optimum bandgap exists for maximum conversion efficiency as illustrated in Fig. 1.5 [31], which shows that Si and GaAs bandgaps are very close to the optimum value. Furthermore, real solar cells usually give efficiencies lower than theoretical values due to various recombination losses, contact and shunt resistance, contact shadowing and front surface reflection.

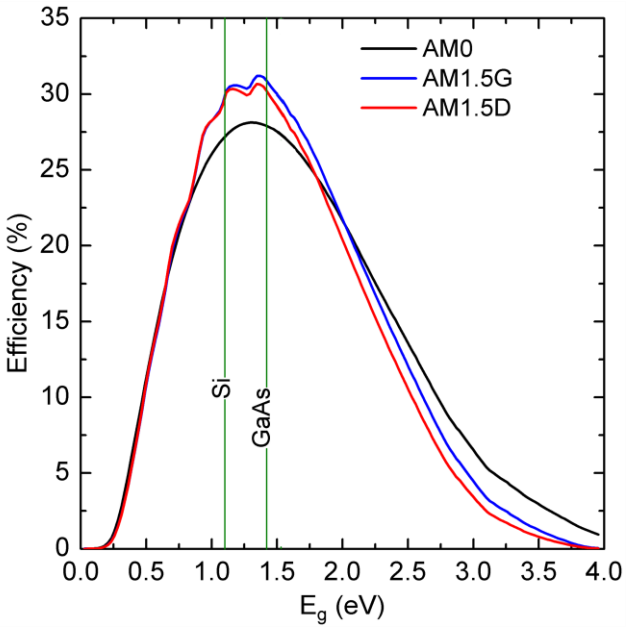

Fig. 1.5. Ideal solar cell conversion efficiency for different solar spectra [31].

1.5 Fundamental Loss Mechanisms for Single Junction Solar Cells

As seen in Fig. 1.5, even for solar cells with close to optimum bandgaps, such as Si and GaAs, their theoretical conversion efficiencies are still lower than 35% and real cells have even lower efficiencies. There are several fundamental loss mechanisms associated with single junction solar cells as described in Fig. 1.6, including transmission loss, thermal relaxation loss, recombination loss and spatial relaxation loss. Figure 1.7 schematically shows contribution of these losses in terms of area and the total area represents the input solar radiation.

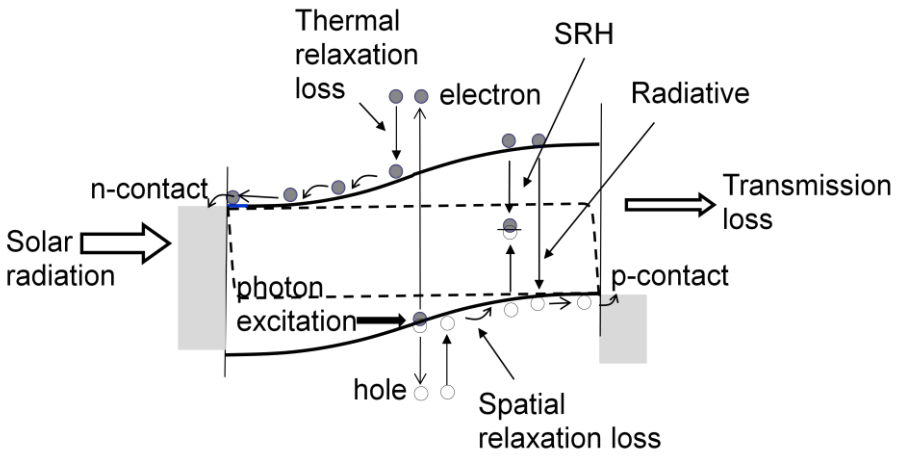

Fig. 1.6. Schematic diagram of fundamental loss mechanisms in a p-n junction solar cell.

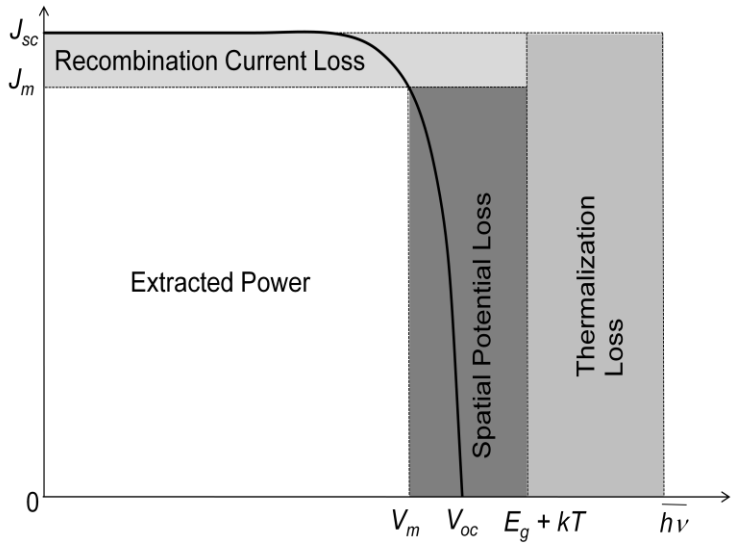

Fig. 1.7. Contribution of various fundamental loss mechanisms. The total area represents the input solar radiation.

The transmission loss is due to the transmission of photons with energies below the bandgap, which cannot be absorbed by the cell. For example, GaAs has a bandgap of 1.42 eV and 34% of the radiation power is below this bandgap for AM1.5G spectrum. The thermal relaxation loss is due to the difference between average absorbed photon energy $\overline{h\upsilon}$ and bandgap. An electron-hole pair is generated by a photon with energy greater than the bandgap. Initially, the energy difference between the electron and hole is equal to the photon energy and larger than the bandgap energy. Then the carriers quickly relax to their corresponding band edges through thermal relaxation and the extra energy above

the bandgap becomes heat. It should be noted that the average carrier energy at the band edge is actually higher than the bandgap by about kT at low injections [33]. This loss mechanism accounts for about 20% loss for GaAs under AM1.5G condition. One important reason for such a large transmission and thermal relaxation loss is the nature of broad solar spectrum.

The spatial relaxation loss is due to the potential energy loss when carriers travel from the junction region to the contact. This results in a smaller working voltage than the cell bandgap energy divided by electron charge. For example, GaAs has a bandgap of 1.42 eV while the cell working voltage is usually below 1 V. The difference is the built in voltage and this voltage creates an electric field that helps to extract the carriers. In the case of GaAs, this loss accounts for about 11% loss under AM1.5G condition.

The recombination loss is due to the carrier loss through various recombination mechanisms, including Shockley-Read-Hall (SRH), radiative, and Auger recombination. For high quality materials, this loss usually accounts for just a few percent efficiency reductions. In summary, the above four fundamental losses already account for more than 65% efficiency loss for typical GaAs single junction solar cells.

It is interesting to note that if the recombination rate is forced to be zero,

no electric field is needed to extract the carriers. Then the spatial relaxation loss inside the semiconductor becomes zero. And the only spatial relaxation loss happens at the contacts. Therefore, the working voltage will just be slightly below the bandgap divided by electron charge. However, if the recombination is strong in the semiconductor, a stronger electric field is needed to collect the carriers. And this will result in a smaller working voltage and thus smaller conversion efficiency. Therefore, decreasing the recombination loss can also help to decrease spatial relaxation loss.

1.6 Methods to Reduce Losses in Solar Cells

The above discussions reveal the four fundamental loss mechanisms of single junction solar cells. Generally, it is difficult to reduce the transmission and thermal relaxation loss in single junction solar cells. However, multi-junction solar cells are able to achieve low transmission and thermal relaxation loss, which will be introduced in the next chapter. Moreover, a number of techniques have been developed to reduce the recombination loss and therefore the spatial relaxation loss. Moreover, real solar cells carry many more practical issues which further limit the energy conversion efficiency. These issues include i) contact resistance, ii) shunt resistance, iii) contact shadowing, and iv) front surface reflection. The techniques to overcome these limitations

are discussed in detail as follows.

1.6.1 Techniques to Reduce Recombination Losses

Generally, all three recombination mechanisms, namely SRH, radiative and Auger recombination, can happen in a semiconductor solar cell. However, it should be noted that even under high solar concentration, the carrier density in a solar cell is still several orders of magnitude lower than that in quantum well lasers or LEDs. This is because the thickness of quantum wells is usually just a few nano-meters, while that of solar cells is usually above a few micrometers. Therefore, the SRH recombination dominates in most p-n junction based solar cells since it is a single carrier event. The SRH recombination can happen inside the semiconductor, at the semiconductor surface, and close to contacts. Thus, different techniques are used to reduce the SRH recombination at different places.

The SRH recombination inside the semiconductor is usually caused by the material defects formed during growth. Therefore, high quality epitaxial materials grown on single crystalline substrates are usually used and growth conditions are tuned to minimize the defect density. Moreover, SRH recombination can also be decreased by shortening the time carriers stay inside the solar cell. For that purpose, a lightly doped layer is often inserted between the p and n-type thin layers of the solar cell. The lightly doped layer helps to

extend the electric field across a broader region, which can sweep the carriers out in a relatively short time and thus reduce the probability of recombination. This lightly doped layer also minimizes the free-carrier absorption due to the low doping level.

The non-radiative recombination at the semiconductor surface is usually caused by surface defects formed during processing. A typical way to reduce surface recombination is to deposit or grow a passivation layer on top of the solar cell. For example, a thin SiO_2 layer can be used for Si solar cells. Moreover, a window layer and back-surface-field (BSF) layer are often added to the front and back surface to further reduce surface recombination as shown in Fig. 1.8. Figure 1.9 shows the band diagram of this structure. The window layer can be of the same material as the solar cell junction region and has significantly higher doping level. The potential barrier formed by the high doping level prevents the holes from getting to the top n contact. Therefore, the top side surface recombination can be minimized. The BSF layer follows the same concept to prevent electrons from getting to the bottom surface. If the window layer is of the same material as the junction, some of the sun light is absorbed in the layer and the photo generated electron-hole pairs can still recombine there. And due to the high doping level in the window layer, free-carrier absorption also needs to

be considered. Therefore, a wider bandgap material is usually more desirable for the window layer with moderate doping level as long as a potential barrier in the valance band can be formed. And of course, the window layer material has to be lattice-matched to the substrate in order to minimize interface defects and recombination.

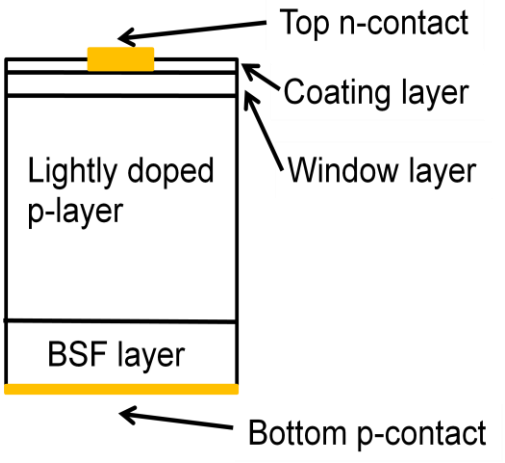

Fig. 1.8. Single junction solar cell structure with window, intrinsic and BSF layer.

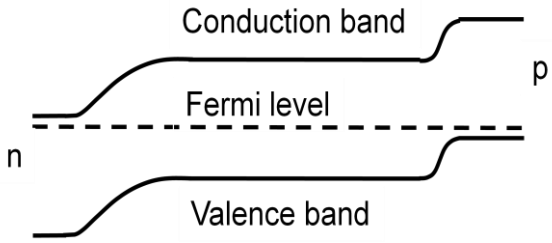

Fig. 1.9. Band diagram of single junction solar cell with window, intrinsic and BSF layer.

Defects may be formed beneath contacts caused by metal-semiconductor inter diffusion during contact deposition and subsequent annealing. Therefore, an effective way to reduce the recombination is to reduce the back contact area.

A structure called passivated emitter, rear locally diffused (PERL) cell is developed for Si single junction cells [10]. In this structure, the back surface is firstly passivated with SiO_2. Then back contacts are made through small holes in the oxide layer. This results in small total back contact area and therefore low average defect density. Moreover, the minority carrier recombination is further suppressed by the potential barrier formed using a locally highly doped region close to the contact. A conversion efficiency of 25% is realized using a Si cell by this structure under 1 sun AM1.5G condition [34].

1.6.2 Techniques to Reduce Contact Resistance

Contact resistance in solar cells dissipates power as heat according to the I^2R law. The ideal I-V characteristic of the solar cell is modified by this extra resistance, given as

$$I = I_s \left\{ \exp\left[\frac{q(V - IR_s)}{kT} \right] - 1 \right\} - I_L \quad , \tag{1.6}$$

where R_s is the contact resistance. Although the open circuit voltage stays the same with certain contact resistance, the short circuit current can decrease a lot for large contact resistance. The conversion efficiency may be further reduced due to the reduction of fill factor since contact resistance takes away a decent amount of voltage from the load at a large working current such as I_m. Figure 1.10

clearly shows the effect of contact resistance according to Eq. 1.6. The situation is even worse in concentrated photovoltaics (CPV), where sun light is concentrated by 500-1000 times. The degradation of fill factor with increasing solar concentration is shown in Fig. 1.11. Therefore, a contact design may work well for a non-concentrated solar cell but it may fail due to largely reduced fill factor when the solar cell is illuminated by concentrated sun light. Specific contact resistance can be decreased by using expensive metals but the cost can be increased substantially. Increasing the front contact area is another effective way to decrease the contact resistance but more sun light is blocked. Therefore, a lot of front contact grid designs are developed to more efficiently collect the carriers and reduce the contact resistance while keeping the light blocking and cost to a minimum [35, 36].

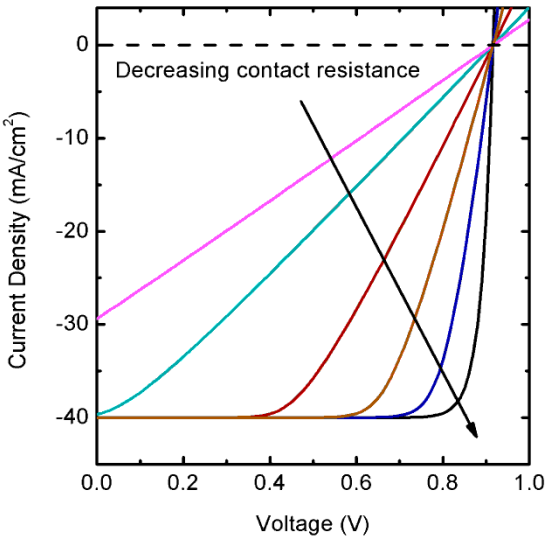

Fig. 1.10. I-V characteristic of a solar cell with a contact resistance under illumination.

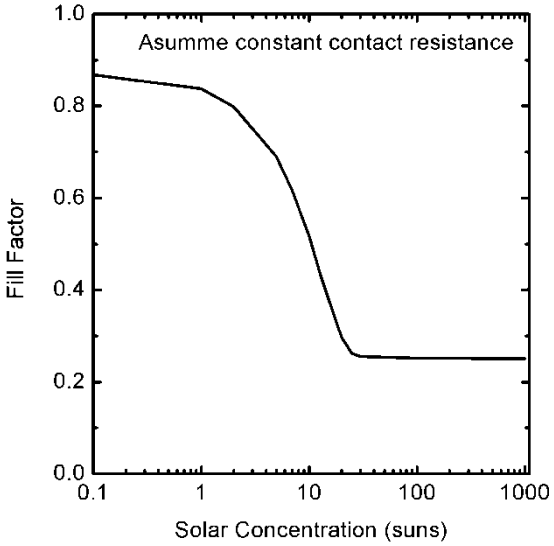

Fig. 1.11. The dependence of solar cell fill factor on solar concentration at constant contact series resistance.

1.6.3 Techniques to Reduce Shunt Resistance

Shunt resistance reduces the solar cell conversion efficiency in a different way compared contact resistance. It is a current bypass around the solar cell that is mostly created by cell processing steps or due to bad material. Due to the nature of shunt resistance, carefully designed processing recipes are needed. The shunt resistance can be represented by a resistor parallel with the cell and the I-V relation is modified as,

$$I = I_s\left[\exp\left(\frac{qV}{kT}\right)-1\right]-I_L+\frac{V}{R_{sh}} \quad , \qquad (1.7)$$

where R_{sh} is the shunt resistance. As can be seen, the shunt resistance reduces the solar cell working current but the short circuit current still remains the same. The open circuit voltage is also reduced due to this extra current path. Moreover, the fill factor is reduced due to the above two reasons. It is known that the solar cell working voltage only changes a little under different solar concentrations but the current changes linearly, which means that the shunt resistance has a greater impact to the cell performance under low concentration since the current diverged by the shunt resistance is almost a constant. Figure 1.12 shows the I-V relation of the solar cell with different shunt resistance. And Fig. 1.13 shows the change of fill factor with various concentrations.

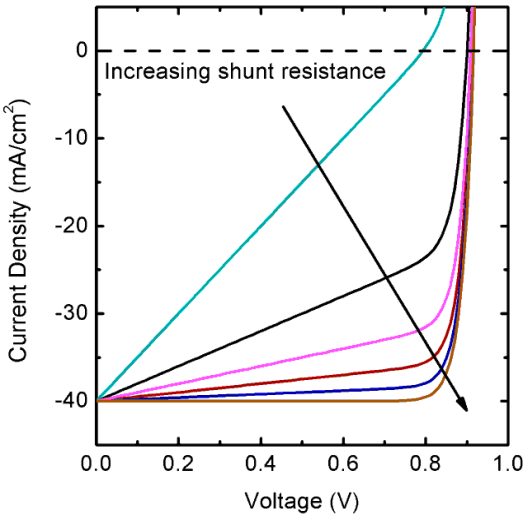

Fig. 1.12. I-V relation of the solar cell with different shunt resistance.

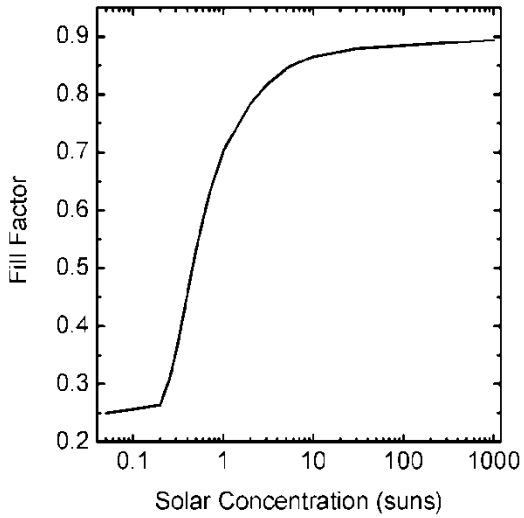

Fig. 1.13. Fill factor dependence on various concentrations for the same shunt resistance.

1.6.4 Techniques to Reduce Contact Shadowing

Front contact can block sun light from entering the cell and the total area should be minimized for high conversion efficiency. And there is a trade-off between contact shadowing and contact resistance. For a typical solar cell, the front contact area is about 5-10% of the total surface area [36]. As discussed previously, advanced front contact grid designs are developed to reduce the solar cell contact resistance while using the minimum total contact area. Moreover, three ways are typically adopted to achieve reduced contact shadowing.

The first one is to use transparent contacts instead of conventional metal

contacts. Transparent conducting oxide and carbon nanotubes have drawn quite some interest. Among these materials, Indium-Tin-Oxide (ITO) is the most successful and features high electric conductivity. The drawback is the absorption in the infrared region due to free carrier absorption and potentially high cost due to the limited Indium supply [37]. For this reason, Aluminum doped Zinc-Oxide and Indium doped Cadmium-Oxide have been proposed as alternatives [37, 38]. Recently, the research on carbon nanotubes shines light on future transparent contacts due to their potential of high conductivity and high transmittance in the infrared region [39, 40].

The second one is a technique called buried-contact developed for Si solar cells which can effectively increase the contact area in the vertical direction while maintaining small surface area in the horizontal direction [41, 42]. In this structure, a deep groove is firstly formed by laser scribing on the top surface, and then a highly doped p region is formed around the groove by phosphorus diffusion. After that, the groove is filled with metal by electro-plating. The drawback is that damage, including microcrystalline regions and dislocations, may be formed during the laser scribing and oxidation processes.

The third one is to put both n and p contacts on the backside, thus leaving no front contact shadowing at all [43]. This structure not only eliminates the

shadowing but also reduces the series resistance when connecting cells together to form a module. Current Si unit cells are becoming larger and larger which results in increasing current. This requires thicker contact tabs to be soldered to the front and back of the solar cell contacts to keep the resistance low. But due to the strain created by solar heating the tabs are currently almost at their maximum thickness [44]. If both contacts are at the back, thinner and wider tabs could be used to reduce the resistance.

1.6.5 Techniques to Reduce Front Surface Reflection

A decent amount of light can be reflected by the front surface of a semiconductor solar cell due to the large refractive index. Therefore, anti-reflection (AR) coating and surface light trapping structures are often used to reduce light reflection. Unlike the AR coating for camera lens which requires low reflection only in the visible spectrum, the coating for solar cell has to work for a much broader spectrum from infrared to ultraviolet. This adds great difficulty to the coating design and usually multi-layer coating is required for optimum performance. To date, various coating materials have been tried, such as SiO, SiO_2, Si_3N_4, TiO_2, Al_2O_3, Ta_2O_5, SiO_2- TiO_2, ZnS, MgF_2 [45-50]. These materials are usually deposited by PECVD, which results in broad spectrum reflectance below 10% [51-53]. Recently, a triple-layer SiO_2/SiO_2- TiO_2/ TiO_2

coating with average reflectance of 3.2% (400-1000 nm) was developed using spin-coating technique, which could offer the potential of low-cost solar cell fabrication [54]. Surface light trapping is usually achieved by texturing the front surface by anisotropic etching [34, 41]. When light is incident on the front surface, it can bounce between the small pyramids many times and eventually be absorbed. The typical structures can be found in Ref. 34 and 41.

II. PRESENT TRIPLE-JUNCTION SOLAR CELLS AND BEYOND

Currently, triple-junction solar cells hold the record of energy conversion efficiency for both space and terrestrial applications. This chapter discusses the various approaches for triple-junction solar cells and their limitations. Then a material platform based on monolithically integrated II-VI and III-V material systems is proposed for multi-junction (MJ) solar cell applications. And new design principles are discussed for this material platform. The advantages and potential problems of this material platform are also briefly discussed.

2.1 Advantage of Multi-Junction Solar Cells

As discussed previously, the best single junction solar cells can only give efficiencies about 26% [14], where the transmission loss and thermal relaxation loss accounts for 34% and 20% efficiency loss, respectively. In general, these two losses are difficult to reduce in single junction solar cells. However, MJ solar cells can effectively address both losses by vertically stacking several single junction solar cells with decreasing bandgaps from the top. In a MJ cell, the transmission loss is reduced by using subcells with smaller bandgaps. And the thermal relaxation loss is reduced since the subcells divides the solar spectrum into several sections and the average photon energy is closer to the corresponding subcell bandgap. A typical triple-junction solar cell structure design is shown in Fig. 2.1 [55]. A tunnel junction is usually used to connect the adjacent subcells.

The whole structure is usually grown by various epitaxial techniques, such as molecular beam epitaxy (MBE) and metal organic chemical vapor deposition (MOCVD). Figure 2.2 shows the corresponding energy bandgaps of the subcell materials along with the solar spectrum [32].

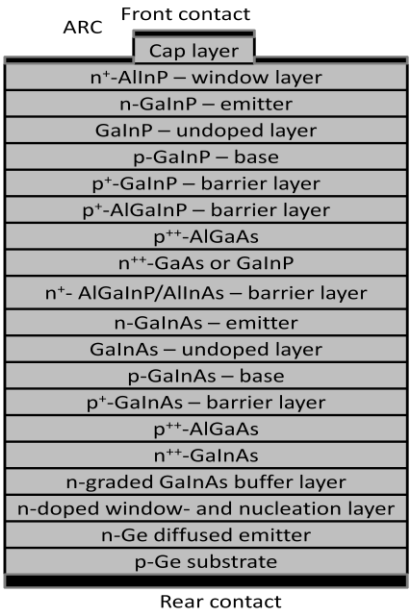

Fig. 2.1. A typical InGaP/InGaAs/Ge triple-junction solar cell structure [55].

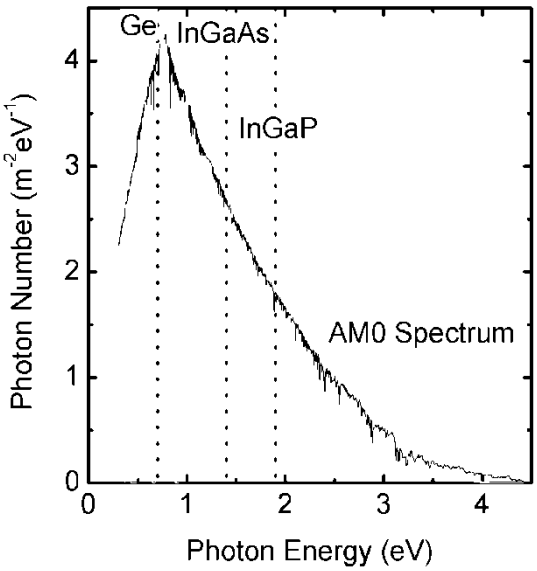

Fig. 2.2. The corresponding energy bandgaps of the subcell materials along with the solar spectrum [32].

2.2 Keys to High Efficiency Multi-Junction Solar Cells

The most important keys to highly efficient MJ solar cells are the abilities

to i) match the current of all junctions at the optimal working condition, and ii) match the lattice constant of all epitaxial layers to the substrate to achieve high crystalline quality. These two requirements place strict limits on the possible choice of epitaxial materials and substrates used for the devices.

The current matching condition puts a constraint to the choice of the subcell bandgaps. From Fig. 2.2, it can be seen that each of the three subcells can produce a certain current that is directly related to the number of photons absorbed. These subcells have to work under the same current, since they are connected in series. This current usually limited by the lowest current produced by the subcells if they were to work independently. In order to achieve the highest possible energy conversion efficiency, all the subcells have to produce the same current at their optimum working conditions. Therefore, the current matched bandgaps have to partition the solar spectrum into almost equal parts in terms of photon numbers. And the current matched bandgaps change as the solar spectrum (air mass condition) varies. It should be noted that the current matched bandgaps also change with solar concentration. This is because the optimum working current for each subcell does not increase exactly linearly with solar concentration due to various competing recombination mechanisms. Moreover, slight change in recombination loss also results in a big change in

spatial relaxation loss according to the discussion in the previous chapter. Usually, many different sets of current matched bandgaps exist and a set of optimum bandgaps can be found to give the highest conversion efficiency.

After the optimum bandgaps of an N-junction solar cell are determined, the desirable materials with the right bandgap need to be identified. These materials are usually grown on single crystal substrates by various epitaxial techniques. In order to get high quality epitaxial materials, the material lattice constant should be the same or close to the substrate lattice constant, which is therefore called the "lattice-matching condition". This condition puts a very strict restriction on the possible materials that can be used for MJ solar cells monolithically grown for a particular substrate. There are several common semiconductor substrates such as Si, Ge, GaAs, InP, InAs and GaSb, each with a different lattice constant. Figure 2.3 shows the energy bandgaps of various alloys as a function of lattice constant [56]. As can be seen, for each of the substrates, there exists a few binary or ternary materials with the same lattice constant. This means if a substrate is chosen, only a few different materials with certain bandgaps can be found to be lattice-matched to the substrate. But usually these bandgaps can hardly meet the current matching condition described previously. And it will be even more difficult to reach the optimum bandgaps

selected from all the possible current matched designs. Therefore, it is usually very challenging to meet both the current matching and lattice matching conditions simultaneously in a real MJ solar cell design. And a practical design is usually a compromise between these two conditions.

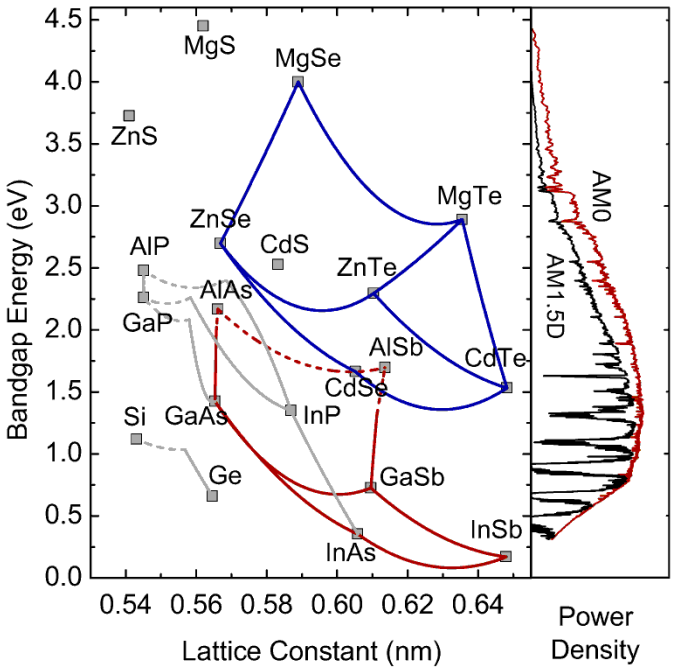

Fig. 2.3. Bandgap energy versus lattice constant for various alloys [56]. The power density of the AM0 and AM1.5D solar spectra are shown on the right.

Moreover, tunnel junctions are necessary to connect adjacent subcells. The key to make a good tunnel junction is the high doping of both n- and p-type regions, which is not trivial at times [57-61]. For example, ZnSe and ZnTe are

easily doped n- and p-type, respectively [58, 59]. But p-type CdSe, ZnSe and n-type ZnTe are difficult to achieve [60, 61]. Furthermore, good window layer not only has to meet lattice matching condition but also requires large bandgap. And good anti-reflection coating is also important, which has to work for a much broader spectrum range than the coating for single junction solar cells.

2.3 Limitations of State-of-the-Art Triple-Junction Solar Cells

The state-of-the-art triple junction solar cells hold the current energy conversion efficiency record. In order to further increase the efficiency, one has to carefully analyze the present cell designs according to current and lattice matching conditions discussed previously.

In a typical triple-junction solar cell structure as shown in Fig. 2.1, the top and middle cell materials are $In_{0.50}Ga_{0.50}P$ and $In_{0.01}Ga_{0.99}As$ with energy bandgaps 1.9 eV and 1.4 eV, respectively [55, 62]. And these two materials are lattice matched to the Ge substrate. Therefore, the misfit dislocations are greatly limited and the material quality can be very high in this design. The energy conversion efficiency has reached 32.0% and 40.1% under 1 sun AM1.5G and 135 suns AM1.5D conditions, respectively [62].

The drawback of this lattice matched design is that current matching condition is not achieved. The Ge bottom cell can produce almost twice of the

current produced by the top two cells. In order to better match the current, the bandgaps of the top two cells need to be lowered to produce more current. It should be noted that moving up the bottom cell bandgap to match the current is not a good option, since there are enough photons for adding one more subcell between $In_{0.01}Ga_{0.99}As$ and Ge cells and results in a four-junction design. Therefore, another combination of the top two cells $In_{0.56}Ga_{0.44}P$ and $In_{0.08}Ga_{0.92}As$ has been tried with energy bandgaps of 1.8 eV and 1.3 eV, respectively [62]. These two materials have lower bandgap energies and can better match the current. However, due to the lattice mismatch, the misfit dislocations are greatly increased resulting in poorer material quality. As a result, the energy conversion efficiency reached 31.3% and 40.7% under 1 sun AM1.5G and 240 suns AM1.5D conditions, respectively [62]. This means the advantage of better current matching is greatly negated by the poor material quality.

To even better match the current, the combination of $In_{0.65}Ga_{0.35}P$ and $In_{0.17}Ga_{0.83}As$ is used [63]. This approach has been investigated by the Fraunhofer ISE and a conversion efficiency of 41.1% under 454 suns AM1.5D condition has been demonstrated [63]. Due to the large lattice mismatch of about 1.1%, a carefully designed InGaAs buffer layer is used to minimize the defects in the top two cells. Since the current is almost perfectly matched in the

design, to further increase the efficiency requires further improvement of the material quality and systematic change of all three subcell bandgaps for an optimum current matched design.

Besides this Ge substrate, GaAs substrates are also used for triple junction solar cells. A typical device structure is shown in Fig. 4.4 [64]. In this design, the top cell $In_{0.50}Ga_{0.50}P$ is grown first on the GaAs substrate then the middle cell GaAs is grown and finally the bottom cell $In_{0.3}Ga_{0.7}As$. This growth sequence is reversed compared with the Ge based triple junction solar cells, where the bottom cell is grown first. Therefore, this type of structure is called inverted metamorphic (IMM) and the Ge based cell (with at least one lattice mismatched cell) is called metamorphic (MM) cell. The top two cells are lattice matched to the GaAs substrate and therefore have low misfit dislocation densities and high material quality. The bottom cell is made of $In_{0.3}Ga_{0.7}As$ with a bandgap of 1.0 eV, which matches the current better than Ge. But the lattice mismatch between $In_{0.3}Ga_{0.7}As$ and the GaAs substrate is about 2%, which results in high density of misfit dislocations even with carefully designed buffer layer. Although this IMM structure contains lattice mismatched subcell just like the Ge based MM designs, the energy conversion efficiency could potentially be higher since the most important top two cells are lattice matched to the substrate and have the

highest material quality. This structure has reached energy conversion efficiency of 33.8%, 30.6% and 38.9 under 1 sun AM1.5G, 1 sun AM0 and 81 suns AM1.5D conditions, respectively [64].

The IMM designs discussed above still have room for further improvement as the current is still not perfectly matched. In order to further increase the conversion efficiency, the middle and bottom cell bandgaps need to be lowered. Therefore the material combination of 1.83 eV $In_{0.49}Ga_{0.51}P$, 1.34 eV $In_{0.04}Ga_{0.96}As$ and 0.89 eV $In_{0.37}Ga_{0.63}As$ is investigated by NREL [65]. Even with two metamorphic subcells, this design still reaches 40.8% efficiency under 326 suns AM1.5D condition due to the better current matching.

To summarize the above discussions, various triple junction solar cell designs are listed in Table 2.1. Although these efficiencies are impressive, they can still be further improved by developing materials that are lattice-matched and cover a broad range of bandgap energies. And at present, it seems difficult to further improve the efficiencies for the triple-junction solar cells considering the less than 1% efficiency increase in recent years. The next big boost in conversion efficiency may come from adding one more junction. In order to do that, a high quality lattice-matched material with about 1.0 eV bandgap is needed. The 1.0 eV lattice matched quaternary alloy InGaNAs has been investigated, but

no improvement in conversion efficiency has been observed due to its short minority-carrier lifetime, or diffusion length [66-68]. It is therefore necessary to explore new approaches with the potential to reach even higher efficiencies using lattice-matched materials with a wide range of optimal bandgap energies for the best possible performance.

Table 2.1. State-of-the-art triple-junction solar cell designs (I-V).

Design I. LM			
	Material	E_g (eV)	Lattice matched (Y / N)
Top cell	$In_{0.50}Ga_{0.50}P$	1.86	Y
Middle cell	$In_{0.01}Ga_{0.99}As$	1.39	Y
Bottom cell	Ge	0.66	Y

Design II. MM			
	Material	E_g (eV)	Lattice matched (Y / N)
Top cell	$In_{0.56}Ga_{0.44}P$	1.80	N
Middle cell	$In_{0.08}Ga_{0.92}As$	1.29	N
Bottom cell	Ge	0.66	Y

Design III. MM			
	Material	E_g (Ev)	Lattice matched (Y / N)
Top cell	$In_{0.65}Ga_{0.35}P$	1.67	N
Middle cell	$In_{0.17}Ga_{0.83}As$	1.18	N
Bottom cell	Ge	0.66	Y

Design IV. IMM			
	Material	E_g (Ev)	Lattice matched (Y / N)
Top cell	$In_{0.50}Ga_{0.50}P$	1.82	Y
Middle cell	GaAs	1.39	Y
Bottom cell	$In_{0.3}Ga_{0.7}As$	1.02	N

Design V. IMM			
	Material	E_g (Ev)	Lattice matched (Y / N)
Top cell	$In_{0.49}Ga_{0.51}P$	1.83	Y
Middle cell	$In_{0.04}Ga_{0.96}As$	1.34	N
Bottom cell	$In_{0.37}Ga_{0.63}As$	0.89	N

2.4 A New Material Platform for Multi-Junction Solar Cells and Design Principles

The integration of lattice-matched II-VI (ZnCdMg)(SeTe) and III-V (InGaAl)(AsSb) compound semiconductor material systems offers great advantage for MJ solar cell applications over the conventional GaAs and Ge based materials. As can be seen from Fig. 2.3, if quaternary materials are used, this material integration can provide bandgap coverage for almost the entire solar spectrum from 3.0 eV down to 0.4 eV with any given lattice constant roughly between 5.9 and 6.1 Å. And in this study, solar cell designs based on these materials grown on GaSb substrate with 6.1 Å lattice constant are investigated. Furthermore, this material system can also be grown on InAs and InP substrates. Moreover, most of these alloys have direct bandgaps and can be grown with zinc blende crystal structure.

The use of these semiconductors for solar cells has two important advantages: i) lattice-matched materials result in fewer misfit dislocations than metamorphic materials and ii) direct bandgaps result in much thinner junctions than indirect bandgap materials; both of which substantially improve device performance by reducing parasitic recombination losses within each junction. This material system also enables the construction of solar cell structures with

even more junctions, such as 4, 5 or 6 using lattice matched alloys. Furthermore, it should be noted that the binary material ZnTe has a lattice constant very close to 6.1 Å, which is also the lattice constant of GaSb. Thus, if GaSb is selected as the MJ solar cell substrate, ZnTe could be a very good candidate for a subcell material due to its ease to grow. These highly desirable features are not available with any other known material systems that can be grown on any known substrates including GaAs and Ge.

Besides lattice matching and direct bandgap, the GaSb based II-VI and III-V material system has several other advantages from the material growth point of view. First, the alloys can potentially be doped both n- and p-type quite heavily, enabling the formation of tunnel diodes connecting adjacent subcells in the MJ cell design. Table 2.2 lists the most commonly used dopants and their maximum doping concentrations in the binaries. It has been demonstrated that the properties of alloys consisting of these binaries will have mixed properties for n- and p-type doping [69, 70]. And both n and p-type doping for antimonides is straightforward. Second, this material system permits the formation of tunnel junctions using type-II hetero-junctions that require significantly lower doping levels compared to conventional tunnel junctions that must be very heavily doped. Third, this material system offers unparalleled selection of wide bandgap

materials for surface, interface passivation and window, back surface field (BSF) layer. Forth, low resistance contacts have been demonstrated for most of the binary materials as listed in Table 2.3. Lastly, the formation of misfit dislocations caused by thermal mismatch is quite limited in this material system. It is well known that misfit dislocations can form during the post growth cool-down process when the constituent materials have mismatched thermal expansion coefficients. The reported thermal expansion coefficients for the proposed materials range from 4 to 8×10^{-6} K^{-1}; this range is narrow enough so that the formation of structural defects due to thermal mismatch is minimal [71].

Table 2.2. List of dopants and their maximum doping concentrations in the binaries of interest.

Materials	Dopants	n (cm^{-3})	Materials	Dopants	p (cm^{-3})
n-ZnSe	I	$>10^{18}$ [72,73]	p-ZnSe	N	4×10^{17} [61, 74]
n-CdSe	Cl	$>10^{19}$ [75]	--		
n-ZnTe	Al, Cl	$<4\times10^{18}$ [60, 76]	p-ZnTe	P, N	3×10^{19} [59, 61, 74, 77-79]
n-GaSb	Te	4×10^{18} [80]	p-GaSb	C, Ge, Sn	10^{19} [81, 82]

Table 2.3. List of ohmic contacts for the binaries of interest.

Semiconductor	n-contact material	p-contact material
ZnTe	W, In, In/Hg [60, 83]	Au, Pt, Au/Pt/Pd, Au/Pt/Ti/Ni [59, 61, 77-79, 84-86]
ZnSe	Al [71]	--
CdTe	--	HgTe [87]
GaSb	Au/Sn/Au [88, 89]	Ti/Au [88]

Preliminary experimental work on the growth of II-VI materials on GaSb and InAs substrates shows very encouraging results [57]. High-resolution x-ray diffraction measurements and transmission electron microscopy micrographs show very uniform alloy compositions, layer thicknesses and excellent, abrupt, smooth semiconductor interfaces [90]. Although the initial growth turned out to be quite successful, much more work are still needed, such as defect reduction in various ternary, quaternary materials, and optimal doping in II-VI semiconductors.

III. NUMERICAL SIMULATION OF SOLAR CELLS

With the technology development during the past years, solar cells with higher performance are more and more desirable. Theoretical simulations of cell devices can not only help to optimize the device performance but also save R&D time and cost. In the early years of solar cell research, people already developed various theoretical models, such as the detailed balance models developed by Shockley and Queisser [31] and Henry [91], to predict solar cell efficiency limits. While these detailed balance models are helpful to roughly predict solar cell efficiency limits, solar concentration effect, and optimal material bandgaps, they fail to provide a detailed device structure design with quantitative performance prediction.

In this chapter, the commercial software package Silvaco is used to design and optimize the various solar cell structures. Silvaco is one of the TCAD (technology computer-aided design) tools, which use 2D/3D finite element analysis to model various semiconductor devices [92, 93]. Other popular software packages include Synopsys, Crosslight, GSS, Archimede, Aeneas, etc. These TCAD tools can usually model both semiconductor device fabrication and device operation by using various physical models. Table 3.1 lists the capabilities of the detailed balance model and Silvaco. Although simulations using Silvaco usually takes longer to complete, these simulations use real material

parameters and considers both radiative and non-radiative recombination. Therefore, the efficiency predictions from Silvaco are closer to experimental ones compared with detailed balance model. Moreover, solar cell structure designs, including layer thickness and doping, can be optimized by using Silvaco simulations. The knowledge learned from this optimization process is important to the understanding of limiting factors of the solar cell performance, such as carrier mobility, photon absorption coefficients, and recombination coefficients. The basic models and numerical implementations for solar cell simulations can be found in Appendix I. Furthermore, the modeling accuracy often depends on the choice of physical models and associated material parameters. The material parameters used in the simulations are listed in Appendix II.

Table 3.1. Comparison of capabilities of detailed balance model and Silvaco.

	Detailed balance model	Silvaco
Radiative Recombination	Y	Y
SRH & Auger Recombination	N	Y
Guide for detailed cell structure design	N	Y
Calculation time	Minutes	Hours

3.1 GaAs Single Junction Solar Cell Simulation

In this section, a GaAs single junction solar cell is defined and simulated using Silvaco. The various approximations are discussed and followed by the discussion of different effects including carrier concentration dependent mobility, bandgap narrowing, contact shadowing, contact resistance, surface recombination and thick substrate. It also tries to demonstrate the various physical quantities that could be extracted from the simulation.

In the work, a 150 μm wide and 3 μm thick GaAs solar cell is defined and shown in Fig. 3.1 (a). In this 2-Dimensional simulation, the calculation is only done on the $150 \times 3\ \mu m^2$ mesh shown in Fig. 3.1 (b). Physical quantities along the third dimension (depth of the solar cell) are assumed the same with those on the 2D mesh. The top contact locates at the center with a width of 7.5 μm corresponding to 5% area coverage. The top contact is set to be opaque to simulate the contact shadowing effect. The bottom contact spreads across the whole area which is common for solar cells. And both contacts are assumed ohmic. The solar spectrum used in the simulation is AM1.5G corresponding to the un-concentrated terrestrial applications. The current efficiency record for GaAs single junction solar cell is 26.1% under AM1.5G condition [14].

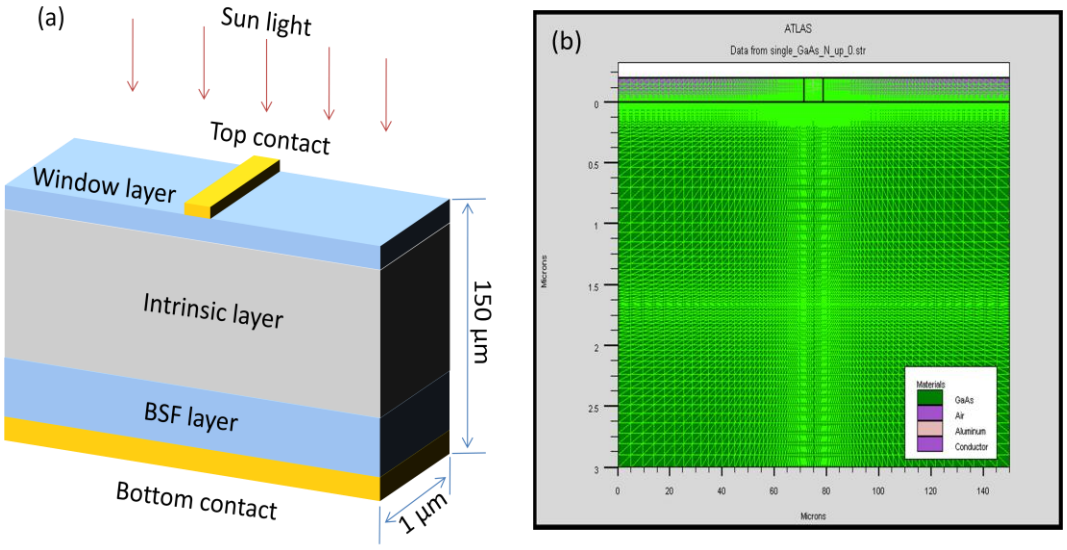

Fig. 3.1. GaAs single junction solar cell structure. (b) 2D meshing of the simulated solar cell.

In this solar cell structure, the window and back surface field (BSF) layers are made from highly doped GaAs. Therefore, only homo-junction is involved in the simulation, which simplifies the calculation by avoiding the simulation of hetero-interfaces. Moreover, perfect front surface anti-reflection (AR) coating is assumed, which means all the sun light can get into the solar cell without reflection. Although AR coating can never be perfect in a real solar cell, it can always be improved. Therefore, it is reasonable to assume perfect AR coating when calculating the solar cell efficiency limit. Below bandgap absorption is another factor that is not included in the calculation. The reason is that the width

of Urbach tail is material dependent and is just on the order of kT for direct bandgap materials [94]. This only results in tiny changes in the energy conversion efficiency. However, generation from below bandgap absorption may help to improve the short circuit current and therefore may further improve the conversion efficiency. Free carrier absorption is not considered due to the reason that the absorption is mainly for low energy photons.

In general, carrier mobility changes with carrier concentration due to scattering. And carrier concentration dependent mobility model provided by Silvaco can take care of this effect. Unfortunately, this model is only available for Si and GaAs, for which a lookup table for mobility and the corresponding carrier concentration is provided. For other materials, this information is hard to find due to the lack in material research especially for many ternary and quaternary materials. Therefore, it is desirable to know the impact this model. Figure 3.2 shows the conversion efficiency calculated using concentration dependent mobility model and constant mobility model. From the results it can be seen that the difference by using these two models is usually less than 0.5% and this difference only exceeds 1% when the concentration is over 1000 due to the higher carrier concentration. However, the cell structure design can be modified to take the reduced diffusion length into account. Therefore, the

conversion efficiency can be further reduced. Moreover, this means that solar cell structures should be optimized at specific solar concentrations and a universally optimized design is generally difficult to achieve. Furthermore, there is not enough experimental data on the material parameters especially for ternary and quaternary materials at present. Therefore, most of the material parameters have to be interpolated from binary material parameters and their accuracy is not very high. Thus, the constant mobility model rather than the concentration dependent mobility model is used in the later calculations to give the efficiency limits.

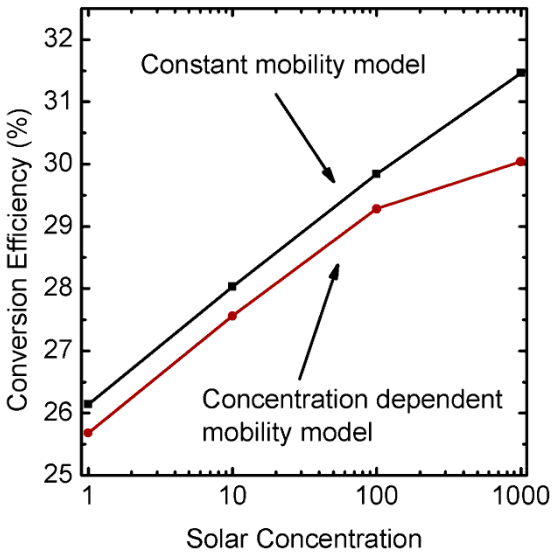

Fig. 3.2. Conversion efficiency calculated using concentration dependent mobility model and constant mobility model under various solar concentrations.

Bandgap narrowing is a phenomenon caused by many-body interactions in the highly doped semiconductor regions [95] and therefore mainly occurs in window and BSF layers. In Silvaco, this can be taken care of by the Slotboom, Klaassen and the universal bandgap narrowing models. And the Slotboom model gives the biggest bandgap shrinkage of about 80 meV at 10^{19} cm^{-3} doping level [92]. Figure 3.3 shows the calculation results with and without this bandgap narrowing model. It can be seen that the efficiency is lowered by about 1% under the Slotboom model at various solar concentrations. This efficiency drop is mainly due to the reduced working voltage caused by the reduction of effective bandgap of the window and BSF layers. However, in a practical solar cell design, the window and BSF layers are usually made of hetero-structures with moderate doping levels. Therefore, the required potential barrier is mainly formed by the band offset rather than doping. And the quasi-Fermi levels are not limited by the band edges in the window and BSF layers. Thus, the efficiency drop due to bandgap narrowing is hardly seen in a well designed practical cell. For this reason, the bandgap narrowing effect is not taken into account in later calculations.

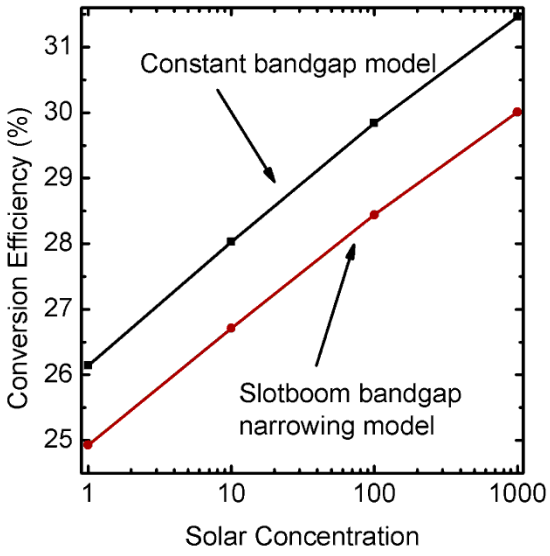

Fig. 3.3. Conversion efficiency calculated with and without this bandgap narrowing model under various solar concentrations.

Front metal contact grid can block some of the sun light and therefore reduce the conversion efficiency. When calculating the efficiency limit, it is useful to take this effect out because different cell designs have different contact area coverage. And when it is necessary to compare efficiencies with different contact area coverage, the effective efficiency η with contact shadowing can be calculated as

$$\eta = \eta_0 /(1+C) \quad , \tag{3.1}$$

where C is the front contact area coverage, η_0 is the efficiency assuming transparent contact. Table 3.2 shows the calculation results from Eq. 3.1

assuming 5% opaque contact area coverage. From Table 3.2, it can be seen that although the carrier distribution is slightly different between using transparent and opaque contact, the results are quite similar. Therefore, in later calculations transparent contact is assumed and η_0 is given as the efficiency limit.

Table 3.2. Calculation results from Eq. 3.1 assuming 5% opaque contact area coverage.

Solar concentration	η_0 (%)	η (%)	Opaque contact efficiency (%)
1	26.1	24.9	25.1
10	28.0	26.7	26.9
100	29.8	28.4	28.7
1000	31.5	30.0	30.2

Finite contact resistance is another factor that can lower the working voltage of real solar cells. Typically, 10^{-6} $\Omega \cdot cm^2$ contact specific resistance can be achieved for both n and p-type GaAs contacts, respectively [96, 97]. Table 3.3 shows the effect of contact resistance on conversion efficiency. It can be seen that for low contact resistance, the efficiency drops less than 0.1% even at 1000 suns concentration. And a noticeable efficiency drop only occurs when the

specific contact resistance is over 10^{-5} $\Omega \cdot cm^2$ and solar concentration is over 1000. Therefore, in later calculations, contact resistance is assumed zero to give the efficiency limit.

Table 3.3. Conversion efficiencies with and without specific contact resistance at various solar concentrations.

Solar concentration	Efficiency without specific contact resistance (%)	Efficiency with 10^{-6} $\Omega \cdot cm^2$ specific contact resistance (%)
1	26.14	26.14
10	28.03	28.03
100	29.84	29.84
1000	31.46	31.44

Surface recombination reduces the quantum efficiency and therefore reduces the solar cell working current. Passivation layers can reduce the surface recombination and so do the window and BSF layer. It should be noted that although the surface recombination velocity is about 10^6 - 10^7 cm/s for unpassivated GaAs-air surface, 10^3 cm/s recombination velocity could be achieved for well passivated surface [98]. In solar cell simulations, only the

surface recombination at the top surface is important because the carrier generation rate is the highest. Assuming 10^3 cm/s recombination velocity, the efficiency drop is unnoticeable even at 1000 suns concentration. Moreover, the conversion efficiency only drops 0.5% when the surface recombination velocity reaches 10^5 cm/s at 1000 suns concentration. Therefore, in later calculations the surface recombination is assumed zero to give the efficiency limit.

Most solar cell devices often carry a thick substrate rather than just the epitaxial layer. For GaAs based solar cells, the typical substrate thickness is about 350 μm. Therefore, a simulation is done to test the importance of including the substrate in the calculation and results are shown in Fig. 3.4. It can be seen that the conversion efficiency is increased by less than 0.2% if the substrate is included and concentration is not high. Although 99% of the photons can be absorbed by 3 μm think GaAs, close to 100% of the photons could be absorbed with the help of the substrate. Therefore, more current is produced when the substrate is included in the calculation. However, the efficiency is lowered by about 0.2% including the substrate when the concentration is above 1000. This is because the increased carrier concentration can cause more SRH and radiative recombinations in the substrate, which completely negate the advantage of more complete photon absorption. In general, the difference in

efficiency with or without the substrate is always within 0.2% at concentrations below 1000. Therefore, in the later calculations, the substrate is not included to reduce the calculation load.

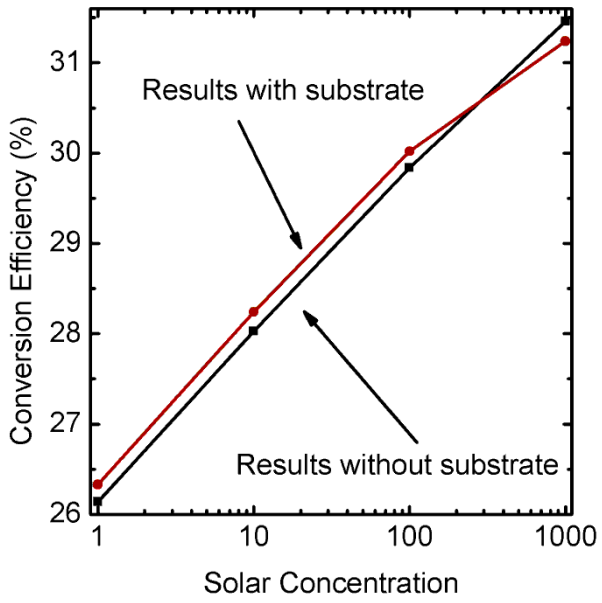

Fig. 3.4. Conversion efficiency calculated with and without substrate under various solar concentrations.

From the above discussion, it can be concluded that although many approximations are made, the calculated efficiency limits are still close to the ones achievable by practical cells. Moreover, the simple models used in the calculations require less material parameters than the advanced models and are quite desirable at early stage of research. And the calculation load is also greatly

reduced without losing much accuracy. Furthermore, this numerical simulation can not only give detailed device designs but also provide many physical quantities and some of them are hard to probe from experiments. These physical quantities include current-voltage (I-V) characteristic, band diagram, position dependent recombination rate, electric field, carrier density, quasi-Fermi levels, current density, generation rate profile, spectral response, etc. These physical quantities can be used to understand the device limits and help to further optimize the device performance. As an example, some of the physical quantities are extracted and shown in Fig. 3.5.

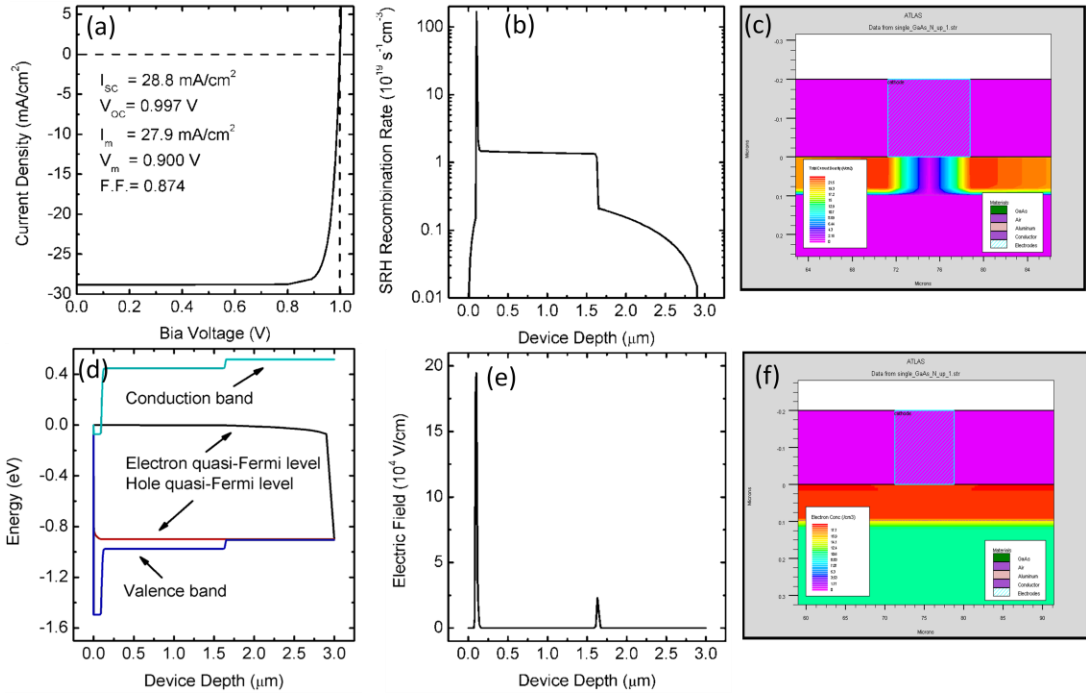

Fig. 3.5. Various physical quantities extracted from the numerical simulation. (a) I-V relation, (b) SRH recombination rate, (c) current density profile near cathode, (d) band diagram, (e) electric versus device depth, (f) electron density near cathode.

3.2 Simulation Sensitivity on Input Parameters

In the numerical simulation of solar cells, various material parameters are needed for accurate results. The ternary and quaternary material parameters used in the simulations, such as Shockley-Read-Hall (SRH) recombination lifetimes, radiative recombination coefficients, carrier mobilities, effective masses, and absorption coefficients are obtained from linearly interpolated

published values [71, 99, 100]. Since many of the published material parameters are scattered, a sensitivity analysis of the impact of the parameter values on the device performance is carried out using GaAs single junction solar cell.

As expected, the most critical recombination loss mechanism is SRH, which is characterized by the electron and hole nonradiative lifetimes. Figure 3.6 shows conversion efficiency dependence on carrier lifetimes. In the simulations, 5 ns and 10 ns is used for electron and hole lifetimes, respectively. These are published values which are typical for molecular beam epitaxial (MBE) grown material with the doping levels used in the device. The efficiency is only improved by 0.9% when the electron lifetime is increased to 1 μs, which represents very high quality epitaxial material. While the overall efficiency decreases by 0.8% when the electron lifetime is reduced to 1 ns, which represents lower quality epitaxial material with a large number of defects. The sensitivity to variations in the hole lifetime is similar. The efficiency is improved by 0.7% when the hole lifetime is increased to 1 μs, and decreased by 1.8% when the hole lifetime is reduced to 1 ns. It can be seen that the conversion efficiency various 1.7% and 2.5% when the electron and hole lifetime changes three orders of magnitude, respectively. And for reasonable quality lattice-matched epitaxial materials, the carrier lifetime is usually longer than 1 ns due to the low density of

material defects. However, for metamorphic material where the presence of high-density misfit dislocations can reduce the electron and hole lifetime to less than 1 ns, the impact of the carrier lifetime becomes an important factor to performance and reduces the overall efficiency significantly.

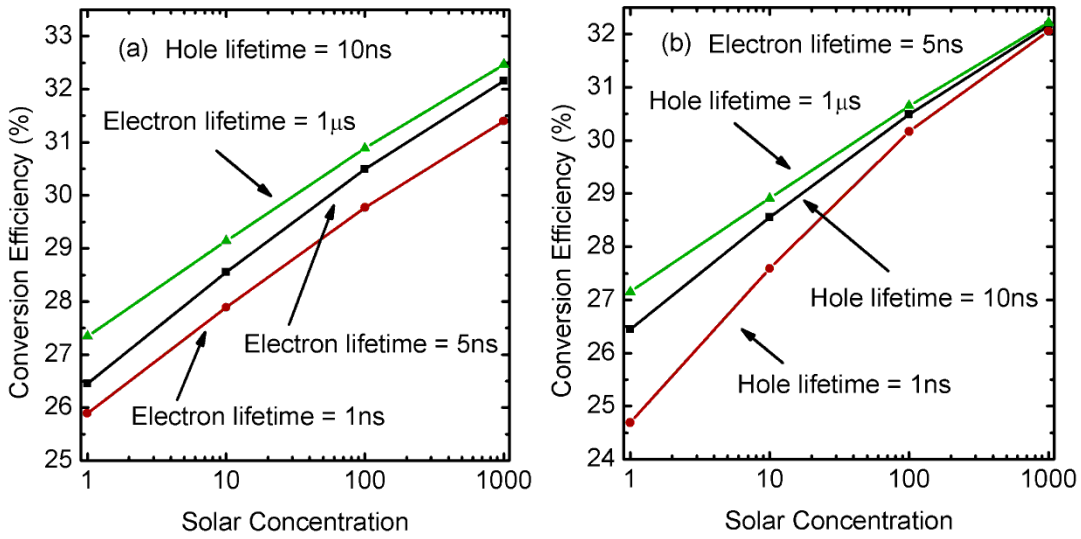

Fig. 3.6. Conversion efficiency with different carrier lifetimes and solar concentrations: (a) hole lifetime is kept at 10 ns; (b) electron lifetime is kept at 5 ns.

Moreover, the efficiency difference by using different lifetimes becomes smaller as the solar concentration increases as shown in Fig. 3.6. This is because the efficiency increase by using high solar concentration mainly comes from the

improvement of working voltage or quasi-Fermi level separation. The current is increased roughly proportional to the concentration and does not contribute to the efficiency increase. At high solar concentration, the shorter carrier lifetime only results in a tiny reduction of the total current and the current still roughly increases linearly with concentration. Therefore, the working voltage does not change much for different carrier lifetimes. Thus, the change in carrier lifetime becomes less important. And this effect can also be used for the study of carrier lifetime related solar cell issues. Particularly, the effect of short carrier lifetime can be removed by using high solar concentration. Moreover, it should be noted that the lifetime value used in the calculation is from published experimental values. And for direct bandgap materials, lifetime measurement often includes the SRH and radiative recombinations. In order to calculate the effect of SRH recombination, the contribution of radiative recombination to the lifetime should be excluded resulting in longer lifetimes. Therefore, it is not very likely to have SRH lifetimes shorter than 1 ns for reasonable quality epitaxial materials in reality. The calculation error from inaccurate SRH lifetimes should be below 1.8% without solar concentration.

Radiative recombination is another loss mechanism that can be important in direct bandgap solar cells. Figure 3.7 shows conversion efficiency

dependence on radiative recombination coefficients. Published values for the radiative coefficients for most II-VI and III-V materials are around 1×10^{-10} cm^3/s [71]. In the simulations of the GaAs solar cell, 1.5×10^{-10} cm^3/s is used and when varied from 1×10^{-11} to 1×10^{-9} cm^3/s the conversion efficiency changes by less than 1%. Similarly, when the electron effective mass is varied from 0.01 to 0.2 the efficiency varies by less than 3.5%. And when the hole effective mass is varied from 0.05 to 1.0 the efficiency also varies by less than 3.5%. The results are shown in Fig. 3.8

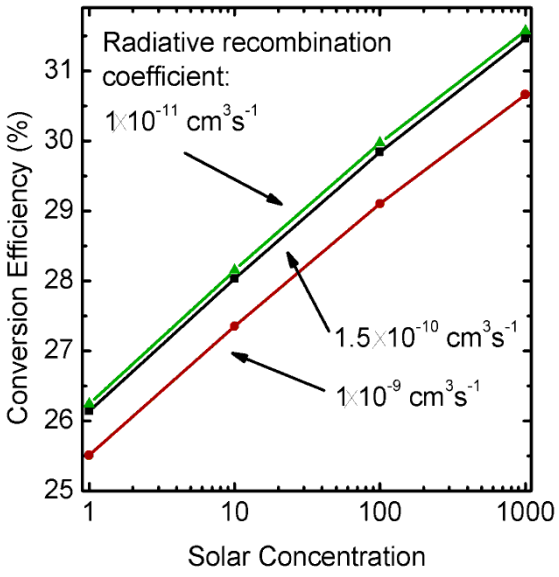

Fig. 3.7. Conversion efficiency with different radiative coefficients.

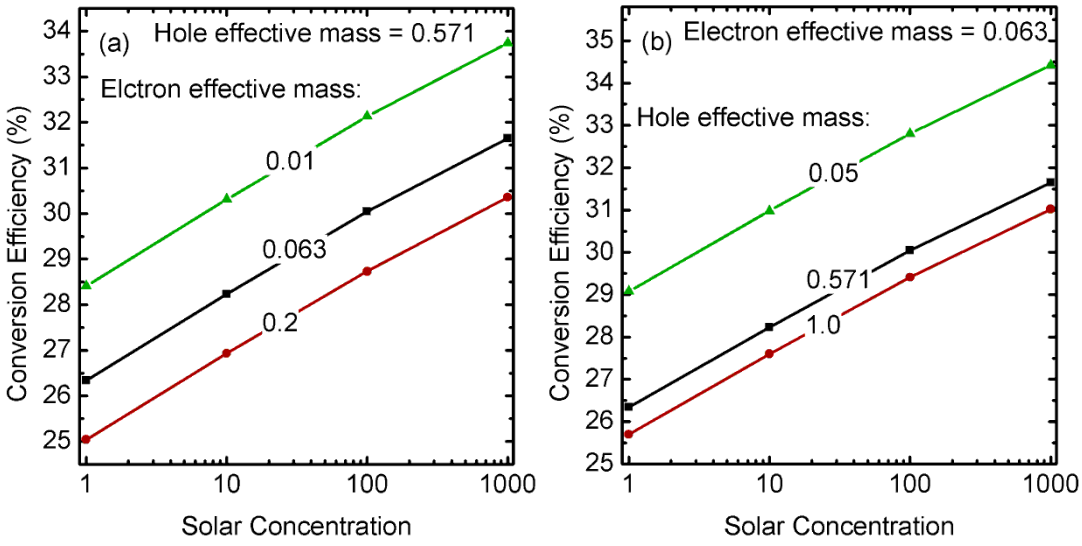

Fig. 3.8. Conversion efficiency with different carrier effective mass and solar concentration: (a) hole effective mass is kept at 0.571; (b) electron effective mass is kept at 0.063.

Moreover, when the electron and hole mobilities are varied two orders of magnitude, the resulting change in conversion efficiency is about 1.5% at most and the results are shown in Fig. 3.9. It is interesting to note that when the mobility is extremely high, the conversion efficiency drops. To explain this, the current flow inside the device need to be carefully analyzed. In the simulated device structure, there are two regions with strong electric field at the n^+p and pp^+ interface, respectively. The electric field can help to move electrons towards the top n contact. And inside the n^+ and p regions, where no electric field is present,

the diffusion current help to move the electrons towards the top n contact. Therefore, higher mobility is helpful for collecting the electrons. However, inside the p^+ region, there is no electric field and the electrons are moved towards the bottom p contact also by diffusion. Therefore, increased mobility also results in increased leakage current at the p contact and the working current is reduced. The overall effect is a competition between increased electron collection at n contact and leakage at p contact. However, the effect of increased leakage current at the p contact generally happens with extremely high mobility due to the small electron concentration close to p contact.

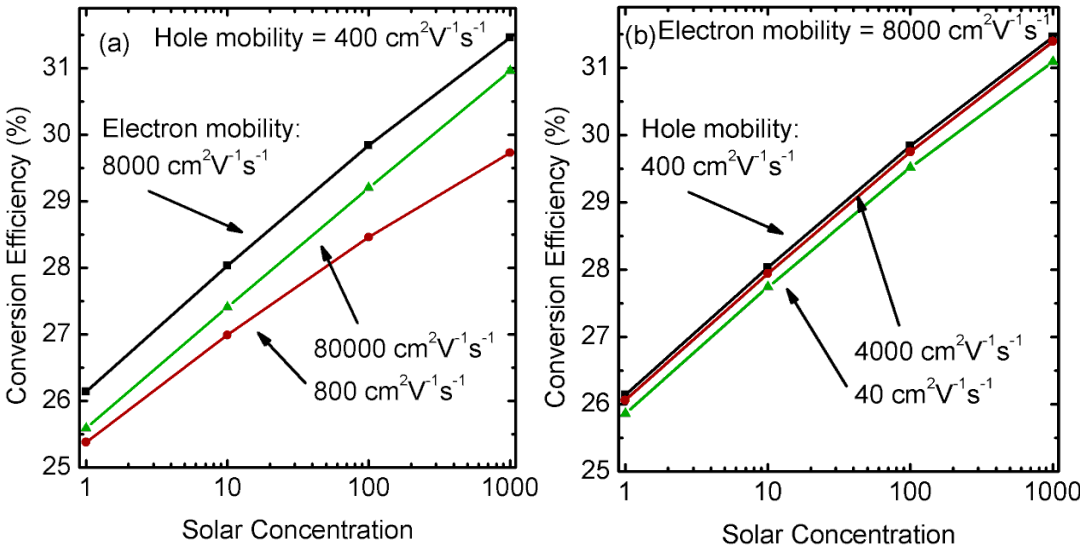

Fig. 3.9. Conversion efficiency with different carrier mobilities and solar concentrations: (a) hole mobility is kept at 400 $cm^2V^{-1}s^{-1}$; (b) electron mobility is kept at 8000 $cm^2V^{-1}s^{-1}$.

The efficiency trends as function of parameter value are similar for the other direct bandgap cell materials. It should be noted that in all the above calculations, 1% efficiency change corresponds to less than 4% relative calculation error. Based on these findings, it can be concluded that the absolute accuracy of the material parameters is not critical as long as the values fall within a reasonable range for good-quality, lattice-matched, crystalline material.

3.3 Optimization of Single Junction Solar Cell Structure

Optimization of single junction solar cell is the basis for multi-junction solar cell optimization and therefore is introduced first. In a single junction solar cell, a lightly doped layer is usually sandwiched between two highly doped layers, namely window and BSF layer. Therefore, two types of structures are available, namely $n^+(n/p)p^+$ and $p^+(n/p)n^+$ structures with the first highly doped layer on the top. The detailed optimization of $n^+(n/p)p^+$ type GaAs cell is discussed first under AM1.5G spectrum and followed by the discussion of $p^+(n/p)n^+$ structure. In the optimization process, values of each layer thickness and doping level need to be determined.

To start the optimization process, the total cell thickness needs to be determined first. The total cell thickness is a tradeoff between the fraction of

solar radiation absorbed and the fraction of photogenerated carriers parasitically lost, both of which increase with cell thickness. For high-quality GaAs solar cell this optimum coincides with the absorption of more than 99% of the solar power above its bandgap. Moreover, the total cell thickness should be within a few micro meters because typical epitaxial material growth is rather slow and on the order of 1 μm/h. Figure 3.10 shows the conversion efficiency and absorption percentage dependence on total thickness. Figure 3.11 shows a typical cell structure to start the optimization.

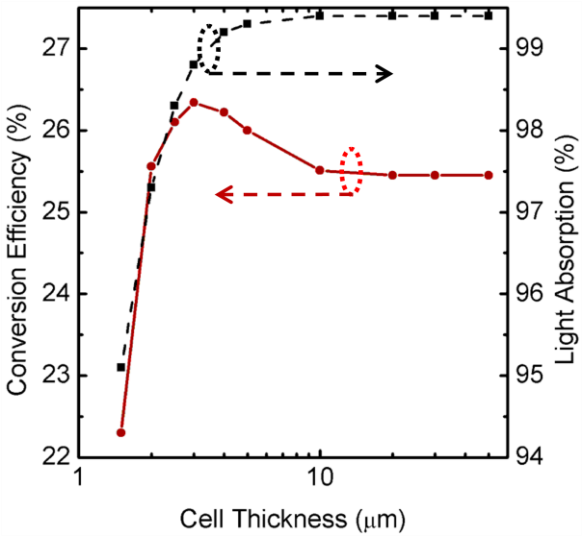

Fig. 3.10. Conversion efficiency and absorption percentage with different total cell thickness.

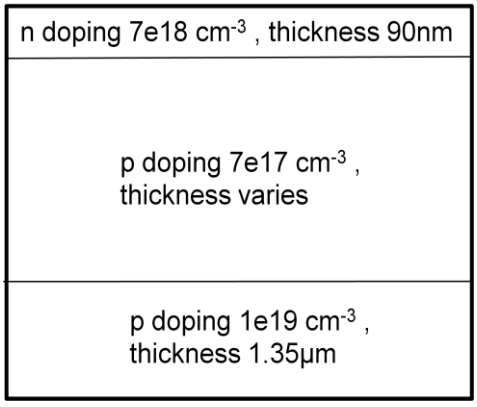

Fig. 3.11. Typical cell structure for optimization.

After the total cell thickness is determined, the three layers inside the cell need to be determined. The lightly doped layer is mainly used to absorb the sun light and therefore is the thickest to start with. The window and BSF layers are usually thin but should be thicker than 10nm due to practical device processing issues. High doping levels in window and BSF layers can help provide a large potential barrier and usually improve the quantum efficiency. Although the p-type GaAs can reach 10^{20} cm^{-3} [101], the p and n-type layer doping is limited below 10^{19} cm^{-3} in the calculation, since it is a typical doping level achievable for most II-VI and III-V semiconductors and extremely high doping levels can cause noticeable efficiency drop due to bandgap narrowing.

From the starting device shown in Fig. 3.11, the window layer thickness and doping is gradually changed and the results are shown in Fig. 3.12 (a) and (b), respectively. Then the BSF layer is optimized following the same procedure and results are shown in Fig. 3.13 (a) and (b). Finally, the doping of the intrinsic layer is optimized. The results are shown in Fig. 3.14 and device with light p-doping performs better. This is because the hole mobility or diffusion length is much smaller than electron and a strong electric field is needed to help the holes generated close to the top surface to move faster down to the bottom contact.

Now a better design than the starting design is achieved after one round of optimization. In order to achieve the best design, an iteration technique is required. Therefore, one more round of optimization is performed starting with window layer. The final design is shown in Fig. 3.15 with a one sun AM1.5G conversion efficiency of 26.4% compared with the record efficiency of 26.1% [14]. The $p^+(n/p)n^+$ type of structure can also be optimized using the above procedure and the p^+pn^+ design gives conversion efficiency of 25.6%.

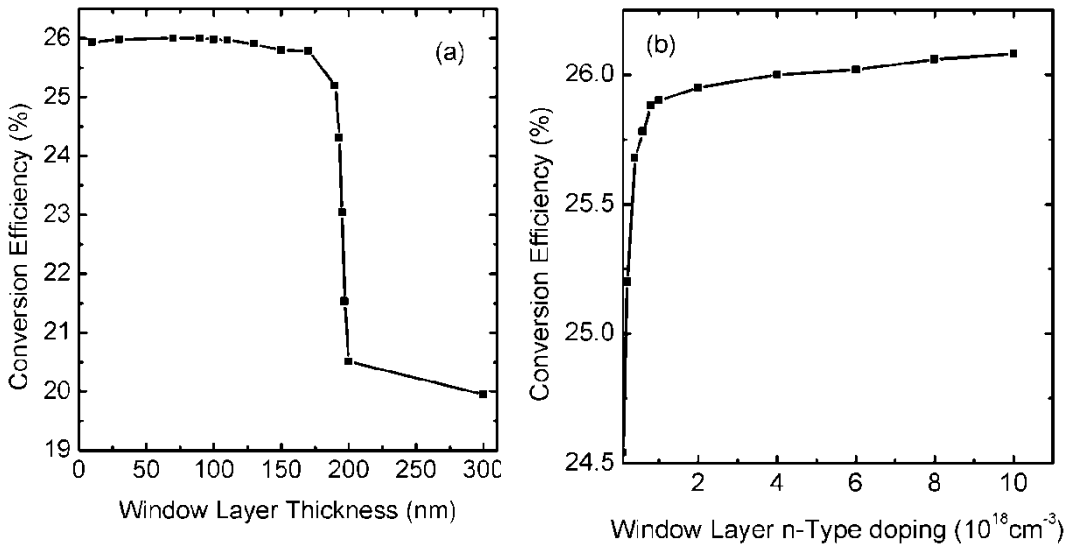

Fig. 3.12. (a) Conversion efficiency with different window layer thickness. (b) Conversion efficiency with different window layer doping level.

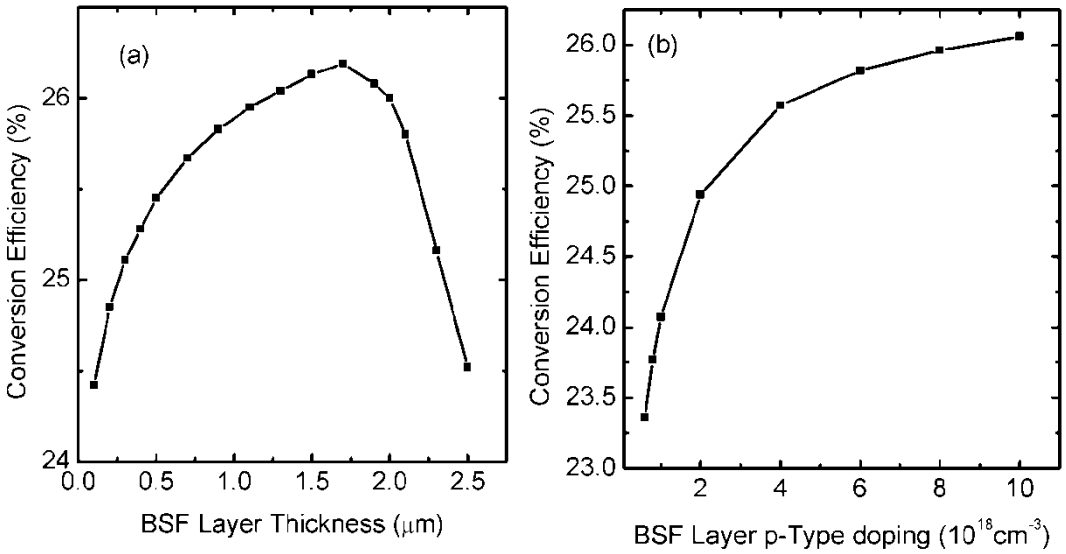

Fig. 3.13. (a) Conversion efficiency with different BSF layer thickness. (b) Conversion efficiency with different BSF layer doping level.

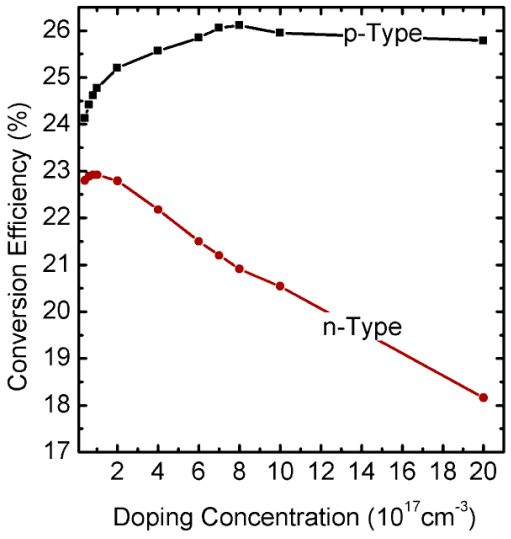

Fig. 3.14. Conversion efficiency with different intrinsic layer doping.

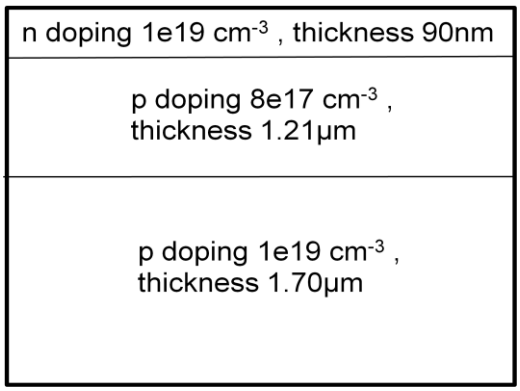

Fig. 3.15. Layer design of the optimized GaAs solar cell.

3.4 Simulation and Design Principles for Multi-Junction Solar Cells

The most straight forward way to simulate the multi-junction (MJ) solar cells is to put all the subcells together and simulate their performance as one device. Although it is possible to do this in Silvaco, the calculation load is extremely high, especially that one needs to take into account the three tunnel junctions connecting the subcells. Moreover, tunnel junctions are best simulated using full quantum transport models such as NEMO1D instead of Silvaco's empirical models [92]. In order to simulate tunnel junctions using Silvaco's empirical tunneling models, carefull calibration with experimental results is necessary. Due to the lack of experimental data, a reliable simulation using Silvaco is not accessible. Therefore, the MJ cell is simulated through the combination of individual simulation results of the subcells in this work. The effect of tunnel junctions is neglected since the differential resistance is quite small when tunneling happens [102, 103] and the voltage drop is usually below 1 mV. The absorption is also quite low for such a thin junction.

Based on the monolithically grown II-VI and III-V material system, the design of MJ cells involves the selection of a set of optimum bandgaps. This material system covers the entire solar spectrum that allows the N-junction solar

cell to arbitrarily partition and absorb the solar spectrum in N sections, using each of its respective N subcell junctions; starting with the absorption of the highest energy solar spectrum partition in the first subcell and the transmission of the lower energy partitions through to the next subcell; and so on until all of the spectrum partitions are absorbed and the unused solar radiation below the smallest bandgap energy is transmitted through the last subcell. Next the bandgap energy of each subcell is adjusted so that each individual subcell operates at the same maximum power operating current, I_m; an operating condition called "current matched". Simultaneously, the structure of each subcell is optimized according to the previous section. Then while maintaining the current matched condition, the bandgap energy of each subcell is systematically moved across the solar spectrum until the overall efficiency, and hence power output, of the entire N-junction device is maximized.

However the model does not consider the following losses as discussed previously: i) top contact shadowing that can be in principle eliminated using transparent contact materials such as, indium tin oxide or ZnO; ii) parasitic absorption at energies below the bandgap which is typically negligible in high-quality lattice-matched materials; iii) absorption in small bandgap tunnel junctions that can be overcome using larger bandgap materials; iv) tunnel junction

transport losses that according to published data [102, 103], are negligible under low concentration and only become noticable at concentrations greater than 100 suns; v) front surface reflection that can be reduced by multilayer coating; and vi) contact resistance that can be reduced by improved contact design; vii) surface recombination that can be reduce by surface passivation or using window and BSF layers. And this work tries to give a practically achievable conversion efficiency limit compared with the detailed balance model [31, 91]. By "achievable conversion efficiency", it means the calculation uses real material parameters and considers position-dependent carrier generation and recombination.

3.5 Four-Junction Solar Cell Designs for AM0 Solar Spectrum

Following the optimization process introduced in section 3.4, the performance of 4 four-junction solar cell designs is calculated using the AM0 spectrum with concentrations from 0.1 to 10 suns (Designs I through IV). The AM0 designs are optimized for a solar concentration of 1 sun, which nicely cover the 0.1 to 10 sun concentration range applicable to space applications within the solar system with little loss in performance compared to using designs optimized for each concentration. Figure 3.16 shows the individual subcell efficiencies for Designs I (Fig. 3.16 (a)) and IV (Fig. 3.16 (b)) where efficiency is defined as the

ratio of the generated electrical power versus the total incident solar power. Figure 3.17 shows the overall solar cell performance of Design I, II, III, and IV. The 1 sun AM0 conversion efficiencies are 40%, 41%, 42%, and 43% for Designs I through IV. The simulated efficiencies are less than the detailed-balance limit of 49% for 1 sun AM0 [91]. The material composition, bandgap energy (E_g), and junction thickness (d) for these four different AM0 four-junction solar cell designs are listed in Table 3.4. A thorough discussion of each individual design follows.

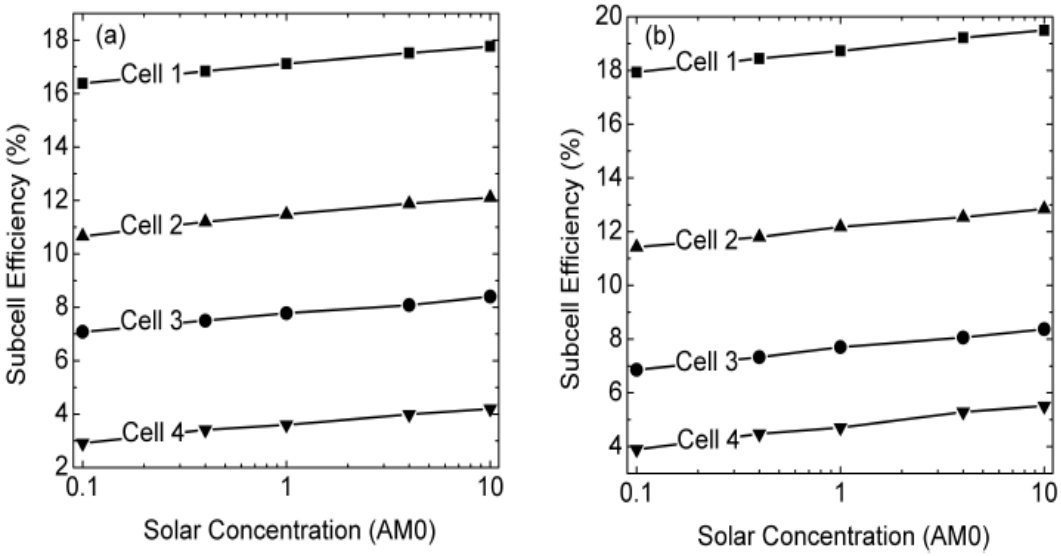

Fig. 3.16. Subcell energy conversion efficiencies: (a) Design I and (b) Design IV.

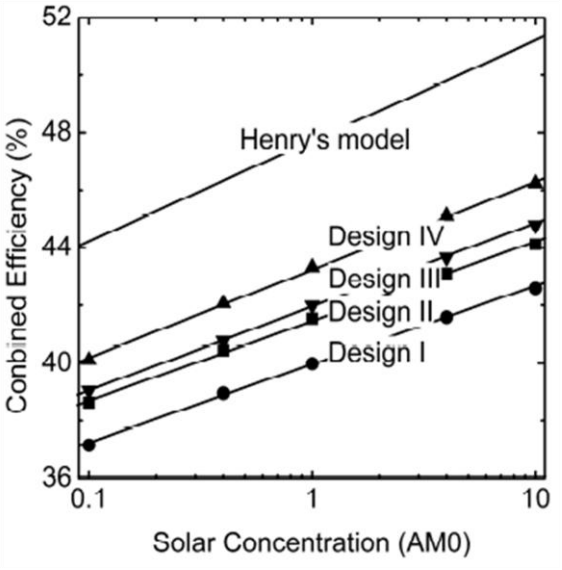

Fig. 3.17. Energy conversion efficiency for four different AM0 four-junction solar cell designs. The theoretical limit given by Henry's model is shown for comparison.

Table 3.4. Material composition, bandgap energy (E_g), and junction thickness (d) for four different AM0 four-junction solar cell designs, ranging from the most practical Design I to optimal Design IV.

Design I			Design II		
Material	E_g (eV)	d (μm)	Material	E_g (eV)	d (μm)
ZnTe	2.27	1.20	ZnTe	2.27	1.20
$Zn_{0.27}Cd_{0.73}Se_{0.66}Te_{0.34}$	1.71	1.20	$Zn_{0.27}Cd_{0.73}Se_{0.66}Te_{0.34}$	1.71	1.20
$Al_{0.41}Ga_{0.59}As_{0.03}Sb_{0.97}$	1.33	1.70	$Al_{0.41}Ga_{0.59}As_{0.03}Sb_{0.97}$	1.33	1.70
GaSb	0.72	2.10	$Al_{0.20}Ga_{0.80}As_{0.02}Sb_{0.98}$	1.04	2.30

Design III			Design IV		
Material	E_g (eV)	d (μm)	Material	E_g (eV)	d (μm)
$Zn_{0.92}Cd_{0.08}Se_{0.09}Te_{0.91}$	2.20	1.20	$Zn_{0.86}Cd_{0.14}Se_{0.14}Te_{0.86}$	2.14	1.20
$Zn_{0.10}Cd_{0.90}Se_{0.81}Te_{0.19}$	1.63	1.20	$CdSe_{0.90}Te_{0.10}$	1.56	1.30
$Al_{0.35}Ga_{0.65}As_{0.03}Sb_{0.97}$	1.25	1.75	$Al_{0.30}Ga_{0.70}As_{0.03}Sb_{0.97}$	1.18	2.10
$Al_{0.13}Ga_{0.87}As_{0.01}Sb_{0.99}$	0.94	2.40	$Al_{0.08}Ga_{0.82}As_{0.01}Sb_{0.99}$	0.86	2.50

Design I uses the II-VI binary ZnTe as the largest bandgap junction (subcell 1) and the III-V binary GaSb as the smallest bandgap junction (subcell 4). Such a choice of the bandgaps for subcells 1 and 4 is advantageous for simplicity and ease of manufacturing but is less than ideal for maximum conversion efficiency. Quaternary materials are chosen for the remaining two subcells such that the best possible overall performance is achieved given the constraint of two less than ideal binary bandgaps. Furthermore, since the overall solar power conversion efficiency is mainly influenced by the largest bandgap junction, the best performance is achieved when the bandgaps of subcells 2 and 3 are selected so that they are current matched to subcell 1. Moreover, since the GaSb bandgap is smaller than that required for current matching to the first three junctions, subcell 4 can be current matched by selecting an adequate thickness that allows some above bandgap solar radiation to be transmitted through the GaSb layer. This however provides an output power that is less than the maximum attainable for the GaSb junction. Therefore, to optimize Design I, the thicknesses of the GaSb junction is selected to attain the largest possible working voltage at the working current (I_m) of the entire solar cell, which is dictated by the first three junctions.

In Designs II, III, and IV the restriction of using two binaries is lifted so that all subcells are perfectly current matched by optimizing the bandgaps of at least three of the junctions. Design II is a modification of Design I, where GaSb is replaced by larger bandgap AlGaAsSb in subcell 4 so that all four junctions are current matched. This design revision increases the efficiency from 40% to 41%. Design III is a modification of Design II, where the bandgaps of all subcells are decreased further to capture more of the AM0 solar spectrum while maintaining the current matched condition; this improves the efficiency from 41% to 42%. Design IV is a modification of Design III, where the bandgaps of all 4 subcells are decreased further to capture even more of the AM0 solar spectrum while maintaining the current matched condition. In this final design the smallest lattice matched bandgap available for the II-VI material system is utilized in subcell 2; this increases the efficiency from 42% to 43%.

To capture even more of the AM0 spectrum the material for subcell 2 has to be changed from II-VI to III-V, which adds the complication of using an indirect bandgap material when the bandgap of subcell 2 falls in the 1.55 – 1.35 eV range where the Al mole fraction is large (see dashed part of the AlGaSb curve in Fig. 2.3). This results in a much thicker junction that is more challenging to grow and that potentially affects the performance of subcell 2; negating the

overall performance gains achieved by further reducing the bandgaps of the other junctions. Nevertheless, assuming that direct bandgap materials are available, the optimal bandgap for subcell 2 is 1.53 eV, which offers an increase in efficiency that is less than 0.1%. Therefore, from a practical point of view, Design IV is the optimal four-junction design for the AM0 spectrum.

3.6 Four-Junction Solar Cell Designs for AM1.5D Solar Spectrum

Following the same optimization process, the performance of 2 four-junction solar cell designs is calculated using the AM1.5D spectrum with concentrations from 1 to 1000 (Designs V and VI). The AM1.5D designs are optimized for a solar concentration of 100 suns, which nicely covers the 1 to 1000 sun concentration range applicable to terrestrial photovoltaic applications. Due to absorption and scattering in the atmosphere, the AM1.5D terrestrial solar spectrum is very different from the AM0 spectrum. Therefore, the four-junction solar cell designs for terrestrial applications vary considerably from those for space applications. Figure 3.18 shows the individual subcell efficiencies for Designs V (Fig. 3.18 (a)) and VI (Fig. 3.18 (b)). Figure 3.19 shows the overall solar cell performance of Design IV. The 1 sun AM1.5D conversion efficiencies are 44% and 46% for Designs V and VI while the 454 sun conversion efficiencies are 53% and 54%, respectively. The simulated efficiencies are less than the

detailed-balance limit of 51% for 1 sun AM1.5D, and 60% for 454 suns AM1.5D given by Henry's model [91]. The material composition, bandgap energy (E_g), and junction thickness (d) for these two different AM1.5D four-junction solar cell designs are listed in Table 3.5. A thorough discussion of each individual design follows.

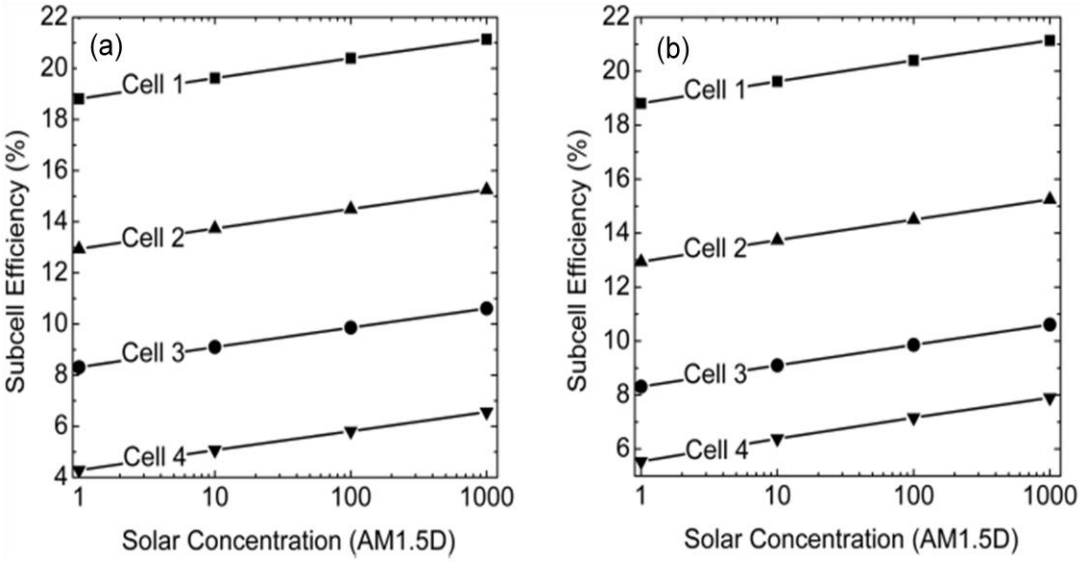

Fig. 3.18. Subcell energy conversion efficiencies: (a) Design V and (b) Design VI.

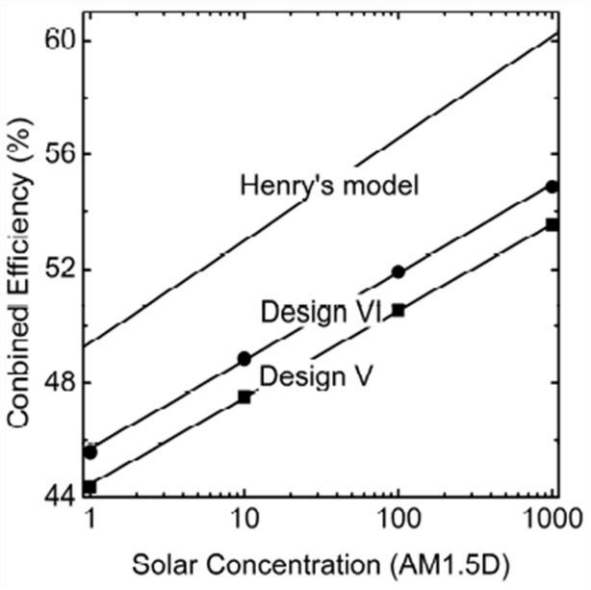

Fig. 3.19. Energy conversion efficiency for two different AM1.5D four-junction solar cell designs. The theoretical limit given by Henry's model is shown for comparison.

Table 3.5. Material composition, bandgap energy (E_g), and junction thickness (d) for two different AM1.5D four-junction solar cell designs.

Design V			Design VI		
Material	E_g (eV)	d (μm)	Material	E_g (eV)	d (μm)
$Zn_{0.76}Cd_{0.24}Se_{0.23}Te_{0.77}$	2.04	1.20	$Zn_{0.76}Cd_{0.24}Se_{0.23}Te_{0.77}$	2.04	1.20
$CdSe_{0.90}Te_{0.10}$	1.56	1.30	$CdSe_{0.90}Te_{0.10}$	1.56	1.30
$Al_{0.32}Ga_{0.68}As_{0.03}Sb_{0.97}$	1.21	2.10	$Al_{0.32}Ga_{0.68}As_{0.03}Sb_{0.97}$	1.21	2.10
GaSb	0.72	2.10	$Al_{0.13}Ga_{0.87}As_{0.01}Sb_{0.98}$	0.92	2.50

During the AM1.5D design process, both binaries ZnTe and GaSb were tested as possible candidates for the largest and smallest bandgaps. However, using ZnTe for the largest bandgap subcell provides much less current than that necessary to achieve a reasonable conversion efficiency because the solar power in the blue region of the AM1.5D spectrum is considerably lower compared to the AM0 spectrum. Therefore, in the most practical AM1.5D design (Design V), only the GaSb binary is beneficial. Moreover, to achieve current matching to the GaSb subcell, the bandgap of subcell 2 would need to be 1.49 eV, which

undesirably requires the use of an indirect bandgap material. Consequently, similar to what is done in Design IV, the smallest available direct bandgap material $CdSe_{0.90}Te_{0.10}$ is chosen for subcell 2 in Design V. Subsequent to Design I, the materials for junction 1 and 3 are selected so that the top three junctions are current matched. And since the subcell 4 (GaSb) bandgap is smaller than that required for current matching to the first three junctions, the thickness of the GaSb junction is selected to attain the largest possible working voltage. The efficiency of Design V is 44% under 1 sun AM1.5D and 54% under 1000 suns. Assuming that a 1.49 eV direct bandgap material is available for subcell 2, the efficiency would increase by less than 2% under both 1 sun and 1000 suns.

In Design VI the efficiency is further improved by replacing GaSb with larger bandgap AlGaAsSb in subcell 4 so that all four junctions are current matched. This results in one ternary and three quaternary subcells and increases the AM1.5D 1 sun efficiency from 44% to 46% and the 1000 sun efficiency from 54% to 55%. Again any further increase in conversion efficiency requires the bandgap energy of subcell 2 to be decreased. Assuming a direct bandgap material is available; the optimal subcell 2 bandgap would also be 1.49 eV and the 1 sun and 1000 sun efficiencies would increase by less than 1%. Therefore,

Design VI is the optimal AM1.5D design for this material system and its performance is within 1% of the best possible AM1.5D four-junction design.

IV. CONCLUSION

The fundamental loss mechanisms of solar cells are indentified, including transmission loss, thermal relaxation loss, spatial relaxation loss and recombination loss. For a GaAs single junction solar cell, the transmission loss, thermal relaxation loss, and spatial relaxation loss account for 34%, 20% and 11% of the total efficiency loss, respectively. Moreover, the spatial relaxation loss and recombination loss are closely related. Larger recombination loss results in larger spatial relaxation loss because more voltage is sacrificed to collect carriers. And various techniques to reduce the losses are discussed.

The monolithically integrated II-VI and III-V materials system is proposed for multi-junction solar cell supplications, which can satisfy both the current- and lattice-matched conditions. This material system possesses continuous energy bandgaps that cover the entire solar spectrum and can be grown lattice matched on GaSb substrate. Based on this material system, new device design principles are discussed and six four-junction solar cells are designed. Ternary or quaternary alloys are needed for various junctions to reach the optimal device performance. In practical designs, however, some performance can be sacrificed in order to improve the viability of the material growth by using less demanding binary materials for some junctions. For the 1 sun AM0 spectrum, the least complicated design uses two binary subcells and offers a conversion efficiency of 40%, while the most complicated optimal design offers a higher conversion efficiency of 43%. For the AM1.5D spectrum, the least complicated design uses one binary subcell and offers a 1 sun conversion efficiency of 44%; while the most

complicated design offers a higher 1 sun conversion efficiency of 46%. These conversion efficiencies are considered as achievable ones because real material properties were used in the calculation. These achievable efficiency limits are smaller than that for the theoretical four-junction conversion efficiencies of 49% for 1 sun AM0 and 51% for 1 sun AM1.5D given by Henry's model. The proposed material system also provides the possibility of making 5-, 6- or more junction solar cells.

PART II

V. INTRODUCTION OF SEMICONDUCTOR LUMINESCENCE REFRIGERATION

Solid state coolers based on luminescence refrigeration are quite desirable for many critical applications, especially for space application. This is because they are vibration free compared with traditional Stirling coolers and feature low working temperature compared with thermal-electric coolers. The idea of optical refrigeration in solid state materials was proposed by Pringsheim in 1929 [104]; and cooling was first observed in 1995 using rare-earth doped glass [105]. However, the requirement of an external high power laser makes it challenging for practical applications. Moreover, cooling by rare-earth doped glass materials becomes quite inefficient when temperature drops below 100 K [106].

Therefore, semiconductor coolers based on luminescence refrigeration, another type of solid state coolers, have received much interest. They may achieve temperatures ~10 K and below compared with rare-earth doped glass [106]. Moreover, they can work under both optical and electrical injection [106, 107-112] and can be easily integrated with other semiconductor devices making them more useful than rare-earth doped glass coolers. The fundamental theories of semiconductor photoluminescence and electroluminescence refrigeration are discussed as follows.

5.1 Semiconductor Luminescence Refrigeration under Optical Injection

The basic idea of semiconductor luminescence refrigeration under optical injection is illustrated in Fig. 5.1. Photons with energy near the semiconductor bandgap can be absorbed and generate electron-hole pairs. The photo-generated

electrons and holes radiatively recombine and emit photons. However, the electrons and holes cannot all stay at the band edge due to the Pauli Exclusion Principle. Therefore, the average energy of electrons and holes is above and below the conduction and valence band edge, respectively. Moreover, for radiative transitions, electrons and holes need to have the same momentum. Thus, the average energy of the emitted photons is the same as the average energy difference between electrons and holes in the conduction and valence band, respectively. This means that the average energy of the spontaneously emitted photons is larger than that of the absorbed photons and is about $E_g + k_B T$ at low optical injection according to Ref. 33, where E_g is the bandgap energy, k_B is the Boltzmann constant and T is the temperature. The extra energy comes from the absorption of phonons by electrons and holes. Furthermore, net cooling can be achieved if both close to unity internal quantum efficiency and extraction efficiency can be realized.

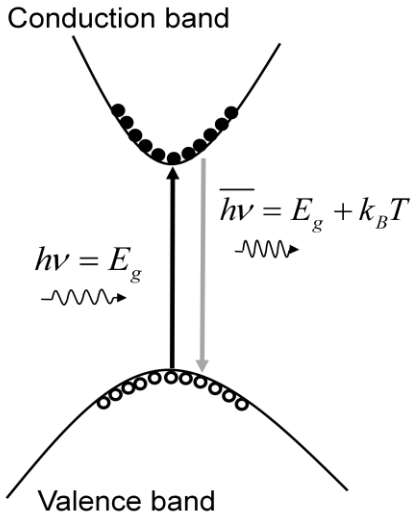

Fig. 5.1. Schematic diagram of the cooling process in semiconductors under optical injection, where E_g is the bandgap energy, k_B is the Boltzmann constant and T is the temperature.

5.2 Semiconductor Luminescence Refrigeration under Electrical Injection

Normally, a semiconductor light-emitting diode (LED) is a heater under high external bias (e.g. larger than the bandgap). However, it can become a net cooler under low electrical injection if both the internal quantum efficiency and extraction efficiency are close to unity. The fundamental refrigeration mechanism under electrical injection is more complicated compared with refrigeration under optical injection and is clarified in Ref. 109. In order to understand the refrigeration process, the carrier transport in the device needs to be carefully investigated. Figure 5.2 illustrates the band diagram of an electrically injected quantum-well (QW) LED, where E_{Fn} and E_{Fp} are the electron and hole quasi-

Fermi levels, respectively. ΔE_n and ΔE_p are the cooling contribution per electron and hole, respectively. The device can be divided into three regions, namely contact, bulk semiconductor, and QW regions. In the n-contact region, there is a highly doped layer right beneath the metal contact. Due to the high doping level, the Fermi level is slightly above the conduction band edge. Moreover, a narrow spike at the metal-semiconductor interface is formed due to the difference between metal work function and semiconductor electron affinity. If the doping is high enough, the spike becomes very thin and carriers can tunnel through the spike easily. Then the ohmic contact assumption can be applied. The height and width of the spike is represented by the specific contact resistance. The doping level inside the semiconductor is lower and a gradual potential barrier is formed. Once electrons get into the semiconductor through tunneling, they need to absorb phonons in order to climb up the potential barrier and move to the QW region. Due to the absorption of phonons, this transport process is a cooling process. When electrons travel to the QW region, they fall to bound states and release phonons, making this transport process a heating process. Holes travel to the QW region following similar processes. Electrons and holes inside the QW can radiatively recombine and emit photons. If the quasi-Fermi level separation is smaller than the average energy of emitted photons, net cooling can be realized.

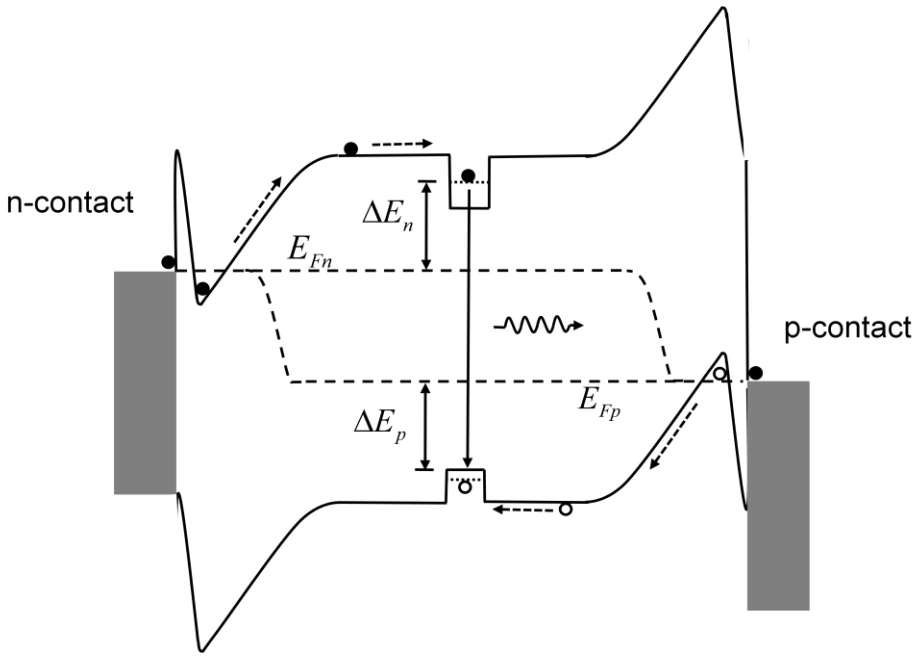

Fig. 5.2. Schematic diagram of the cooling process in an electrically injected quantum well LED, where E_{Fn} and E_{Fp} are the electron and hole quasi-Fermi levels, respectively. ΔE_n and ΔE_p are the cooling contribution per electron and hole, respectively.

However, many practical issues have to be overcome before demonstration of refrigeration using this type of LEDs. Firstly, electrically injected carriers can recombine non-radiatively and generate heat. Therefore, extremely high quality material is needed to increase the spontaneous emission quantum efficiency to close to unity. Secondly, the carrier leakage has to be minimized trough careful device design, since the carrier leakage is a heating process and lowers the internal quantum efficiency. Thirdly, the absorption of photons by metal contacts has to be quite small to avoid heating. Lastly, the

luminescence extraction efficiency needs to be very high in order to avoid re-absorption of photons. But the luminescence extraction efficiency is usually limited by the high refractive index of the semiconductor. Until now, refrigeration in electrically injected semiconductor devices has not been realized yet.

VI. NUMERICAL SIMULATION OF SEMICONDUCTOR LUMINESCENCE REFRIGERATION DEVICE

A specially designed semiconductor light-emitting diode (LED) working at low injection levels is one of the most promising candidates for semiconductor luminescence refrigeration with straightforward electrical input. However, it is quite challenging to realize cooling using an LED and two important conditions must be met: i) close to unity internal quantum efficiency, and ii) close to unity extraction efficiency. In this chapter, a practical device is proposed for semiconductor luminescence refrigeration and numerical simulations are carried out to predict the performance.

6.1 A Practical LED Device for Semiconductor Luminescence Refrigeration

A schematic diagram of the proposed device, which monolithically integrates a thin slab LED and an anti-reflection (AR) coated GaAs hemisphere, for luminescence refrigeration is shown in Fig. 6.1. In order to achieve cooling, both the thin slab LED and the hemisphere have to be carefully designed. The requirement for the entire device is close to unity internal quantum efficiency and extraction efficiency. In this work, a high quality InGaAs/GaAs triple quantum-well (QW) structure is used as the active region and grown on GaAs substrate by molecular-beam-epitaxy technique. In previous work, a similar active region demonstrated a spontaneous emission quantum efficiency of 94% at room temperature and over 99% at 100 K [113]. The material growth will be introduced in Chapter 7 and the numerical simulation of the thin slab LED (active

region) will be discussed in Section 6.2.

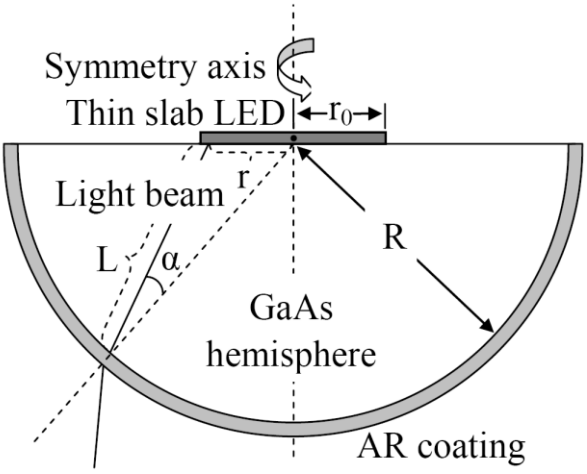

Fig. 6.1. Schematic device structure to achieve luminescence refrigeration.

Another major challenge to the realization of electroluminescence refrigeration in LEDs is that the energy conversion efficiency is limited by poor light extraction caused by the large difference in the refractive indices between semiconductors and air. For example, due to light trapping a planar GaAs LED emits less than 2% of the internally generated spontaneous emission into free space through a given surface. Advanced techniques have been used to increase the luminescence extraction efficiency of LEDs, such as epoxy encapsulation, photonic crystal, and surface roughening [114-116]. Although the use of photonic crystal can give extraction efficiency as high as 73% [117], it is still not enough for cooling purpose. In the proposed device shown in Fig. 6.1, a GaAs hemisphere is used to increase the luminescence extraction efficiency and is

fabricated in the substrate. In this structure the interface reflection between the thin slab LED and the hemisphere is negligible because the respective refractive indices are very closely matched. Contrary to planar structures, a hemisphere device can be designed so that all of the spontaneous emission that falls onto a given point of the hemisphere-air interface lies within the escape cone provided the hemisphere diameter is sufficiently larger than the thin slab LED diameter. The detailed calculation for the extraction efficiency of this hemisphere structure is given in Section 6.3.

6.2 Numerical Simulation of the Thin Slab LED

The numerical simulation of the thin slab LED (active region) is carried out using Silvaco and a schematic diagram of the simulated structure is shown in Fig. 6.2. The material growth cross section is shown in Fig. 6.3 with the right side corresponding to the top of the thin slab LED shown in Fig. 6.1 and 6.2. Different from the simulation of solar cells, a 2D cylindrical coordinate is used. Although it is possible to use the 3D cylindrical coordinate in Silvaco, the 2D simulation greatly saves the calculation time. Moreover, this thin slab LED structure is much more complex than typical solar cell structures and involves more advanced physical models resulting in significantly longer simulation time even using 2D models. The simulation plane and symmetry axis of the 2D cylindrical coordinate are also shown in Fig. 6.3. The physical quantities are only calculated on the 2D simulation plane and the 3D device performance can be interpreted using rotational symmetry. Besides the use of 2D cylindrical

coordinates, there are several other changes from the simulation of solar cells. Effects related to practical device performance, including contact resistance and surface recombination, are considered. Most importantly, advanced physical models including i) transport model, ii) recombination model, iii) quantum model, iv) temperature dependent bandgap model, and v) mobility model are considered. The input parameters are listed in Appendix III.

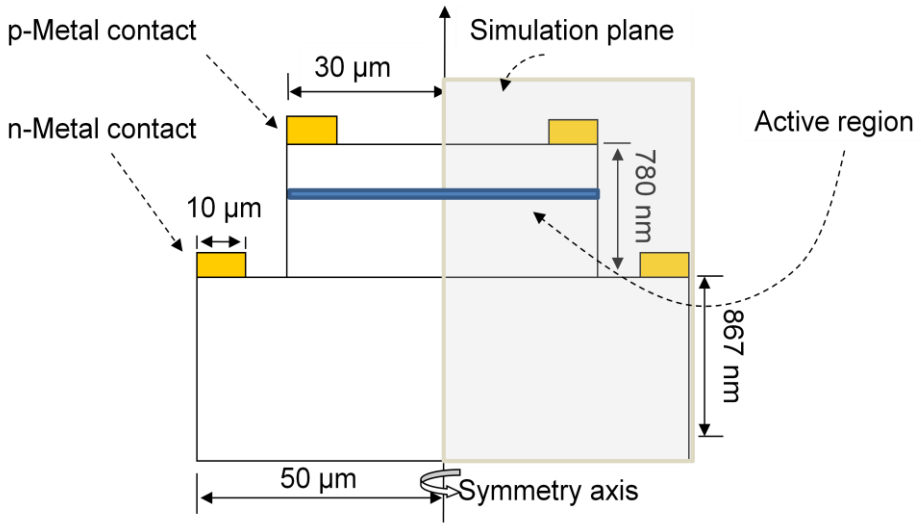

Fig. 6.2. Schematic diagram of the simulated thin slab LED structure.

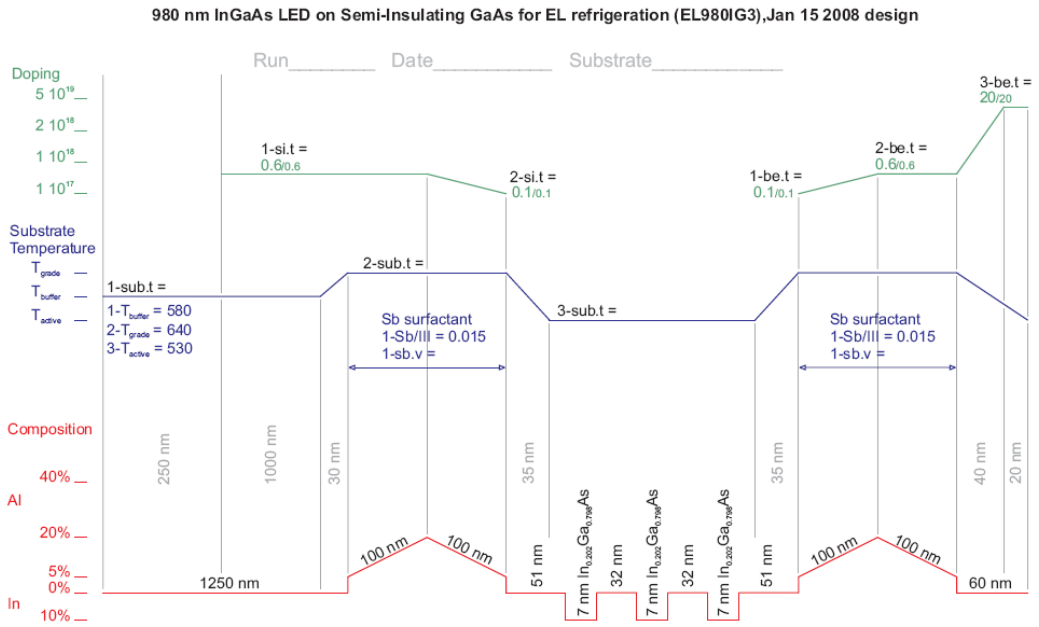

Fig. 6.3. Material growth cross section for the thin slab LED.

6.2.1 Carrier Transport Model

In Silvaco, there are two major carrier transport models, namely the drift-diffusion (DD) and energy balance transport models. Both models come from different levels of approximations to the Boltzmann transport equation. The conventional DD model has been the predominant model for a long time and is quite successful for the traditional semiconductor devices with sizes above 0.5 μm [93]. Therefore, in the simulation of p-n junction solar cells, the DD model is used. However, this model neglects non-local transport effects which are important for deep submicron devices [92]. In the DD model, the carrier temperature is assumed to be the same as the lattice temperature and the driving force of current comes from the local electric field and carrier density gradient.

But in the presence of strong electric field, electrons can gain energy from the field resulting in higher electron temperature than the lattice temperature. This electron temperature gradient provides an extra driving force for the current, since the electron gas pressure is proportional to the electron temperature [93]. Due to the temperature difference between carriers and the lattice, there will be energy transfer between them. The energy balance transport model takes this nonlocal effect into account and represents a higher order of approximation to the Boltzmann transport equation. In this thin slab LED active region, strong electric fields exist at many hetero-interfaces and therefore the energy balance transport model is used.

In the energy balance transport model, the electron and hole current densities are modified to in include the effect of carrier temperature gradient and given as [92]

$$\vec{J}_n = qD_n \nabla n - q\mu_n n \nabla \Psi + qnD_n^T \nabla T_n \quad , \tag{6.1}$$

$$\vec{J}_p = -qD_p \nabla p - q\mu_p p \nabla \Psi - qpD_p^T \nabla T_p \quad , \tag{6.2}$$

where T_n and T_p are the electron and hole temperatures, respectively. D_n^T and D_p^T are the electron and hole thermal diffusivity, respectively. The energy transfer between carriers and the lattice is expressed as [92]

$$\vec{S}_n = -K_n \nabla T_n - \left(\frac{k\delta_n}{q} \right) \vec{J}_n T_n \quad , \tag{6.3}$$

$$\nabla \bullet \vec{S}_n = \frac{1}{q} \vec{J}_n \bullet \vec{E} - W_n \quad , \tag{6.4}$$

$$\vec{S}_p = -K_p \nabla T_p - \left(\frac{k\delta_p}{q} \right) \vec{J}_p T_p \quad , \tag{6.5}$$

$$\nabla \bullet \vec{S}_p = \frac{1}{q} \vec{J}_p \bullet \vec{E} - W_p \quad , \tag{6.6}$$

where $\vec{S}_n$, K_n and W_n are the electron energy flux density, the thermal conductivity, and the energy density loss rate, respectively. $\vec{S}_p$, K_p, W_p are the corresponding values for holes. Moreover, all carrier temperature (energy) dependent parameters have to be remodeled in the energy balance transport model, such as the mobility and the effective density of states. Detailed expressions of these quantities can be found in Ref. 92.

In the simulated thin slab LED active region, there are quite a few hetero-interfaces where the carriers can gain thermal energy by absorbing phonons and then move across the potential barrier. This contribution to the current is taken care of by the thermionic field emission model provided by Silvaco. The expression of the current at hetero-interfaces is given as [92]

$$\vec{J}_n = q v_n (1+\delta) \left[n^+ - n^- \exp\left(\frac{-\Delta E_C}{kT_L} \right) \right] \quad , \tag{6.7}$$

$$\vec{J}_p = -q v_p (1+\delta) \left[p^+ - p^- \exp\left(\frac{-\Delta E_V}{kT_L} \right) \right] \quad , \tag{6.8}$$

where the current is assumed to flow from the "-" region to the "+" region. $\vec{J}_n$ and $\vec{J}_p$ are the current density for electrons and holes, respectively. v_n and v_p are the thermal velocity for electrons and holes, respectively. The thermal velocity is

proportional to the product of the carrier effective mass and square of the temperature. ΔE_C and ΔE_V are the conduction and valence band energy change from the "-" region to the "+" region, respectively. δ is the tunneling factor and represents the contribution of current from tunneling. Detailed expressions for v_n, v_p, and δ can be found in Ref. 92.

6.2.2 Recombination Models

Besides the carrier transport model, advanced recombination models are also used in this work. The Shockley-Read-Hall (SRH) recombination rate is given as [92]

$$R_{SRH} = \frac{pn - n_{ie}^2}{\tau_{p0}\left(n + n_{ie}\right) + \tau_{n0}\left(p + n_{ie}\right)} \quad , \tag{6.9}$$

where n_{ie} is the intrinsic carrier concentration. τ_{n0} and τ_{p0} are the electron and hole SRH lifetimes, respectively. To take into account the temperature dependence, the SRH recombination lifetimes of GaAs and $In_{0.202}Ga_{0.798}As$ are taken from fittings of temperature dependent lifetime measurement data in Ref. 33 and listed in Appendix III.

Auger recombination is also included, since the injection level is quite high inside the quantum-well regions. The expression for the Auger recombination rate is given as [92]

$$R_{Auger} = AUGN \bullet \left(pn^2 - nn_{ie}^2\right) + AUGP \bullet \left(np^2 - pn_{ie}^2\right) \quad , \tag{6.10}$$

where *AUGN* and *AUGP* are the electron and hole Auger recombination coefficients, respectively. To take into account the temperature dependence of

Auger recombination coefficients, the Klaassen's model is used and given as [92]

$$AUGN(T_L) = AUGN_{300}\left(\frac{T_L}{300}\right)^{1.18} , \tag{6.11}$$

$$AUGP(T_L) = AUGP_{300}\left(\frac{T_L}{300}\right)^{0.72} , \tag{6.12}$$

where $AUGN_{300}$ and $AUGP_{300}$ are the electron and hole Auger recombination coefficients at 300 K, respectively. T_L is the lattice temperature, which is replaced by the corresponding local carrier temperature in the energy balance transport model.

Moreover, the radiative recombination is taken care of by Li's model instead of the general radiative recombination model used in solar cell simulations. Li's model considers the optical transitions between the conduction band and two valence bands, namely heavy and light hole bands [92]. The spontaneous recombination rate from Li's model is given as [92]

$$r_{sp} = \left(\frac{q}{m_0}\right)^2 \frac{\pi\hbar}{\varepsilon E}\left|M(E)\right|^2 \rho \bullet D(E) \bullet f_j^{'}\left(1 - f_i^{'}\right) , \tag{6.13}$$

where E is the transition energy. $M(E)$ is the transition matrix element. ρ is the density of states. $D(E)$ is the optical mode density. $f_i^{'}$ and $f_j^{'}$ are the Fermi functions for the i th and j th valence and conduction band bound state, respectively. Detailed expressions for these quantities can be found in Ref. 92. It can be seen that Li's model is more physical than the general radiative recombination model, which only calculates recombination rates based on a

constant recombination coefficient. Moreover, Li's model can also give spectral information of the emission, which is important for the calculation of the total emission power.

6.2.3 Quantum Well Model

The incorporation of quantum-wells in the LED device also makes the simulation more complex and quantum models have to be used. In Silvaco, there are several models that can simulate the quantum confinement effect and the General Quantum Well Model is used in this work. This model is based on the self-consistent Schrodinger-Poisson model, which self-consistently solves the Poisson's equation for potential and Schrodinger's equation for bound state energies and carrier wavefunctions [92]. Therefore, this model can predict the gain and spontaneous recombination rates if used with Li's model. But it should be noted that this model cannot be used to study carrier transport problems. Although the Density Gradient and the Bohm Quantum Potential models can both calculate the carrier transport, they do not provide information about bound state energies or wavefunctions. Without the information of bound state energies and wavefunctions, it is not possible to accurately model spontaneous recombination in the quantum-well.

6.2.4 Temperature Dependent Bandgap Model

For GaAs and AlGaAs materials, the universal energy bandgap model is used to describe the temperature dependence of bandgaps and given as [92]

$$E_g(T_L) = EG300 + EGALPHA\left[\frac{300^2}{300 + EGBETA} - \frac{T_L^2}{T_L + EGBETA}\right] \quad , (6.14)$$

where *EG*300 is the bandgap at 300 K. Input parameters *EGALPHA* and *EGBETA* are listed in Ref. 92. At present, Silvaco lacks the capability of evaluating temperature and strain dependent bandgaps for zinc blende materials. Therefore, the temperature and strain dependent bandgap and band alignment of $In_{0.202}Ga_{0.798}As$ is calculated separately using the program developed in Ref. 118 and listed in Appendix III.

6.2.5 Mobility Model

For $In_{0.202}Ga_{0.798}As$ and AlGaAs, the temperature dependent low field mobility model is used and given as [92]

$$\mu_n(T_L) = \mu_{n0}\left(\frac{T_L}{300}\right)^{-1.5} , \tag{6.15}$$

$$\mu_p(T_L) = \mu_{p0}\left(\frac{T_L}{300}\right)^{-1.5} , \tag{6.16}$$

where μ_n and μ_p is the electron and hole mobility, respectively. μ_{n0} and μ_{p0} is the electron and hole mobility at 300 K, respectively. For GaAs, the impurity concentration dependent and parallel field dependent mobility models are used. The concentration dependent mobility model uses a look-up table to find the mobility of GaAs at specific impurity concentrations at 300 K and then use Eqs. 6.14 and 6.15 to calculate the temperature dependence. The look-up table can be found in Ref. 92. The parallel field dependent mobility model is given as [92]

$$\mu_n(E) = \frac{\mu_{n0} + \frac{VSATN}{E}\left(\frac{E}{4\times10^3}\right)^4}{1+\left(\frac{E}{4\times10^3}\right)^4} , \tag{6.17}$$

$$\mu_p(E) = \frac{\mu_{p0} + \frac{VSATP}{E}\left(\frac{E}{4\times10^3}\right)^1}{1+\left(\frac{E}{4\times10^3}\right)^1} \quad , \tag{6.18}$$

where μ_n and μ_p are the electron and hole field dependent mobility, respectively. μ_{n0} and μ_{p0} are the electron and hole low field mobility calculated from the concentration dependent mobility model, respectively. *VSATN* and *VSATP* are the electron and hole saturation velocity, respectively. E is the parallel electric field.

6.2.6 Device Simulation Results

The electrical performance is calculated for both single and triple QW devices under various bias and temperature conditions. It should be noted that the re-absorption of the spontaneous emission through either inter band absorption or free carrier absorption is not considered in this calculation. Therefore, all the spontaneously emitted photons are assumed to get out of the thin slab LED from both top and bottom sides. However, some of the photons may be absorbed through photon recycling and parasitic absorption leading to non-zero photon recycling factor and lower internal quantum efficiency. Moreover, photons may bounce back and forth many times between the two sides before they are extracted in a thin slab LED due to the large refractive index mismatch between semiconductor and air, which further increases re-absorption. Thus, the following results are only valid when photon recycling factor is zero and there is no parasitic absorption loss.

Figure 6.4 shows the I-V characteristic for, (a) single QW design, and (b) triple QW design. It can be seen that the I-V characteristics for single and triple QW devices are similar and the triple QW device has slightly higher current at specific temperature and bias voltage due to more QWs. Figure 6.5 shows the energy conversion efficiency versus bias voltage for, (a) single QW design, and (b) triple QW design. The conversion efficiency is defined as the ratio of total emission power over input power. It can be seen that the energy conversion efficiency increases with decreasing temperatures and is approaching unity when temperature is 150 K.

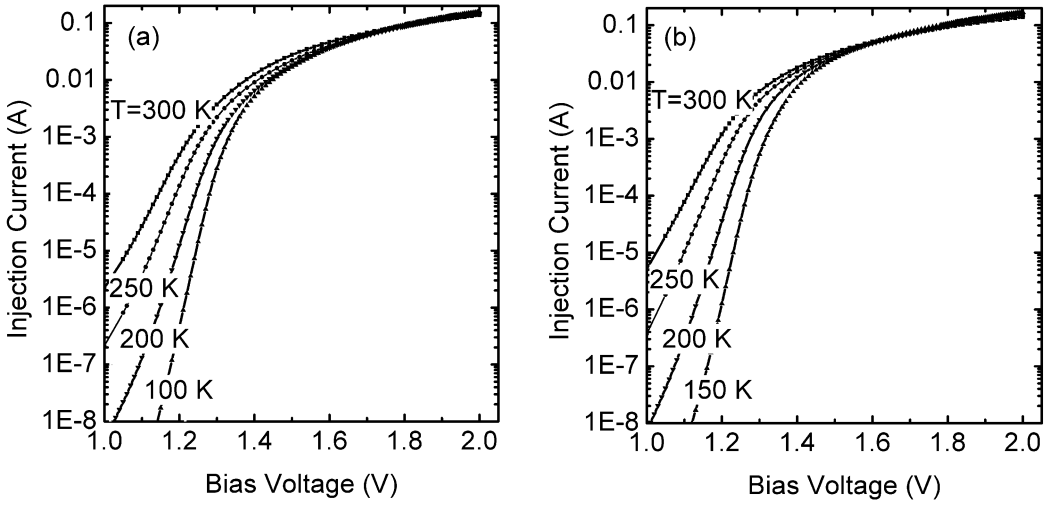

Fig. 6.4. I-V characteristic for, (a) single quantum-well design, and (b) triple quantum-well design.

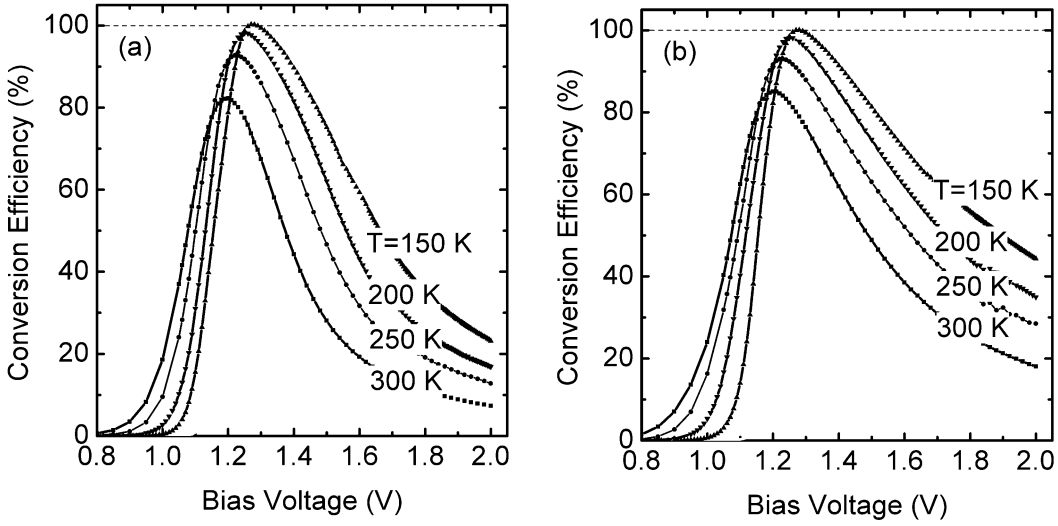

Fig. 6.5. Energy conversion efficiency versus bias voltage for, (a) single quantum-well design, and (b) triple quantum-well design.

While the performance with respect to bias voltage is important for electrical devices, the performance under various temperatures should really be compared at the same injection level instead of the bias voltage. The injection level is defined as the difference between the quasi Fermi level separation and energy bandgap normalized by $k_B T$, where k_B is the Boltzmann constant and T is the lattice temperature. Moreover, the bandgap (or rather minimum transition energy) for QW device increases with decreasing temperatures. Therefore, this definition of injection level takes into account the temperature difference and directly relates to the log of the carrier density inside the QW. Figure 6.6 shows the conversion efficiency versus injection level for, (a) single QW design, and (b) triple QW design. From Fig. 6.6 the highest energy conversion efficiency is

achieved when the quasi Fermi level separation is close to the energy bandgap and the cooling contribution comes from the difference between the carrier ground state energy in the QW and the quasi Fermi level.

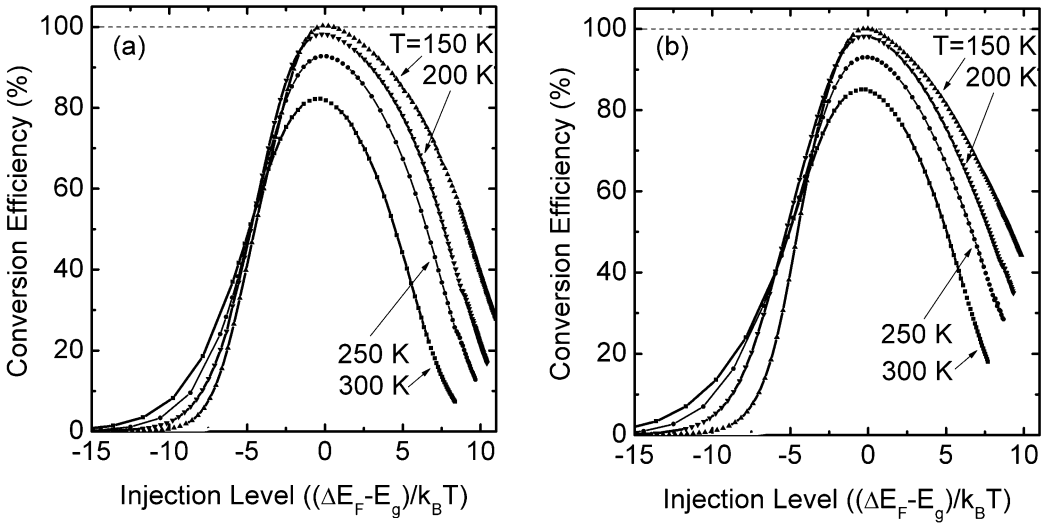

Fig. 6.6. Energy conversion efficiency versus injection level for, (a) single quantum-well design, and (b) triple quantum-well design.

Moreover, from Fig. 6.6 the triple QW device performs better than the single QW device at high injection levels (> 0). There are two major loss mechanisms at high injection levels, namely leakage current loss and Auger recombination loss. The leakage current increases quickly with increasing bias (injection level) due to the fact that the built-in potential, which prevents current leakage, becomes smaller with increasing bias voltage. Figure 6.7 shows the ratio of leakage current over total current versus injection level for, (a) single QW design, and (b) triple QW design. It can be seen that the triple QW device has

much lower leakage current loss compared with single QW device because carriers can be effectively caught by the two extra QWs in the triple QW device. Furthermore, the leakage current increases dramatically with increasing temperature because the QW becomes shallower with increasing temperature due to the reduced band offset. Auger recombination significantly lowers the spontaneous emission quantum efficiency at high injection levels. Figure 6.8 shows the spontaneous emission quantum efficiency versus injection for, (a) single QW design, and (b) triple QW design. It can be seen that the triple QW device performs slightly better than the single QW device at high injection levels. This is because the injection levels of the three QWs in the triple QW device are slightly different resulting in different Auger recombination loss in the QWs and the overall efficiency is higher by using the injection level in the middle QW.

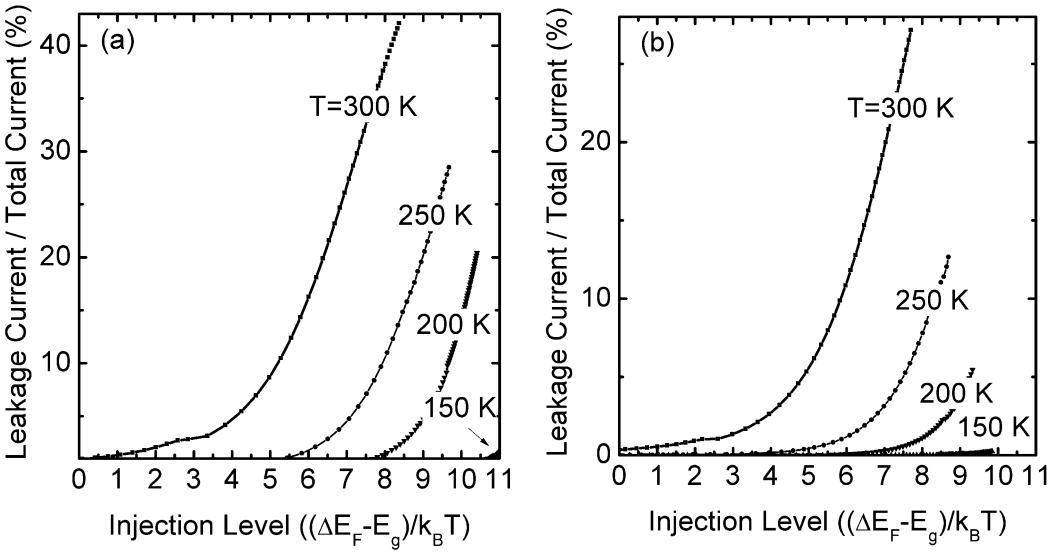

Fig. 6.7. The ratio of leakage current over total current versus injection for, (a) single quantum-well design, and (b) triple quantum-well design.

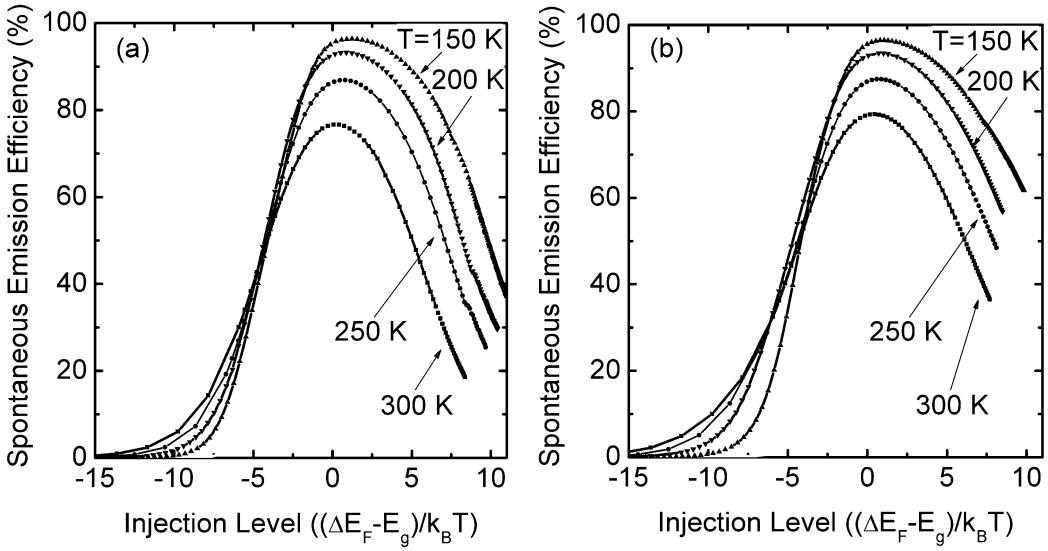

Fig. 6.8. Spontaneous emission quantum efficiency versus injection level for, (a) single quantum-well design, and (b) triple quantum-well design.

6.2.7 Discussion

From Fig. 6.8, the spontaneous emission quantum efficiency for both single and triple quantum well devices is over 96% at optimum injection level (~ 0) and at 150 K due to the high material quality. Although the room to further increase the material quality is limited, higher material quality can help to achieve higher energy conversion efficiency at higher temperature. From Fig. 6.7, the leakage current loss is negligible (< 5e-8) at the optimum injection level (~ 0) and at low temperature (< 150 K). Therefore, in order to demonstrate cooling, the device testing temperature has to be lower than 150 K for the present material quality. However, the calculation at temperatures below 150 K is not carried out

due to the calculation instability and more physics, which are out of the scope of this research, are involved at low temperatures.

6.3 Numerical Simulation of Luminescence Extraction

In the previous section, it is shown that the high quality QW thin slab LED could achieve over 100% energy conversion efficiency under low temperature and optimum injection levels. But there is one implied assumption that the luminescence extraction efficiency is also 100%, which is very hard to achieve due to the large refractive index of the LED material compared with air. In this work, a GaAs hemisphere is monolithically integrated with the previously calculated thin slab LED to increase the luminescence extraction. The basic idea is that the interface reflection between the thin slab LED and the hemisphere is negligible because the respective refractive indices are very closely matched. Therefore, there is no light refraction at the thin slab LED and hemisphere interface. In the limit of infinitely large hemisphere, all the light rays can fall onto the hemisphere-air interface perpendicularly. Thus, there exists a particular hemisphere size that all the light rays can just fall into the escape cone.

Therefore, the largest light ray incident angle within the escape cone at the hemisphere-air interface needs to be calculated for the proposed device structure. Using the law of cosines, as shown in Fig. 6.1, the incident angle, α, can be expressed as

$$\cos(\alpha) = \frac{R^2 + L^2 - r^2}{2RL} \quad , \tag{6.19}$$

where R is the radius of the hemisphere, r is the radial distance from the center to a given point on the surface of the active region, and L is the distance from the corresponding point on the active region surface to the hemisphere surface. The incident angle goes through a maximum at $L^2 = R^2 - r^2$, which occurs when light is emitted perpendicular to the surface of the active region, with $\sin(\alpha) = r/R$. Furthermore, the condition for total internal reflection is given by $\sin(\alpha) > 1/n$, where n is the refractive index, and since the maximum value of r is the active region radius r_0, then as long as $R > nr_0$ all of the spontaneous emission from the active region falls within the escape cone. Moreover, due to the small incident angles, an effective anti-reflection coating is relatively easy to attain.

To evaluate the performance of this design, the extracted fraction of the spontaneous emission leaving the active region of the thin slab LED from the hemisphere side is calculated for various hemisphere sizes with single-layer anti-reflection coatings. The thin slab LED thickness is negligible compared with the hemisphere size and thus there is no spacing between the active region and the hemisphere. The GaAs hemisphere is assumed transparent, since the high quality semi-insulating GaAs substrate is used and the emission from the InGaAs QWs (980 nm) is well below the GaAs bandgap. It is also assumed that the light emission is randomly polarized and uniformly distributed in all directions for the entire active region emission spectrum. Furthermore, in the case where the hemisphere is large enough to eliminate light trapping, the only back reflection loss is due to a less than ideal anti-reflection coating on the hemisphere surface.

As a worst case scenario, the reflected light is assumed to be parasitically lost inside the hemispherical device. An assumption that underestimates the performance as part of the reflected light is extracted as it again reaches the hemisphere surface through multiple reflections. To calculate the AR coating thickness and the extraction efficiency for various hemisphere sizes, numerical simulation is necessary.

6.3.1 The Transfer Matrix Method

The calculations are performed using the transfer matrix method [119], which is explained in detail as follows. First, consider a stack of three different materials with varying refractive indices as shown in Fig. 6.9. Light travels from the material with refractive index n_1 to the material with index n_3 (top to bottom). At each interface, some of the light may be reflected due to the refractive index difference. Moreover, light may be reflected multiple times in the middle layer before getting into the other layers. Therefore, if ray-tracing technique is used, infinite series of reflected rays need to be considered for interference in the calculation of reflectance or transmittance. Although it is straight forward to consider the infinite series mathematically, the calculation becomes quite complicated for multi-layer coating where multiple infinite series exist. It is even more problematic to imagine the infinite series of reflected rays can interfere over a distance infinitely long. If one thinks about the cause of interference, it simply comes from the sum of different electro-magnetic (EM) waves of the same frequency and different phase separations provide the power intensity oscillation.

Therefore, if one can find EM wave solutions in the corresponding media, the reflectance and transmittance can be easily calculated.

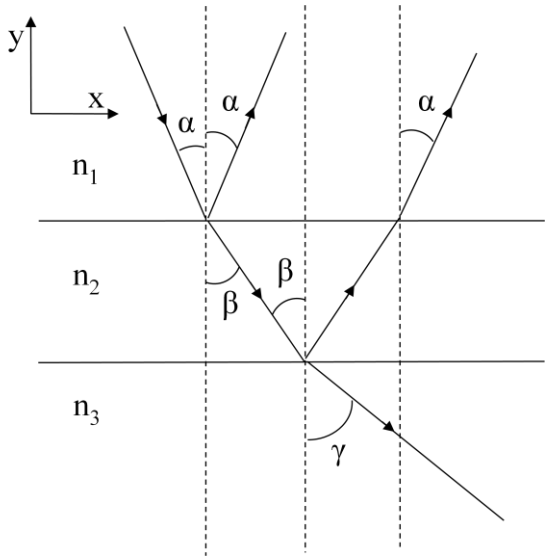

Fig. 6.9. Light incident on a stack of flat media.

The following derivation is based on plane waves and flat interfaces. Although plane waves are not physical they can be used to represent light rays or construct other solution forms. As shown in Fig. 6.9, it is easy to define the solutions in three different regions with different refractive indexes. Moreover, the solution in each region can be divided into two parts, namely down-going and up-going parts. Therefore, the TE polarized electric wave solution in the top region can be expressed as

$$\vec{E}_{1d} = \hat{z}\exp(-ik_{1y}y + ik_{1x}x) \quad , \tag{6.20}$$

$$\vec{E}_{1u} = \hat{z}r\exp(ik_{1y}y + ik_{1x}x) \quad , \tag{6.21}$$

where $\vec{E}_{1d}$ and $\vec{E}_{1u}$ represent the down-going and up-going part, respectively. r is the reflection coefficient. $\hat{z}$ is the unit vector in the z direction. k_{1y} and k_{1x} are the vertical and horizontal projections of the wave vector. The electric wave solution for the middle region can be expressed as

$$\vec{E}_{2d} = \hat{z}A_2 \exp\left[-ik_{2y}\left(y+d\right)+ik_{2x}x\right] \ , \tag{6.22}$$

$$\vec{E}_{2u} = \hat{z}B_2 \exp\left[ik_{2y}\left(y+d\right)+ik_{2x}x\right] \ , \tag{6.23}$$

where $\vec{E}_{2d}$ and $\vec{E}_{2u}$ represent the down-going and up-going part, respectively. A_2 and B_2 are the corresponding amplitude. k_{2y} and k_{2x} are the vertical and horizontal projection of the wave vector, respectively. d is the thickness of the middle layer. The electric field in the bottom layer can be expressed as

$$\vec{E}_{3d} = \hat{z}A_3 \exp\left[-ik_{3y}\left(y+d\right)+ik_{3x}x\right] \ , \tag{6.24}$$

where $\vec{E}_{3d}$ represents the down-going part, A_3 is the amplitude, and k_{3y} and k_{3x} are the vertical and horizontal projection of the wave vector, respectively. In the last region, there is no up-going part of the electric wave.

The magnetic field strength in each region can be calculated as

$$\vec{H} = \frac{1}{i\omega\mu}\nabla\times\vec{E} \ , \tag{6.25}$$

where ω is the angular frequency, μ is the permeability. Moreover, in the case when the electric field only has the z component, Eq. 6.25 can be expressed as

$$\vec{H} = \hat{x}\frac{1}{i\omega\mu}\frac{\partial E_z}{\partial y} \ , \tag{6.26}$$

where E_z is the z component of the electric field. At the interface of adjacent regions, the tangential electric and magnetic field strength are continuous. Therefore, for the first interface (between material n_1 and n_2) one has

$$1+r = A_2 \exp\left[-ik_{2y}d + i\left(k_{2x}-k_{1x}\right)x\right] + B_2 \exp\left[ik_{2y}d + i\left(k_{2x}-k_{1x}\right)x\right] \quad . \tag{6.27}$$

$$-1+r = -\frac{\mu_1}{\mu_2}\frac{k_{2y}}{k_{1y}} A_2 \exp\left[-ik_{2y}d + i\left(k_{2x}-k_{1x}\right)x\right] + \frac{\mu_1}{\mu_2}\frac{k_{2y}}{k_{1y}} B_2 \exp\left[ik_{2y}d + i\left(k_{2x}-k_{1x}\right)x\right] \quad . \tag{6.28}$$

In order to achieve non-trivial solutions to Eq. 6.27 and 6.28, k_{1x} has to be equal to k_{2x}. Therefore, Eq. 6.27 and 6.28 can be further reduced to

$$1+r = A_2 \exp\left(-ik_{2y}d\right) + B_2 \exp\left(ik_{2y}d\right) \quad . \tag{6.29}$$

$$-1+r = -\frac{\mu_1}{\mu_2}\frac{k_{2y}}{k_{1y}} A_2 \exp\left(-ik_{2y}d\right) + \frac{\mu_1}{\mu_2}\frac{k_{2y}}{k_{1y}} B_2 \exp\left(ik_{2y}d\right) \quad . \tag{6.30}$$

For the second interface (between material n_2 and n_3) one has

$$A_2 \exp\left(-2ik_{2y}d\right) + B_2 \exp\left(2ik_{2y}d\right) = A_3 \exp\left(-2ik_{3y}d\right) \quad . \tag{6.31}$$

$$-A_2 \exp\left(-2ik_{2y}d\right) + B_2 \exp\left(2ik_{2y}d\right) = \frac{-\mu_2 k_{3y}}{\mu_3 k_{2y}} A_3 \exp\left(-2ik_{3y}d\right) \quad . \tag{6.32}$$

In deriving Eq. 6.31 and 6.32, k_{2x} also needs to be equal to k_{3x}. Equation 6.29 to 6.32 can be expressed in a matrix form as

$$\begin{pmatrix}1\\ r\end{pmatrix}=\frac{1}{2}\begin{pmatrix}\exp\left(-ik_{2y}d\right)\left(1+\dfrac{\mu_1}{\mu_2}\dfrac{k_{2y}}{k_{1y}}\right) & \exp\left(ik_{2y}d\right)\left(1-\dfrac{\mu_1}{\mu_2}\dfrac{k_{2y}}{k_{1y}}\right)\\ \exp\left(-ik_{2y}d\right)\left(1-\dfrac{\mu_1}{\mu_2}\dfrac{k_{2y}}{k_{1y}}\right) & \exp\left(ik_{2y}d\right)\left(1+\dfrac{\mu_1}{\mu_2}\dfrac{k_{2y}}{k_{1y}}\right)\end{pmatrix}\begin{pmatrix}A_2\\ B_2\end{pmatrix}=\overline{\overline{B}}_{12}\begin{pmatrix}A_2\\ B_2\end{pmatrix}$$

.

(6.33)

$$\begin{pmatrix}A_2\\ B_2\end{pmatrix}=\frac{1}{2}\begin{pmatrix}\exp\left[2i\left(k_{2y}-k_{3y}\right)d\right]\left(1+\dfrac{\mu_2 k_{3y}}{\mu_3 k_{2y}}\right) & 0\\ \exp\left[-2i\left(k_{2y}+k_{3y}\right)d\right]\left(1-\dfrac{\mu_2 k_{3y}}{\mu_3 k_{2y}}\right) & 0\end{pmatrix}\begin{pmatrix}A_3\\ 0\end{pmatrix}=\overline{\overline{B}}_{23}\begin{pmatrix}A_3\\ 0\end{pmatrix} \quad .(6.34)$$

The wave vectors in the three regions satisfy

$$k_1=\omega n_1/c \quad , \tag{6.35}$$

$$k_{1x}=k_{2x}=k_{3x}=k_1\sin\alpha \quad , \tag{6.36}$$

$$\left(k_{1x}^2+k_{1y}^2\right)/n_1=\left(k_{2x}^2+k_{2y}^2\right)/n_2=\left(k_{3x}^2+k_{3y}^2\right)/n_3=\omega^2/c^2 \quad , \tag{6.37}$$

where c is the speed of light in vacuum. Moreover, Eq. 6.33 and 6.34 can be combined to give,

$$\begin{pmatrix}1\\ r\end{pmatrix}=\overline{\overline{B}}_{12}\overline{\overline{B}}_{23}\begin{pmatrix}A_3\\ 0\end{pmatrix}=\begin{pmatrix}b_{11} & b_{12}\\ b_{21} & b_{22}\end{pmatrix}\begin{pmatrix}A_3\\ 0\end{pmatrix} \quad . \tag{6.38}$$

The matrices $\overline{\overline{B}}_{12}$ and $\overline{\overline{B}}_{23}$ only depend on the refractive index, incident angle and angular frequency of the light beam.

The energy flux density of the EM wave can be expressed as

$$S=\sqrt{\frac{\varepsilon}{\mu}}\left|\mathrm{Re}(E)\right|^2 \quad , \tag{6.39}$$

Therefore, the reflectance in the top layer is

$$r^2 = b_{21} / b_{11} \quad , \tag{6.40}$$

The above derivation is for TE polarized light; while the results for TM polarized light can be obtained by the duality principle as

$$\vec{E} \longrightarrow \vec{H} \, , \; \vec{H} \longrightarrow -\vec{E} \, , \; \mu \longrightarrow \varepsilon \, , \; \varepsilon \longrightarrow \mu \quad . \tag{6.41}$$

From the above introduction of the transfer matrix method, it can be seen that although this method is derived for single layer coating it can be easily applied to multi-layer coating by inserting more matrices. It should be noted that the above derivation is based on plane waves and is only suitable for flat surface coating. Therefore, the hemisphere surface is approximated by many small flat areas in the calculation. A careful normalization procedure is needed to average the light extraction from all the flat area elements.

6.3.2 Results and Discussion

In the calculations, single layer anti-reflection coatings are chosen using the materials SiO_2, Al_2O_3 and ZnO with refractive indices 1.54, 1.76 and 1.92, respectively [100, 120]. The refractive indices are assumed to be constant in energy due to the narrow spectral width of the quantum well emission. The ratio of the active region radius to the hemisphere radius is defined as a dimensionless radius, r_0/R, that is varied from 0.10 to 0.30. For a given dimensionless radius and anti-reflection coating material, the coating thickness is optimized to minimize the reflectance at the hemisphere-air interface over the entire emission spectrum.

The results are shown in Fig. 6.10, where the reflectance loss increases dramatically when the dimensionless radius exceeds 0.25, which is the ratio where the onset of total internal reflection occurs as some of the emitted light now lies outside of the escape cone. Moreover, ZnO provides the lowest reflectance among the three materials studied due to its higher refractive index. For large hemispheres with a small dimensionless radius (<0.15) and proper ZnO anti-reflection coating, the reflectance loss is less than 0.1%, which is negligible compared to the other losses in the device; in which case the hemisphere is essentially a perfect extractor.

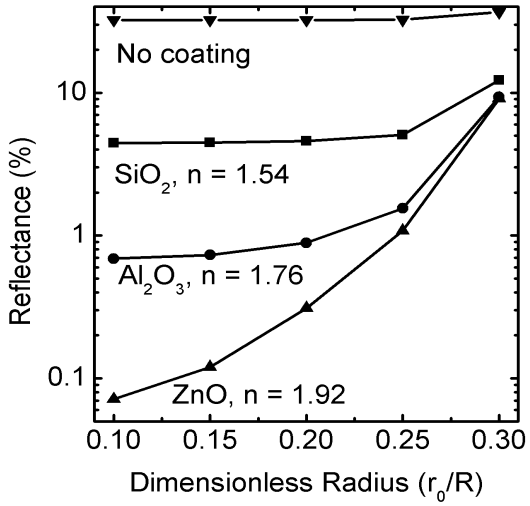

Fig. 6.10. Reflectance of the GaAs hemisphere with different anti-reflection coatings and dimensionless radius.

The extraction efficiency for the entire LED structure can be written as

$$\eta_e = \frac{\text{Extraction Factor}}{\text{Extraction Factor} + \text{Loss Factor}} = \frac{1 - \text{Loss Factor} - \text{Recycling Factor}}{1 - \text{Recycling Factor}} \quad , \tag{6.42}$$

where the extraction factor is the fraction of the active region spontaneous emission that is extracted from the spherical surface of the hemisphere, the loss factor is the fraction of the spontaneous emission lost to internal parasitic absorption plus the fraction extracted from the flat surface of the hemisphere, and the recycling factor is the fraction of the spontaneous emission that is absorbed in the active region, which is not a loss from the standpoint of extraction efficiency as the photon energy is recycled.

Next the extraction factor and the extraction efficiency are determined by estimating the loss factor and recycling factor. Free carrier absorption, which typically has an absorption coefficient less than 50 cm^{-1} results in a parasitic loss that is less than 1% [121]. The parasitic losses caused by free carrier absorption are greatly reduced in this device design because the hemisphere effectively eliminates trapped light; a substantial improvement over a planar design where light trapping results in multiple passes through the device regions containing free carriers before extraction occurs.

However, absorption in metal contacts adjacent to the active region can result in even larger parasitic losses than those for free carriers; particularly when the contact covers a significant portion of the active region. For example, the typical contact materials for GaAs consist of Ti/Pt/Au metal layers about 20/20/200 nm thick; with a complex index of refraction coefficient of $3.03 + 3.65i$

at 980 nm [100], about 72% of the incident light is absorbed by the Ti metal layer. In designing the size of a contact there is a tradeoff between how well the current is spread (larger is better) and the absorption losses (smaller is better). In experiment, 10 μm wide metal rings are used as contacts due to equipment limitations and covers 44% of the active region. This contact design is named as Design I. In Design I the contact offers good current spreading at the expense of large contact area and absorption loss. This loss is about 16% ($0.72 \times 0.44 \times 1/2$); note that only one half of the spontaneous emission is incident on the contact side, hence the ½ factor. In the limit of no contact coverage, the contact absorption loss would be zero and this design is named as Design II for comparison.

For the remaining 56% (or 100%) of the active region not covered by contacts, a small amount of the incident light is extracted from the flat side of the hemisphere through the escape cone containing about 4% of the spontaneous emission, of which 31% is reflected back; resulting in a loss that is less than 1% ($0.56 \times 0.04 \times 0.69 \times 1/2$) for Design I and about 1% ($1 \times 0.04 \times 0.69 \times 1/2$) for Design II. The above discussed three losses add up to a loss factor about 18% for Design I and 2% for Design II. Moreover, on the hemisphere side, the back reflection loss due to a less than ideal anti-reflection coating on the hemisphere surface varies with different coating material and dimensionless radius. The reflected light is assumed to be parasitically lost inside the hemispherical device resulting in an extra loss factor from 0.1% to 9% for ZnO coating and 32% to 37% for un-coated hemisphere surface. Therefore, for Design I the total loss factor

ranges from 18% to 27% in a ZnO coated device and 50% to 55% in un-coated device. For Design II, the total loss factor ranges from 2% to 11% in a ZnO coated device and 34% to 39% in un-coated device.

The photon recycling factor (fraction of spontaneous emission absorbed in the quantum wells) is approximately 4%, using an absorption coefficient of 13440 cm^{-1} for InGaAs [100]. Subtracting both the loss and recycling factors, one can calculate the fraction of spontaneous emission extracted from the hemisphere and the extraction efficiency from Eq. 6.42. Note that both the loss and recycling factors are greatly reduced in this device via the elimination of light trapping. The calculation results of the extraction factor for the device with ZnO coating and without coating are shown in Fig. 6.11 and Fig. 6.12 shows the extraction efficiency. It can be seen that through reducing the contact coverage from 44% to 0%, both the extraction factor and extraction efficiency increase by more than 10%. Moreover, good anti-reflection coating also increases both the extraction factor and extraction efficiency by 20% to 32% depending on the dimensionless radius.

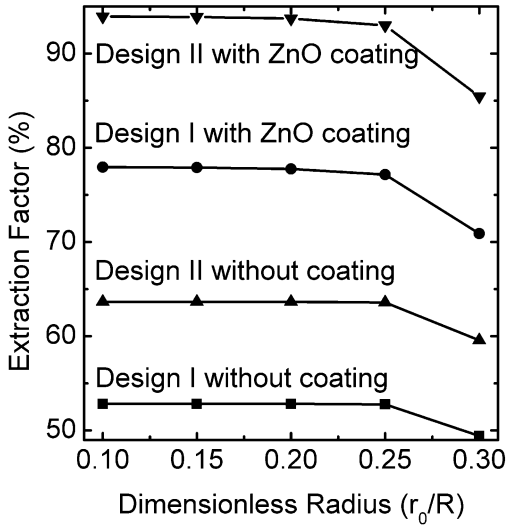

Fig. 6.11. Extraction factor versus dimensionless radius for Design I and II with ZnO coating and without coating.

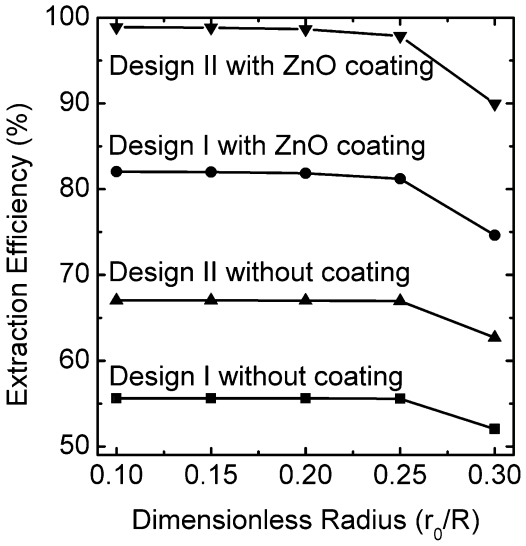

Fig. 6.12. Extraction efficiency versus dimensionless radius for Design I and II with ZnO coating and without coating.

6.4 Discussion

An InGaAs/GaAs quantum well thin slab LED monolithically integrated with a GaAs hemisphere is proposed for semiconductor luminescence refrigeration. From section 6.2, the thin slab LED achieves over 100% energy conversion efficiency and over 96% spontaneous emission quantum efficiency at 150 K under optimum injection level (quasi Fermi level separation equal to energy bandgap) for both single and triple quantum well structures. However, the greater than unity energy conversion efficiency is based on 100% luminescence extraction. From section 6.3, the extraction factor and extraction efficiency for

Design I (44% metal contact coverage) and Design II (0% metal contact coverage) are calculated. Therefore, the more accurate energy conversion efficiency, considering the various loss mechanisms, for Design I and II can be calculated by multiplying the energy conversion efficiency from section 6.2 and the extraction factor from section 6.3. Figure 6.13 shows the energy conversion efficiency versus dimensionless radius for Design I and II (triple quantum well structure is used) at, (a) 150 K, and (b) 300 K. In later experiments, a device using Design I, triple quantum well structure, no anti-reflection coating, and 0.33 dimensionless radius is processed and tested. It can be seen that the processed device can theoretically achieve about 50% and 40% energy conversion efficiency at 150 K and 300 K, respectively. Good anti-reflection coating can further increase the energy conversion efficiency by about 20%.

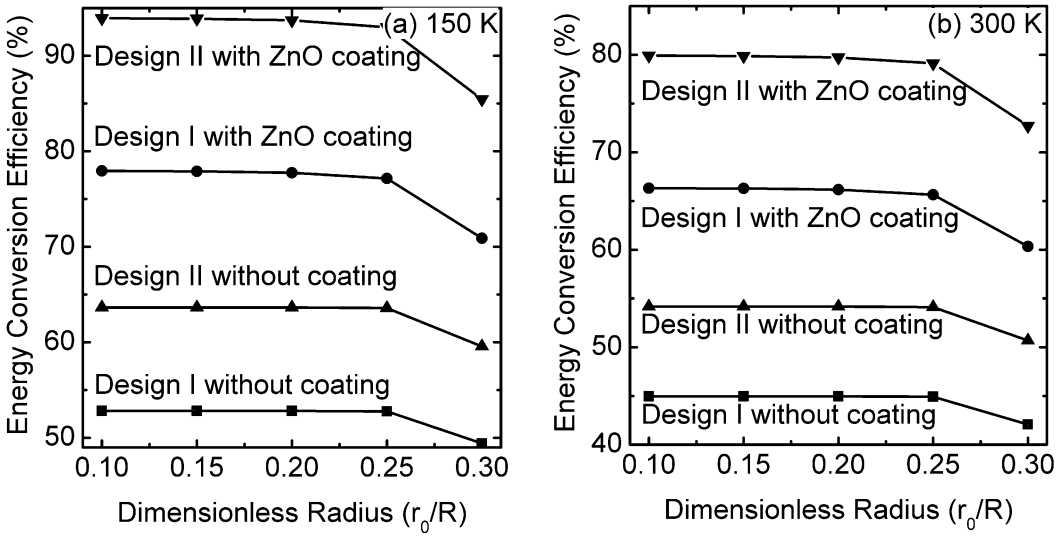

Fig. 6.13. Energy conversion efficiency versus dimensionless radius for Design I and II (triple quantum well structure is used) at, (a) 150 K, and (b) 300 K.

Moreover, the internal quantum efficiency of the entire device can be calculated using [122]

$$\eta_i = \frac{(1-\gamma_r)\eta_q}{1-\gamma_r\eta_q} \quad , \tag{6.43}$$

where η_q is the spontaneous emission quantum efficiency and γ_r is the photon recycling factor. Due to the small recycling factor (4%), the internal quantum efficiency and the spontaneous emission quantum efficiency are very close. The internal quantum efficiency at 150 K and 300 K are 96% and 79%, respectively. It should be noted that the leakage current lowers the internal quantum efficiency in electrically injected devices and should be included in the calculation. However, it is omitted here because the leakage current approaches zero below optimum injection levels as shown in Fig. 6.7.

VII. EXPERIMETAL STUDY OF SEMICONDUCTOR LUMINESCENCE REFIRGERATION DEVICE

In this chapter, the experimental study of semiconductor luminescence refrigeration device is presented. The device layer structure design is discussed followed by the discussion of device processing. The critical processing steps, such as photoresist reflow and dry etch, are simulated to insure successful processing. Finally, optical testing on the devices is carried out and the results are discussed.

7.1 Device Layer Structure Design

The semiconductor luminescence refrigeration device is grown by molecular beam epitaxy (MBE) using a VG V80H solid source MBE system. The material growth cross section is shown in Fig. 6.3 and is also shown here as Fig. 7.1 for completeness. The growth direction is from left to right and the function for each layer is explained as follows.

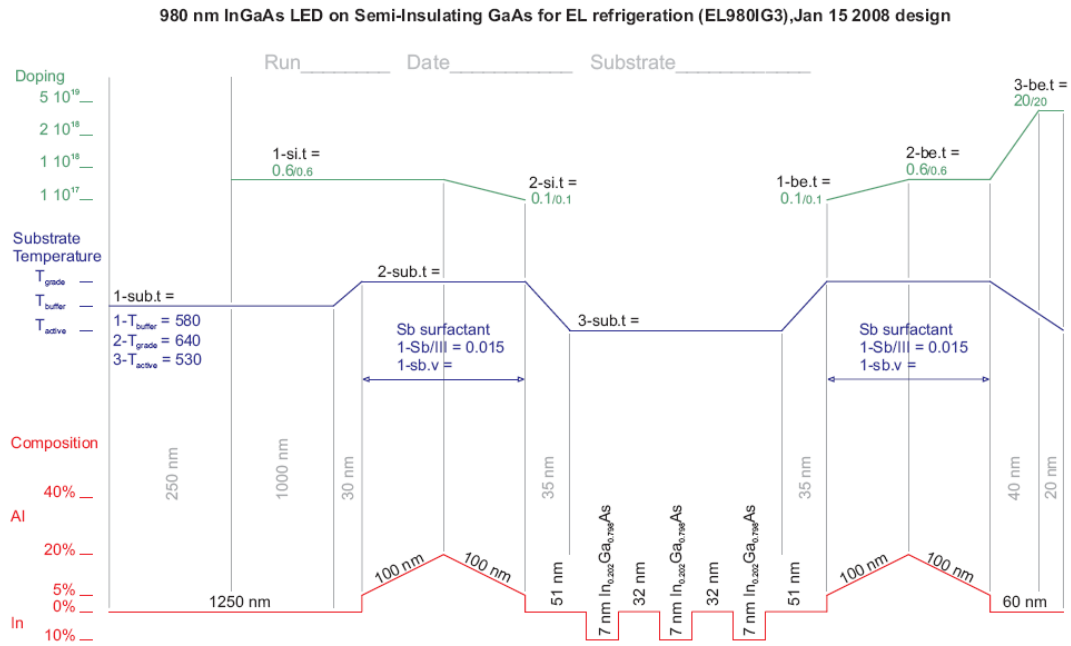

Fig. 7.1. Cooling device growth cross section.

The substrate used in this growth is a semi-insulating GaAs substrate, which helps minimize the free carrier absorption of photons emitted from the active region. Then, a 250 nm GaAs buffer layer is grown to ensure a smooth surface for the actual epitaxial growth after de-oxidation. This is followed by the growth of 1030 nm GaAs with n-type doping of 6×10^{17} cm^{-3}. In the later device processing, n-contact will be made on this layer after mesa etching. The reason of growing such a thick layer is to provide enough tolerance for etching depth variations. Then, a 200 nm AlGaAs barrier layer is grown to confine carriers. In this layer, the Al mole fraction is graded with the peak mole fraction in the middle. This Al composition graded barrier layer not only confines carriers but also improves the carrier injection efficiency with a gradual potential change. The

active region consists of three $In_{0.202}Ga_{0.798}As$/GaAs strained quantum-wells (QWs) with peak emission wavelength at 980 nm. Figure 7.2 shows the room temperature photo luminescence (PL) spectrum of the sample. This emission energy is well below the bandgap of GaAs and therefore the absorption by the substrate is quite low. The number of QWs is a trade-off between cooling power and cooling efficiency. On one hand, more QWs can provide more cooling power per device; on the other hand, more QWs can bring injection unevenness which lowers the energy conversion efficiency. An over biased QW can only provide heat rather than cooling power, while an under biased QW cannot work at its full potential. Therefore, devices with more wells are not necessarily to perform better due to the injection non-uniformity. The active region is undoped to minimize the material defects. After the growth of the active region another AlGaAs carrier confinement layer is grown followed by a highly p-doped layer of 60 nm GaAs for p-contact. Moreover, Sb surfactant is used during the AlGaAs growth to improve the material quality [33].

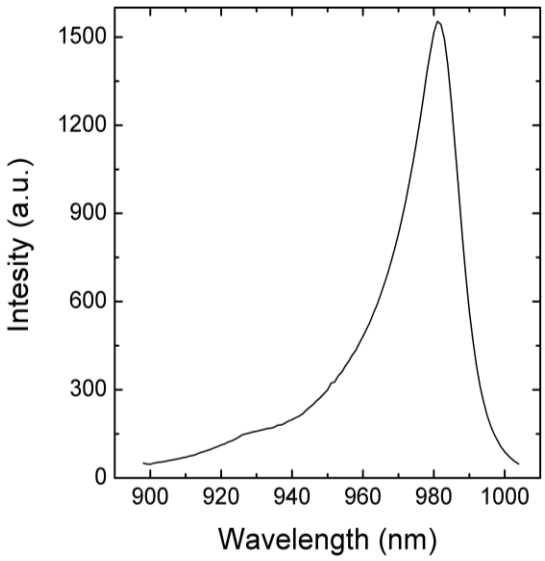

Fig. 7.2. Room temperature photo luminescence (PL) spectrum.

7.2 GaAs Hemisphere Processing Simulation

The proposed device consists of a GaAs hemisphere with a thin slab LED on the top. While a thin slab LED can be fabricated using conventional procedures, the fabrication of a perfect semiconductor hemisphere is quite challenging. However, the fabrication of micro lenses, which is similar to the fabrication of micro hemispheres, has been investigated extensively. Traditionally, micro lenses can be divided into two groups: polymer or glass based, and semiconductor based. For polymer based micro lenses, reflow, hot/UV embossing, gray scale lithography, microjet, excimer laser ablation and direct laser write techniques can be used [123-129]. Although high aspect ratio lenses are achievable, the refractive indexes usually cannot match with that of the light emitting material. For semiconductor based micro lenses, focused ion beam and pattern transfer from photoresist to semiconductor by wet or dry etch are usually

used [130-138]. The refractive indexes are favorable but only low aspect ratio micro lenses are usually produced by this technique with potentially low throughput.

Although GaAs hemispheres have been attempted [139], no design rules or detailed processing information were published and the large volume production capability was unclear. With the new dry etch technology, namely inductive coupled plasma (ICP) dry etch, it is possible to fabricate close to perfect semiconductor micro hemispheres. In this study, the proposed device is fabricated by firstly reflowing the photoresist pattern to form a dome shaped mask and then using ICP dry etch to transfer the curved pattern to the GaAs substrate to form a hemisphere. In order to get a perfect hemisphere, simulations are done to predict the processing results of potoresist reflow and ICP dry etch. Feedbacks are taken from scanning electron microscopy (SEM) and profilometer measurements.

7.2.1 Photoresist Reflow Simulation

In order to fabricate a curved semiconductor surface, a curved photoresist mesa is required as the necessary mask. This is achieved by firstly defining a cylinder of photoresist by conventional photolithography, then heating it up and letting it reflow to take a curved shape. The shape of the curved photoresist mesa after reflow is governed by the Young-Laplace equation, shown in Eq. 7.1, assuming the photoresist is a liquid droplet at steady state

$$\Delta p = \sigma\left(\frac{1}{R_1} + \frac{1}{R_2}\right) \quad , \tag{7.1}$$

where Δp is the pressure difference over the photoresist-air interface; R_1 and R_2 are the principal radii of curvature at the interface; and σ is the surface tension coefficient of the droplet.

A schematic diagram of the photoresist droplet is shown in Fig. 7.3. Based on Eq. 7.1, the equation for a point at position (r_d, z) on the droplet can be written as

$$K(r_d) = K_0 + \frac{\rho g}{\sigma}[\delta - z(r_d)] \quad , \tag{7.2}$$

where

$$K(r_d) = -\left\{ \frac{\dfrac{d^2 z}{dr_d^{\,2}}}{\left[1+\left(\dfrac{dz}{dr_d}\right)^2\right]^{1.5}} + \frac{\dfrac{dz}{dr_d}}{r_d\left[1+\left(\dfrac{dz}{dr_d}\right)^2\right]^{0.5}} \right\} \quad , \tag{7.3}$$

is the position dependent curvature of the free surface of the droplet [140]; $R_0 = 2/K_0$ is the radius of surface curvature at the apex; r_d is the radial distance; z is the height; δ is the droplet height at the apex; ρ=1.08 g/cm^3 is photoresist density [141]; g is acceleration of gravity. In Eq. 7.2, the second term is at least two orders of magnitude smaller than the first, since surface tension coefficient normally ranges from 0.01 to 0.4 N/m^2 and the droplet radius is around 100 μm [142]. Therefore, the accuracy of surface tension coefficient is not important and that of water (0.1 N/m^2) is used in the calculation. Define $dz/dr_d = y$, then Eq. 7.2 is converted to

$$\begin{cases} dz/dr_d = y \\ dy/dr_d = -(1+y^2)^{1.5} \cdot \left[K_0 + \dfrac{\rho g}{\sigma}(\delta - z) \right] - \dfrac{y(1+y^2)}{r_d} \end{cases} . \tag{7.4}$$

When $r_d = 0$, one has $z = \delta$, $y = 0$ and $K = K_0$.

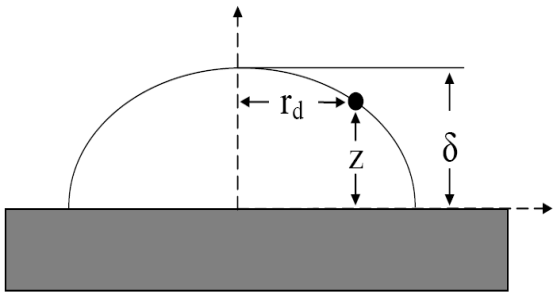

Fig. 7.3. Schematic diagram of the photoresist droplet on a flat surface.

Equation 7.2 can be solved using the fourth-order Runge-Kutta method with any two initial inputs out of dome height δ, apex curvature K_0, and radial distance r_d [143]. In the calculation, the dome height δ and curvature K_0 are used as the only inputs. Then these two values are systematically varied to simultaneously match both the initial photoresist volume (assuming 20% volume loss determined from profilometer measurement) and photoresist cylinder radius (no change in radius from profilometer measurement), determined by the photoresist spin coating and photolithography recipes. The final calculated photoresist droplet profile (dashed line) together with the measured one (solid line) is shown in Fig 7.4. The nonsymmetrical measured photoresist profile is due

to the artifacts of the mechanical profilometer measurement.

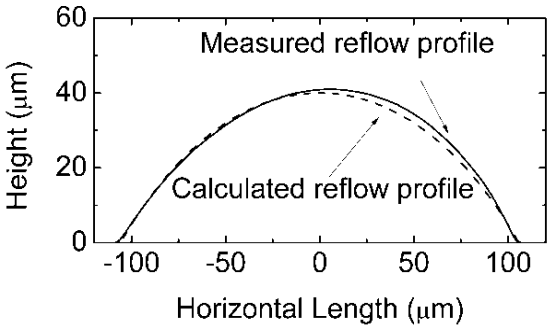

Fig. 7.4. Calculated (dashed curve) and measured (solid curve) photoresist droplet profile after reflow.

7.2.2 ICP Dry Etch Simulation

To achieve the final GaAs hemisphere, ICP dry etch process is performed after the photoresist reflow and the reflow simulation results is directly used as input for the dry etch simulation to predict the etching result. In this dry etch process, both the vertical and horizontal etch rate can be tuned. Therefore, the dry etch calibration results are also important inputs for the dry etch simulation besides the photoresist droplet profile. From experiments, the vertical etching selectivity of photoresist to GaAs is about 1:2.3 and the lateral etch rate is roughly one tenth of the corresponding vertical etch rate. Figure 7.5 shows the calculated GaAs dome (non-perfect hemisphere) profile after etch and the measured one by profilometer. Figure 7.6 shows the SEM image of a trial-etching dome and etching simulation result (white curve), showing the close fit between experiment

and calculations. From Fig. 7.5, although the slope at the foot of the etched dome is not infinite, the etched dome is still very close to a perfect hemisphere for the most part. Moreover, one more simulation is performed that starts from a perfect GaAs hemisphere and goes all the way back to the required photoresist droplet profile. Figure 7.7 shows the required photoresist profiles (solid curves) for perfect GaAs hemispheres and the achievable photoresist droplet profiles (dashed curves) at various radii. It is confirmed again that the measured photoresist droplet profile is very close to the one required for a perfect hemisphere except for the edges and as the radius gets smaller the measured and required profiles become closer.

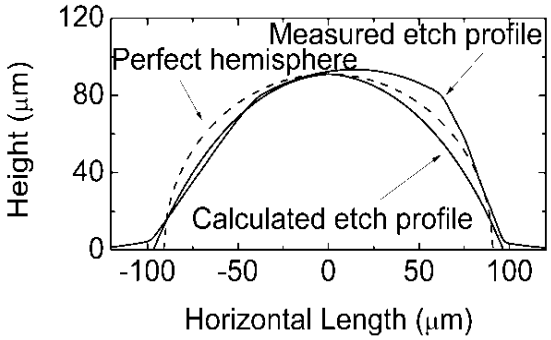

Fig. 7.5. Calculated and measured GaAs hemisphere etch results compared a perfect (dashed curve) hemisphere.

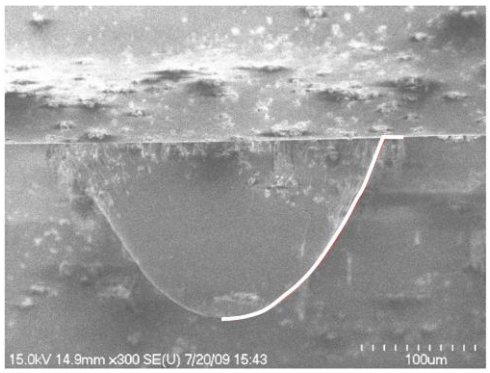

Fig. 7.6. SEM image of a trial-etching dome and etching simulation result (white curve).

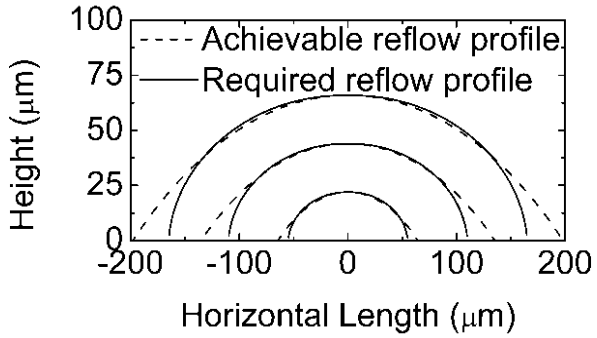

Fig. 7.7. Required photoresist profiles (solid curves) for perfect GaAs hemispheres and achievable photoresist droplet profiles (dashed curves) at various radii.

7.3 Device Processing

The device processing can be divided into two major parts: i) thin slab LED processing, and ii) GaAs hemisphere processing. The samples are double side polished three-inch GaAs wafers with epitaxial layer on the top and the side with the epitaxial layer is referred as the front (top) side in later discussions.

7.3.1 Thin Slab LED Processing

The processing of thin slab LED involves six times photolithography and three times metal deposition. The first step is to define a mesa with 30 μm radius in the epitaxial layer (front side). In this step, a photoresist mesa is firstly defined by spin coating of the photoresist AZ3312 followed by photolithography. This mesa serves as the mask for the subsequent wet etch. In the wet etch step, an acid solution made of H_2SO_4, H_2O_2, and H2O with volume ratio 1:8:40 is used. This particular solution features a moderate etch rate for GaAs at about 1 μm/min at

room temperature. The desired etch depth is between 650 nm and 850 nm. The finished GaAs mesa is schematically shown in Fig 7.8. The reason for the mesa etching is to isolate the devices and also expose the n-type layer previously buried at the bottom of the epitaxial layer. Then both the p-type (top of the mesa) and n-type (bottom of the mesa) layers can be seen from the top and can be used for contacts layers in later steps.

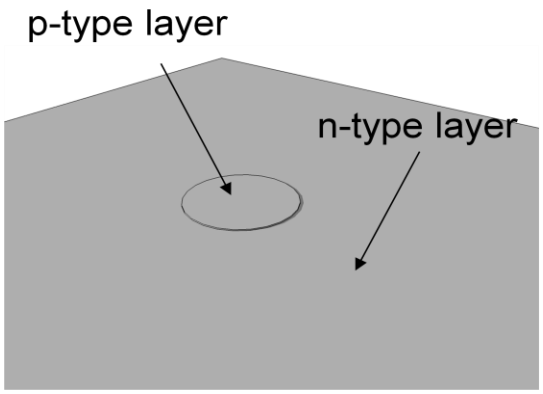

Fig. 7.8. GaAs mesa formation by wet etch.

The second step is p-metal deposition by e-beam evaporator. In this step, the imaged reversed photoresist AZ5214 is firstly spin coated across the sample. Then a ring with inner diameter of 15 μm and outer diameter of 25 μm is opened on top of the mesa by photolithography. Next, the sample is dipped into a solution of $NH_4OH:H_2O$ with 1:10 volume ratio for 30 sec to remove the native oxide on the exposed mesa surface. The sample is then immediately put into the e-beam deposition chamber. The idea of e-beam deposition is to use electron beam to heat the metal and metal atoms can fly out from the crucible to the

sample surface due to increased kinetic energy. This technique features good directionality and low side wall coverage, which is quite desirable for subsequent lift-off process. The p-metal deposition is composed of Ti/Pt/Au with thicknesses 20/20/200 nm, respectively. The Ti layer is used to achieve better adhesion and the Pt layer is used to prevent Ga from diffusion into the Au layer [144]. Au is used to reduce the contact metal resistance. Typically, the p ohmic contact is fairly easy to achieve due to the high doping levels achievable during growth. After the deposition, the sample is put into acetone to lift off the metal on top of the photoresist and a metal ring is then left on the top of the GaAs mesa. This step is called lift-off. A clean surface before processing is the key to achieve good lift-off results.

The third step is n-metal deposition by e-beam evaporator following almost the same procedure as p-metal deposition. The only difference is that the n-type contact is composed of Ni/AuGe/Ni/Au with thicknesses 15/133/175/200 nm, respectively. In this contact design, Ni is used as a wetting agent to improve the adhesion of the AuGe layer; Ge in the AuGe layer is used for doping the GaAs during alloying [97, 144]. The AuGe layer is applied in proportions that represent a eutectic alloy (88% Au, 12% Ge by weight) [97]. After cleaning, the sample is annealed at 400 ℃ for 1 min in N_2/H_2 forming gas. A specific contact resistance in the range of 10^{-6} $\Omega \cdot cm^2$ can usually be achieved for both p-contact and n-contact [97, 144]. Figure 7.9 shows a schematic drawing of the p- and n-contacts.

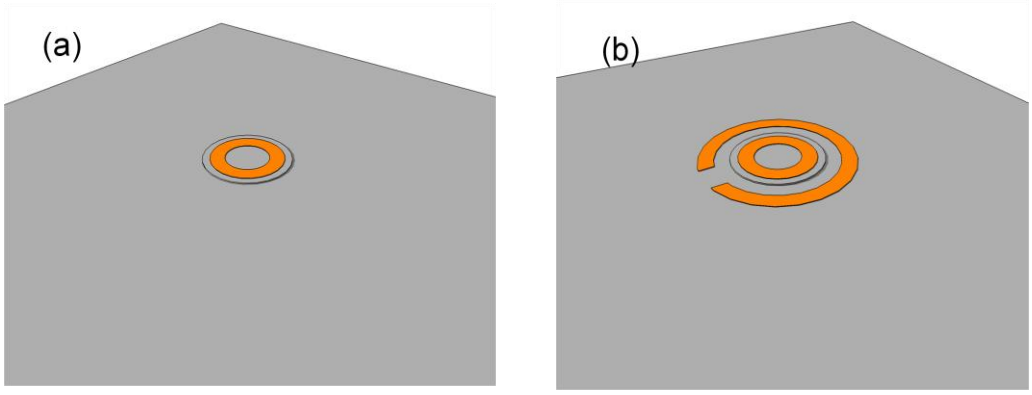

Fig. 7.9. (a) P-type contact deposition. (b) N-type contact deposition.

The forth step is polyamide passivation. In this step, a layer of 1 μm thick photoresist AP2205 is firstly deposited by spin coating. Then four windows are opened in the photoresist layer around the LED by photolithography. The photoresist on top of the metal rings is also removed at the same time. Finally, the sample is cured at 350 ℃ for 1 hour in a furnace filled with N_2 and the photoresist turns into polyamide after curing. In the curing step, it is important to use a slow temperature ramp rate to avoid possible cracks. This polyamide layer completely covers the LED surface and side walls except the metal contacts and can help reduce the surface recombination rates. This layer also provides extra mechanical strength to support the whole structure. A sample with the polyamide layer is schematically drawn in Fig. 7.10.

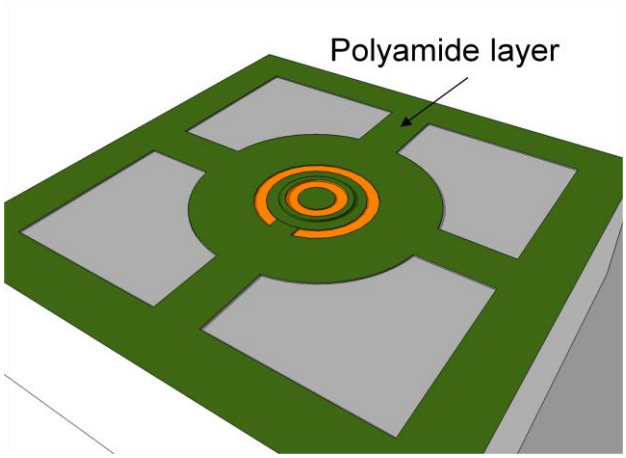

Fig. 7.10. Polyamide passivation layer deposition.

The fifth step is Au contact pad deposition. In this step, the sample front side is firstly roughened by reactive ion etch (RIE) at 50 W for 5 min with O_2. The roughened surface can provide better adhesion for the subsequent Au deposition. Then the image reversed photoresist AZ5214 is used to define the pattern of two contact pads connecting the metal rings by photolithography. Next, a 200 nm thick Au layer is deposited followed by the lift-off process. The finished device is schematically drawn in Fig. 7.11. Figure 7.12 (a) shows a photo of the device under microscope; and (b) shows a magnified image of the connecting regions between Au contact pad and metal rings. The reason for this step is because the metal rings are too narrow to be connected with probing tips. It should be noted that the Au contact pads are on top of the polyamide layer, which is an insulator.

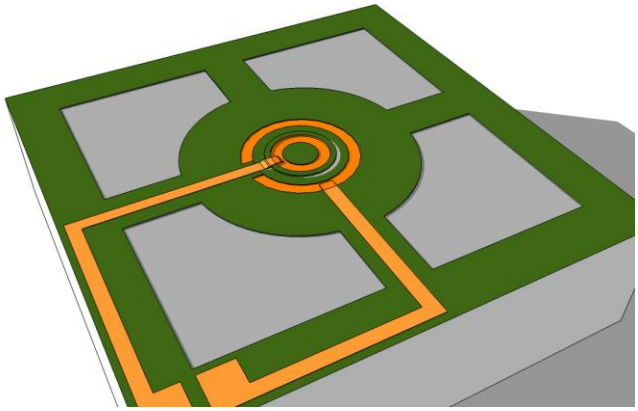

Fig. 7.11. Au contact pad deposition.

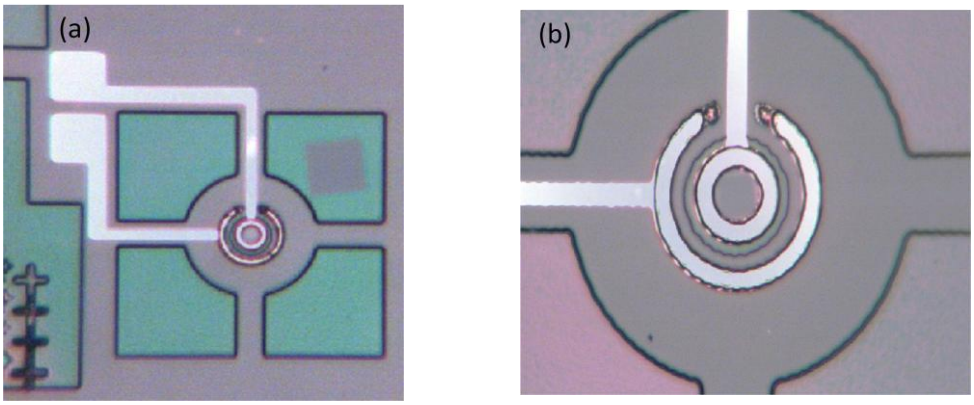

Fig. 7.12. (a) Picture of the device after Au contact pad deposition. (b) Magnified image showing the connecting regions between Au contact pad and metal rings.

The sixth step is support arm etch. In this step, a layer of 10 μm thick photoresist AZ4620 is firstly deposited by spin coating. Then four windows are opened coinciding with the windows in the polyamide layer by photolithography. Finally the four windows are etched 15 μm deep by ICP dry etch as schematically

shown in Fig. 7.13. The dry etch recipe uses a BCl_3 flow of 35 sccm, Cl_2 flow of 1 sccm, chamber pressure at 8 mTorr, platen power at 400 W, coil power at 600 W. The etch rate is calibrated to be 1.25 μm/min. After this step, the processing of the thin slab LED is finished. It should be noted that the final support arm etch step normally doesn't exist in coplanar LED processing. It is adopted here to help the processing of the back side hemisphere. The back side etch usually takes up to two hours and good calibration is difficult. If four windows are opened on the front side of 15 μm deep, one could see through the four windows from the back when the back side etch is close to finish. The remaining GaAs frame is 15 μm thick. Therefore, these four windows can serve as the detection feature to stop etching. A photo of the device looking from the back is shown in Fig. 7.14 to illustrate the idea. When the windows are etched through, four GaAs arms will support the whole structure. These four arms are 40 μm wide and 15 μm thick, which could also minimize the heat transfer. This is very important if only a small amount of cooling power is produced.

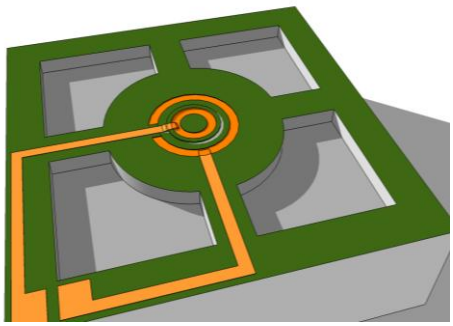

Fig. 7.13. Support arm etch.

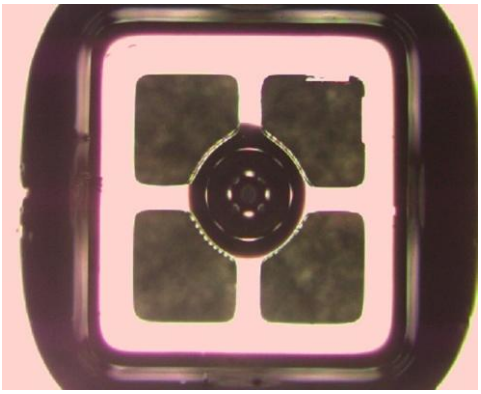

Fig. 7.14. Photo taken from the backside of the sample when etching stops.

7.3.2 GaAs Hemisphere Processing

The GaAs hemisphere processing consists of five major steps involving three times photolithography. The first step is back side lapping and polishing. Before the lapping process, photoresist AZ4620 is spin coated to the front side to protect the thin slab LED. Then the sample front side is mounted to a 4-inch glass plate using wax. In this step it is important to apply only a thin layer of wax to insure the flatness of the bounding. Any air bubbles need to be pressed out to avoid cracks during lapping. Then the glass plate is mounted on a jig with the sample back side facing the lapping plate. A slurry mix containing 9 μm Al_2O_3 particles and a grooved glass lapping plate are used for lapping. The sample is lapped down to about 125 μm from the back side.

After the lapping is finished, the sample is polished to mirror like to enable back side photolithography. The polishing chemical is Chemlox, which is

a sodium hypochlorite based polishing fluid provided by Logitech. In this step, a thin layer of oxide is formed when removing the GaAs material on the back side of the sample. It should be noted that the polishing time has to be short; otherwise small pits may form on the surface due to local chemical enrichment. The optimum polishing time is 3 min and about 10 μm of GaAs is further removed from the back side of the sample in this process. Therefore, the sample thickness after polishing is 115 μm, which is the desired thickness to process a hemisphere of 100 μm in radius. After polishing, the wax on the sample has to be cleaned using heated Ecoclear provided by Logitech. In this step, a long cleaning time is desirable because it is very difficult to tell if there is still a thin layer of wax remaining on the sample. This cleaning step is very critical to the subsequent processing, as even a tiny amount of wax can act as mask during etching.

The second step is back side alignment mark etch. This is a preparation step for the following back side alignment. The goal is to put some marks on the back side of the sample so that the hemisphere on the back side can be aligned to the front side LED. Figure 7.15 shows the schematic diagram of the process flow for this step. A 4-inch quartz wafer is used to carry the 115 μm thick sample because the quartz wafer is transparent in the visible range. The back side alignment is done with the help of two microscopes under the sample. Then alignment marks are formed by wet etch after lithography.

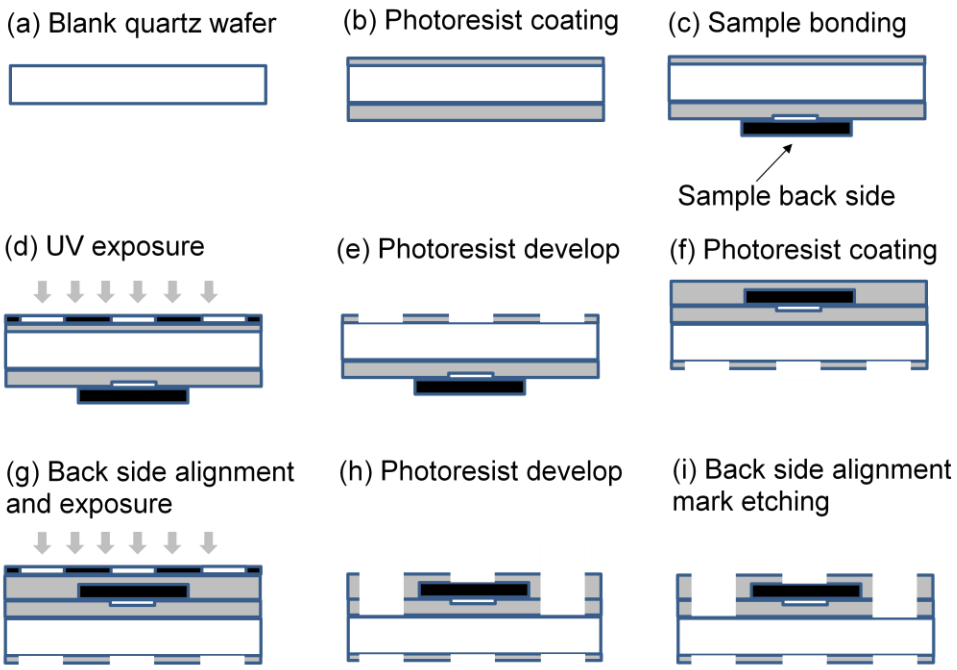

Fig. 7.15. Process flow for back side alignment mark etching.

The third step is photoresist reflow. To attain the correct hemisphere curvature and size, a layer of 27 μm thick photoresist AZ4620 is coated to the back side of the remaining substrate by multiple spin coating and it is followed by standard photolithography to form photoresist cylinders of 100 μm in radius. The photoresist cylinders are then reflowed to create curved photoresist mesas as the dry etch mask by slowly heating up the sample from 60 ℃ to 125 ℃. In this step a slow temperature ramp up rate is necessary to avoid creating any big air bubbles and a slow temperature ramp down rate is followed to avoid photoresist cracking due to strain.

The forth step is the hemisphere etch. In this step, the ICP dry etch technique is used and the etching recipe is the same as the support arm etch.

During etching, the sample front side is mounted to a ceramic plate using cooling grease and the plate is cooled by liquid helium. It is important to apply an even layer of cooling grease as the sample may be heated up locally during etching. The local heating will increase the etch rate locally. Moreover, it is also important to etch away all the photoresist, otherwise a flat top will be left on the GaAs hemisphere. Finally GaAs hemispheres of about 90 μm radius are fabricated in the remaining substrate from the back side, which are also aligned to the center of the top thin slab LEDs.

The last step is blank anti-reflection coating deposition. In this step, ZnO is preferred over SiO_2 or Si_3N_2 due to its higher refractive index at 980 nm wavelength. Moreover, it is critical to accurately control the coating thickness and an error within 5 nm is desired. However, this step is not carried out during the device processing due to the tool failure. Figure 7.16 shows schematic diagram of the finished deice (a) top side, and (b) back side. Figure 7.17 show SEM pictures of the device (a) top side, and (b) back side. Figure 7.18 shows an SEM picture of the device array. From Fig. 7.16, it can be seen that arrays of GaAs hemispheres have been made with good uniformity and the hemispheres are close to perfect indicating the capability for large volume fabrication.

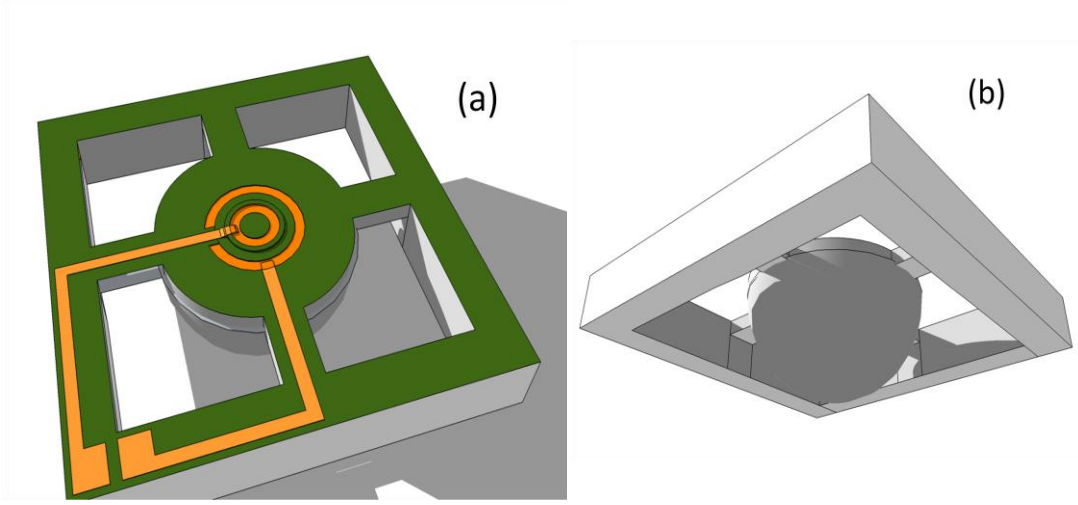

Fig. 7.16. Schematic diagram of finished deice (a) top side, and (b) back side.

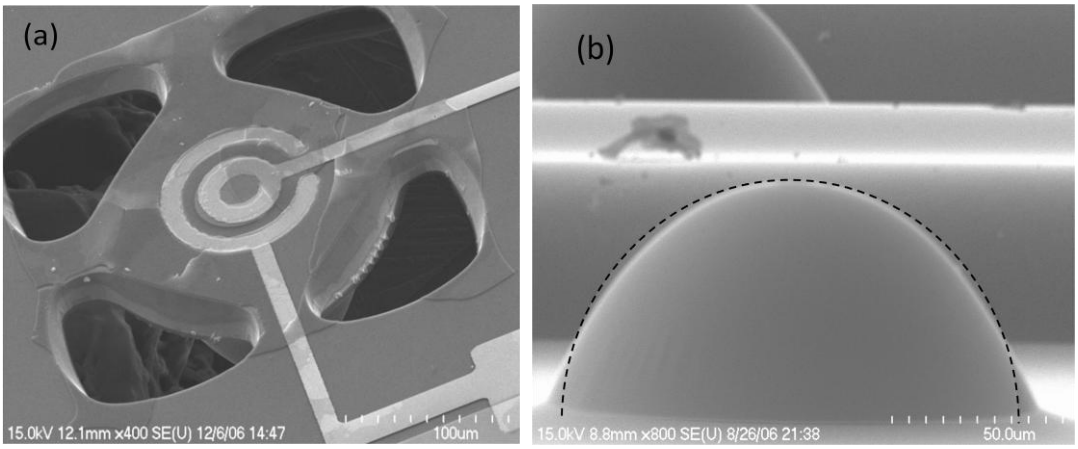

Figure 7.17. SEM pictures of the device (a) top side, and (b) back side.

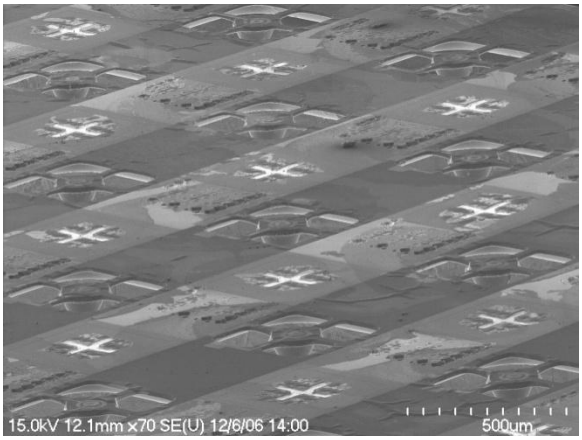

Fig. 7.18. SEM picture of the device array.

7.4 Optical Testing Setup

This section discusses the optical testing setup for the devices fabricated using the procedures described in the previous section. Although the device is intended for electrical injection testing, optical testing is used due to the possible failure in contact annealing or doping during material growth. Moreover, due to the uniqueness of the device structure and testing requirement, an optical injection testing setup is built. This setup can simultaneously measure the total emission power and the micro photo luminescence (PL) spectrum. The PL intensity gives information about device internal quantum efficiency and the red shift of peak wavelength tells the temperature increase during testing. However, in this setup the device temperature cannot be controlled by a thermal electric (TE) cooler or cryostat because the sample cannot be attached on a copper plate. This is because the injection beam and emission beam are on opposite side of the sample. Figure 7.19 shows the schematic diagram of the setup and is explained as follows.

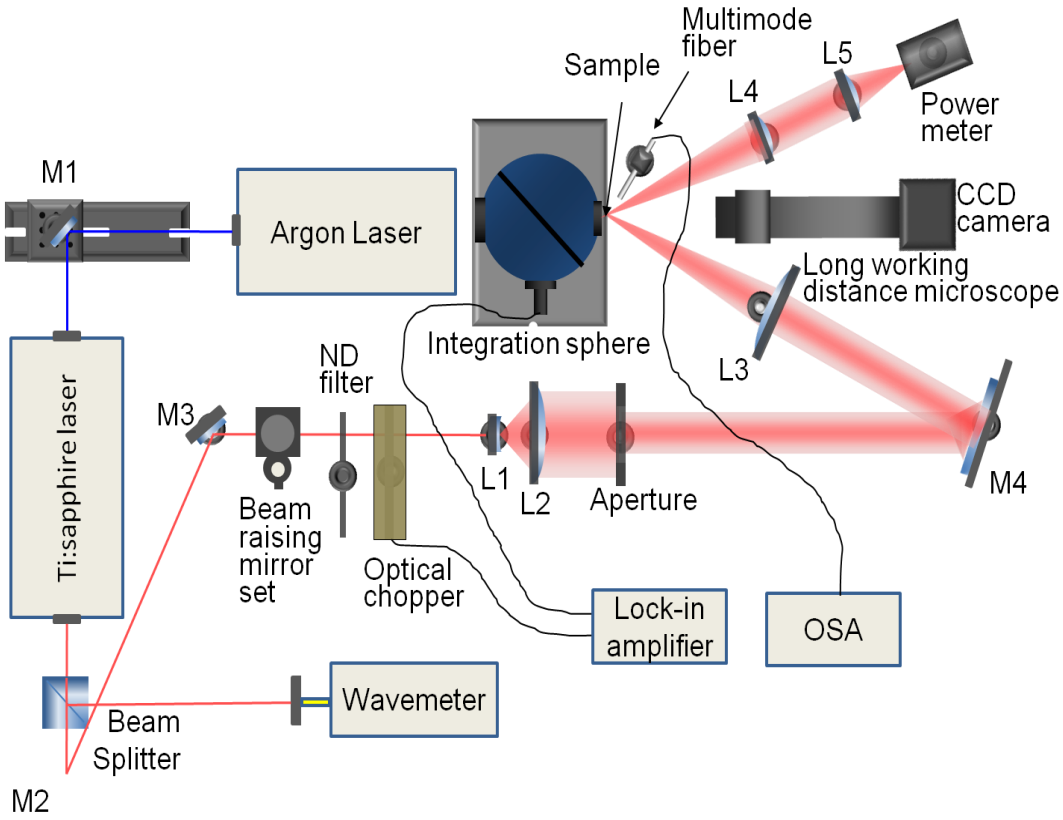

Fig. 7.19. Schematic diagram of the arrangements of optics for the setup.

An Argon laser is used to pump the Ti:sapphire laser, which emits at 820 nm. The laser intensity is attenuated by a neutral density filter. Then the laser beam is expanded to about 20 mm in diameter before focusing on the sample to achieve very tight focus. It is also important to use the fundamental mode of the emission for the same purpose. Then the beam is focused onto the front entrance of the integration sphere where the sample is located. The sample is attached to the front entrance with the front side facing outwards and the back side (hemisphere) facing inwards. The reflected light is collected and measured by a

power meter. Although the optics used in this setup are either plano-convex, plano-concave or doublets and minimize the spherical aberration, the focusing laser spot is still larger than the top metal ring as shown in Fig. 7.20, due to the long focal length of the last focusing lens. The reason for using such a long focal length of 25 cm is to accommodate the microscope, which is used to observe the device. The incident angle is chosen to be about 10 degrees to leave apace for the microscope and it is still easy to focus light to the desired spot compared with vertical incidence. In principle, a microscope objective lens with a beam splitter could be used to focus the laser beam and observe the device and even measure the PL spectrum. However, the laser focusing spot size cannot be freely chosen because the depth of field is quite shallow for objective lenses. Therefore, it is difficult to find an objective lens that focuses laser beam to exactly the inner radius of the top metal ring when it is in focus.

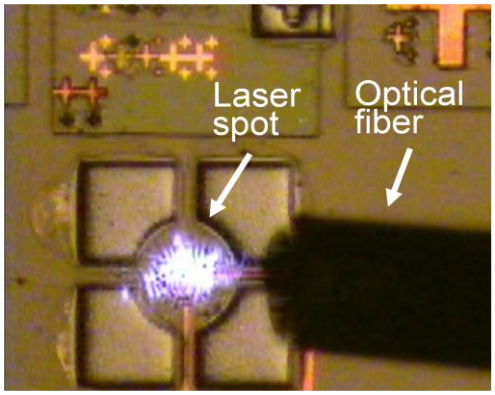

Fig. 7.20. A photograph of a device under laser illumination, where the bright spot is the laser focusing point and the dark rectangular is the shadow of the optical fiber.

The total emission power from the hemisphere side is measured by the integration sphere. The integration sphere diffuses the incident light evenly inside the sphere and a photo detector measures the photon flux through a hole on the side wall of the sphere. Lock-in amplifier and optical chopper are used to increase the signal-to-noise ratio of the photo detector readings. It should be noted that, although most of the LED emission will get out from the hemisphere side, a tiny part (~ 1%) can get out from the top LED surface. This tiny part of emission is probed by a multi-mode fiber connected to an optical spectrum analyzer for PL measurements.

7.5 Optical Testing Results

In the above setup, both the integration sphere and the power meter are used for optical power measurement and a careful calibration is done to insure the consistency of the results from the two instruments. The laser profile is also measured to determine the incident power on the devices. PL measurement is carried out on processed samples as well as the bare wafers with various laser intensities. The internal quantum efficiency (IQE) is calculated based on the pumping power dependent PL intensity measurement. The output power from the hemisphere under laser injection is measured by the integration sphere and is used to determine the external quantum efficiency (EQE). The results are discussed in detail as follows.

7.5.1 Power Meter and Integration Sphere Calibration

In this experiment, both the integration sphere and the power meter are

used for optical power measurement. The power meter measures the optical power using a thermal absorber and features good linearity (< ±1%) over a broad spectral range. The integration sphere measures the optical signal using a Ge detector and good calibration is needed to interpret the total power. Therefore, the laser intensity is measured firstly by the power meter and then by the integration sphere for calibration. Figure 7.21 shows the measurement results by power meter and integration sphere for 820, 860, and 980 nm laser wavelengths at various intensities. The calibration results for the integration sphere at 820, 860, and 980 nm laser wavelengths are 1.68, 2.07, and 7.30 μA/mW, respectively.

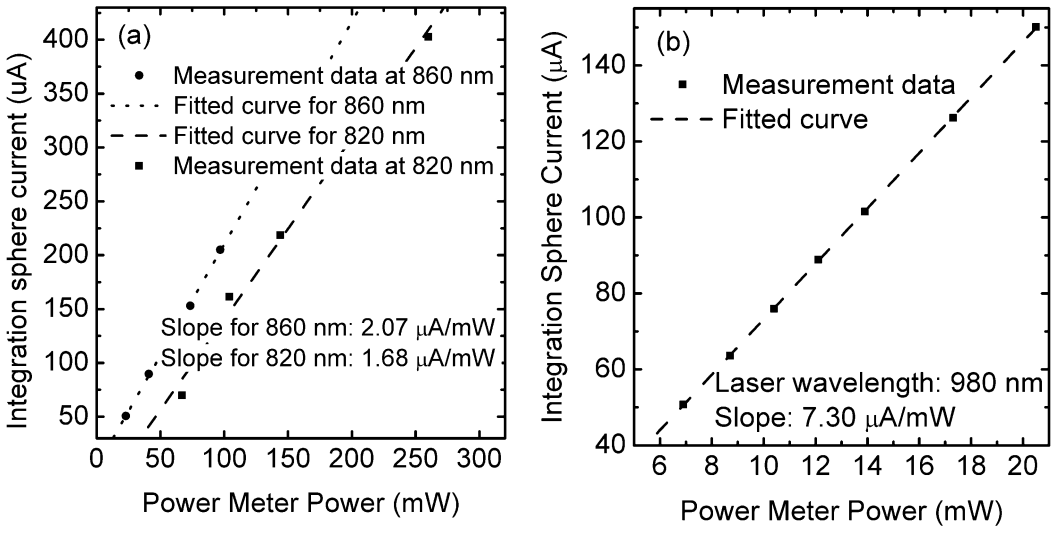

Fig. 7.21. Integration sphere measurement versus power meter measurement for (a) 820, 860, and (b) 980 nm laser wavelengths at various intensities.

7.5.2 Injection Laser Intensity Profile Measurement

The injection laser is carefully tuned to work at the fundamental mode and

the intensity profile follows a Gaussian function. By measuring the percentage of light that passes through pinholes of fixed diameters, the laser intensity profile can be recovered. The results show that 7.5% and 19.3% of the light can pass through pinholes of 15 μm and 25 μm in diameter. The fitted laser intensity profile is shown in Fig. 7.22. For the device under testing, the inner diameter of the top metal ring is 30 μm, which means that 26.6% of the total laser power is effectively incident on the LED. Moreover, assuming the GaAs refractive index to be 3.67 at 820 nm [100], the front surface reflection is 32.7% at 10 ^{o} incident angle from Fresnel's equation. Furthermore, only 17.1% of the incident light can be absorbed by the device active region, assuming the extinction coefficients of InGaAs, GaAs, and AlGaAs to be 0.121, 0.057, and 0.082 [100], respectively. Therefore, only 3.06% and 11.5% of the total laser power is effectively injected for the device and bare wafer (without processing), respectively. This power is defined as the effective injection power.

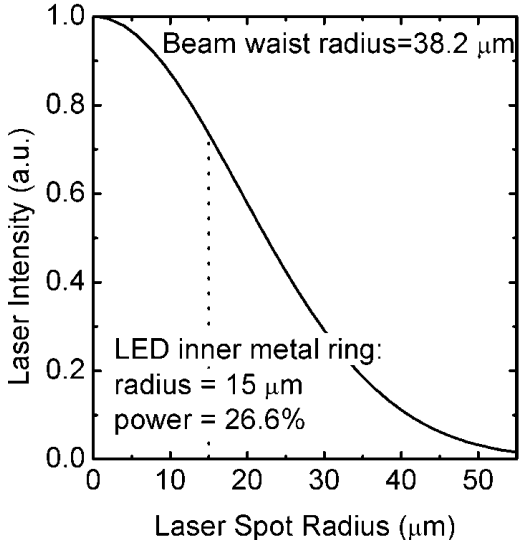

Fig. 7.22. Fitted laser intensity profile.

7.5.3 PL Measurement and IQE Calculation

The PL measurement is carried out on the processed samples as well as the bare wafers (without processing) with various laser intensities and the results are shown in Fig. 7.23. From Fig. 7.23, under high injection levels the maximum red shift of the peak wavelength is below 5 nm, which corresponds to less than 13 K temperature increase from room temperature according to Ref. 144. Figure 7.24 shows the integrated PL intensity versus effective laser injection levels and this data can help to interpret the internal quantum efficiency (IQE), which is defined as the number of net photons generated in the active region over the number of carriers injected into the active region [33]. The basic idea is that the laser intensity can be expressed by the sum of different powers of the PL intensity determined by the rate equation and is given as [122]

$$P_{PL} = A_{PL}\left(L_{PL}\right)^{1/2} + B_{PL}\cdot L_{PL} + C_{PL}\left(L_{PL}\right)^{3/2} \quad , \tag{7.5}$$

where, P_{PL} is the laser injection intensity, L_{PL} is the integrated PL intensity. The A_{PL}, B_{PL} and C_{PL} are fitting parameters, which can be determined by fitting the curves in Fig. 7.24 and are listed in Table 7.1. Moreover, the first term in Eq. 7.5 represents the Shockley-Read-Hall recombination, the second term represents the radiative recombination and the last term represents the Auger recombination. The IQE can be expressed as [122]

$$\eta_i = \left(1 + \frac{A_{PL}}{B_{PL}} L_{LP}^{-1/2} + \frac{C_{PL}}{B_{PL}} L_{LP}^{1/2}\right)^{-1} \quad . \tag{7.6}$$

The IQE versus effective laser injection power is shown in Fig. 7.25. It can be seen that the IQE of the device is lower than that of the bare wafer (without processing). This is mainly due to processing induced defects in the device and note that the recycling factor of a planer LED is also higher than the hemisphere device due to strong light trapping. As the effective injection power increases the difference between the IQE of bare wafer and device becomes. Moreover, the IQE of the bare wafer starts to drop at very high injection levels due to the Auger recombination, while the drop in IQE of the device is not observed due to the low injection levels.

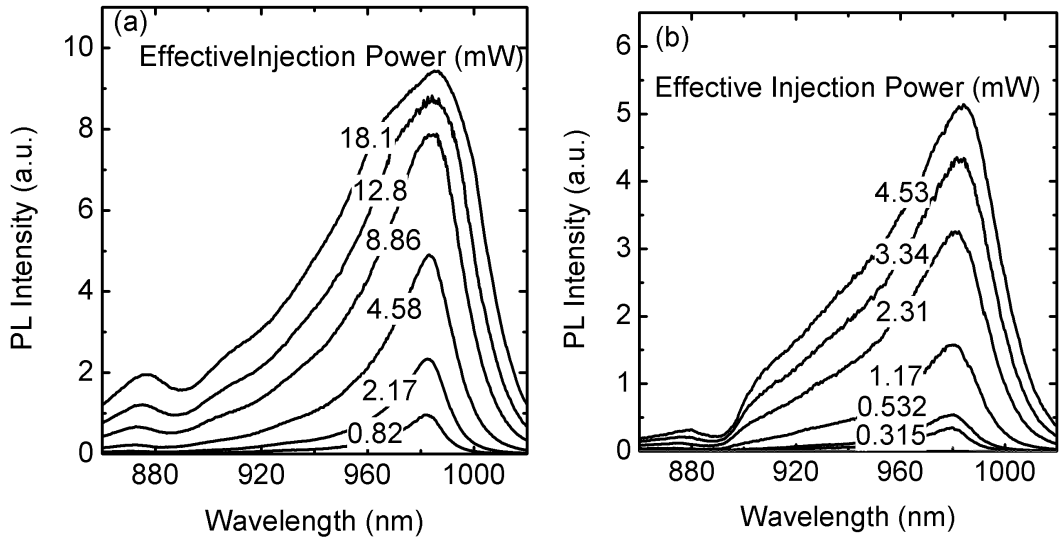

Fig. 7.23. PL spectra of (a) bare wafer (without processing) and (b) device under various laser injection levels.

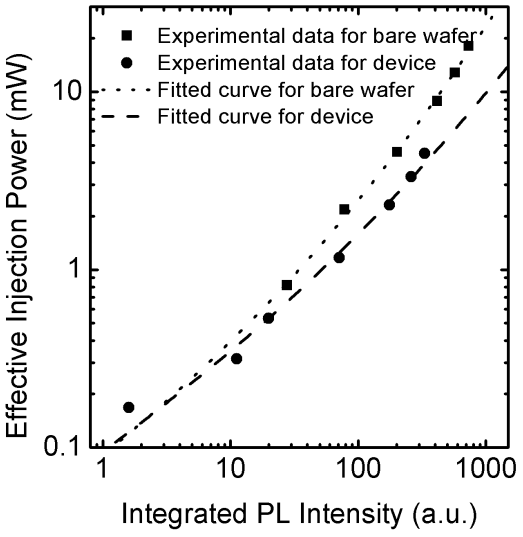

Fig. 7.24. Effective laser injection power versus integrated PL intensity.

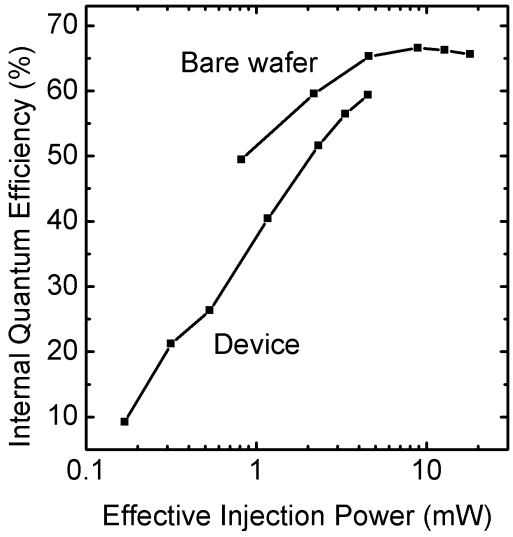

Fig. 7.25. Internal quantum efficiency versus integrated PL intensity.

Table 7.1. Calculated fitting parameters for Eq. 7.5.

	A_{PL}	B_{PL}	C_{PL}
Bare wafer	7.57×10^{-8}	1.50×10^{-14}	1.88×10^{-22}
Device	8.79×10^{-8}	7.06×10^{-15}	N.A.*

* The C_{PL} of the device is too small to be fitted.

7.5.4 EQE and Extraction Efficiency Measurement

The output power under various effective laser injection levels is measured for both the bare wafer (without processing) and device by the integration sphere. Figure 7.26 shows the external quantum efficiency (EQE) versus effective laser injection level for the bare wafer and device. In this work, the EQE is defined as the number of photons collected by the integration sphere over the number of carriers injected into the active region [33]. Figure 7.27 shows the extraction efficiency, defined as the EQE over IQE, versus the effective laser injection level for the bare wafer and device. It can be seen that the average extraction efficiency of the bare wafer and device is about 2.7% and 10.6%, respectively. Although the extraction efficiency is much lower than that theoretically predicted, the GaAs hemisphere does increase the extraction efficiency four times compared to that of a planar LED. The low extraction efficiency is due to the fact that the hemisphere is partially surrounded by the side walls and some of the emission from the hemisphere strikes on the side walls and enters the semiconductor again.

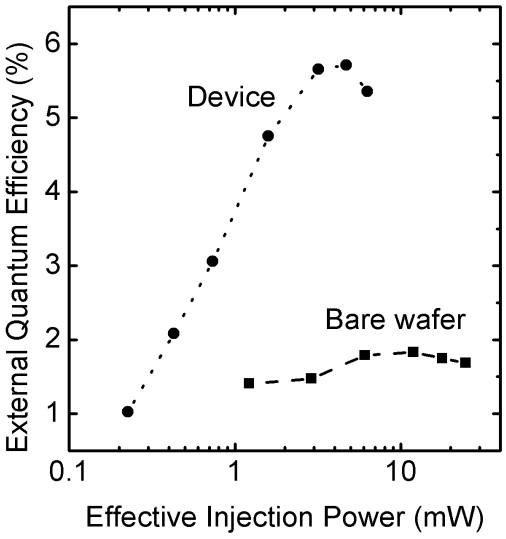

Fig. 7.26. External quantum efficiency versus effective laser injection power.

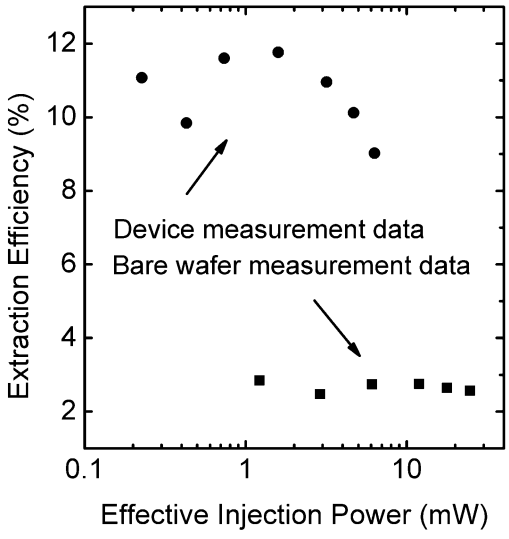

Fig. 7.27. Extraction efficiency versus effective laser injection power.

7.6 Discussion

Devices with hemispheres of 90 μm in radius, active regions of 30 μm in radius and 44% p-contact coverage are successfully fabricated. The overall size of the device is limited by the requirement of a nearly ideal reflowed photoresist droplet profile as a mask to etch near perfect hemispheres, see Fig. 7.7. Furthermore, the light extraction performance of a given hemisphere increases as the size of the active region decreases, see Fig. 6.10. Therefore, to achieve near perfect hemisphere devices with high extraction efficiency, the active region must be small, resulting a reduced power output per hemisphere. Moreover, further increases in the extraction efficiency can be achieved by reducing the metal

contact losses, through reduced contact ring area and by using contact materials that are more reflective.

The testing results show that the device achieves 12% extraction efficiency compared with the theoretical value of 50%. The main reason for the low measured extraction efficiency is that part of the emission from the hemispheres is captured by the side walls surrounding the hemispheres, see Fig 7.16 (b). A metal reflector covering the side walls can effectively reflect the light back into free space and thus increase the extraction efficiency.

VIII. CONCLUSION

A device structure that monolithically integrates a GaAs hemisphere with an InGaAs/GaAs triple quantum-well thin slab LED is proposed to realize semiconductor luminescence refrigeration. Numerical calculations show that the thin slab LED can start cooling below 150 K at optimum injection level if the extraction efficiency is 100%. Simulations show that with optimal designs the hemisphere structure can extract over 99.9% of the light incident upon it, which can result in extraction efficiencies approaching 98% with metal contact coverage approaching zero.

Devices with hemispheres of 90 μm in radius, active regions of 30 μm in radius and 44% p-contact coverage are successfully fabricated using nine times photolithography and eight masks in the ASU class-100 cleanroom. The critical processing steps, such as photoresist reflow and dry etch, are simulated to insure successful processing. As a result, near perfect semiconductor micro hemispheres are fabricated by photoresist reflow and ICP etching. Arrays of GaAs hemispheres are demonstrated with good uniformity showing the potential for large volume fabrication. Moreover, these techniques can also be applied to other important materials, such as Si, GaP, InP and GaSb.

An optical testing setup is built to test the processed devices, which can simultaneously measure the total emission power and micro-photoluminescence (PL) spectrum. The testing results show that the internal quantum efficiency for the devices is close to 6% under optimum injection level compared with the theoretical value of 79%, while the external quantum efficiency is close to 12%

compared with the theoretical value of 50%. Although the measured values are still low, this is the first batch of experiments on real devices targeted for semiconductor luminescence refrigeration. The efficiencies can be increased by further optimization of device design and processing.

REFERENCES

[1] S. M. Sze, and K. K. Ng, *Physics of Semiconductor Devices*, 3rd ed. New Jersey: Wiley, 2007.

[2] A. E. Becquerel, "On Electric Effects under the Influence of Solar Radiation," *Compt. Rend.*, vol. 9, pp. 561-567, 1839.

[3] D. M. Chapin, C. **S.** Fuller, and G. L. Pearson, "A New Silicon p-n Junction Photocell for Converting Solar Radiation into Electrical Power," *J. Appl. Phys*., vol. 25, pp. 676-677, 1954.

[4] http://nssdc.gsfc.nasa.gov/nmc/spacecraftDisplay.do?id=1958-002B

[5] http://inventors.about.com/od/timelines/a/Photovoltaics.htm

[6] S. Kurtz, and J. Geisz, "Multijunction Solar Cells for Conversion of Concentrated Sunlight to Electricity," *Optics Express*, vol. 18, pp. A73-A78, 2010.

[7] Zh. I. Alferov, V. M. Andreev, M. B. Kagan, I. I. Protasov, and V. G. Trofim, ''Solar-energy Converters based on p-n $Al_xGa_{1-x}As$-GaAs Heterojunctions,'' *Sov. Phys. Semicond.*, vol. 4, pp. 2047-2048, 1971.

[8] http://www.solarbuzz.com/technologies.htm

[9] http://en.wikipedia.org/wiki/Solar_cell

[10] J. Zhao, A. Wang, M. A. Green, F. Ferrazza, "Novel 19.8% Efficient 'Honeycomb' Textured Multicrystalline and 24.4% Monocrystalline Silicon Solar Cells," *Appl. Phys. Lett*., vol. 73, pp. 1991-1993, 1998.

[11] O. Schultz, S. W. Glunz, and G. P. Willeke, "Multicrystalline Silicon Solar Cells Exceeding 20% Efficiency," *Prog. Photovolt: Res. Appl.*, vol. 12, pp. 553-558, 2004.

[12] http://www.solarexpert.com/pvbasics2.html

[13] J. Meier, J. Sitznagel, U. Kroll, C. Bucher, S. Fay, T. Moriarty, and A. Shah, "Potential of Amorphous and Microcrystalline Silicon Solar Cells," *Thin Solid Films*, vol. 451-452, pp. 518-524, 2004.

[14] G. J. Bauhuis, P. Mulder, E.J. HaverKamp EJ, J. C. C. M. Huijben, and J. J. Schermer, "26.1% Thin-film GaAs Solar Cell Using Epitaxial Lift-off," *Sol. Energy Mater. Sol. cells*, vol. 93, pp. 1488-1491, 2009.

[15] X. Wu, J. C. Keane, R. G. Dhere, C. DeHart, A. Duda, T. A. Gessert, S. Asher, D. H. Levi, and P. Sheldon, "16.5%-Efficient CdS/CdTe Polycrystalline Thin-film Solar Cell," *Proc. of 17th European Photovoltaic Solar Energy Conference*, Munich, pp. 995-1000, 2001.

[16] I. Repins, M. A. Contreras, B. Egaas, C. DeHart, J. Schart, C. L. Perkins, B. To, and R. Noufi, "19.9%-Efficienct ZnO/CdS/$CuInGaSe_2$ Solar Cell with 82.1% Fill Factor," *Prog. Photovolt: Res. Appl.*, vol. 16, pp. 235-239, 2008.

[17] E. D. Jackson, "Areas for Improving of the Semiconductor Solar Energy Converter," *Trans. Conf. on Use of Solar En. 1955*, Tucson, U. of Arizona Press, vol. 5, pp. 122-125, 1958.

[18] M. Wolf, "Limitations and Possibilities for Improvement of Photovoltaic Solar Energy Converters," *Proc. of the IRE*, vol. 48, pp. 1246-1263, 1960.

[19] J. A. Hutchby, R. J. Markunas, and S. M. Bedair, Photovoltaics, *Proc. of the SPIE*, vol. 543, pp. 543, 1985.

[20] J. F. Geisz, S. Kurtz, M. W. Wanlass, J. S. Ward, A. Duda, D. J. Friedman, J. M. Olson, W. E. McMahon, T. E. Moriarty, and J. T. Kiehl, "High-efficiency GaInP/GaAs/InGaAs Triple-junction Solar Cells Grown Inverted with a Metamorphic Bottom Junction," *Appl. Phys. Lett.*, vol. 91, pp. 023502-1 – 023502-3, 2007.

[21] R. R. King, A. Boca, W. Hong, X.-Q. Liu, D. Bhusari, D. Larrabee, K. M. Edmondson, D. C. Law, C. M. Fetzer, S. Mesropian, N. H. Karam, "Band-Gap-Engineered Architectures for High-Efficiency Multijunction

Concentrator Solar Cells," in *Proc. of 24th European Photovoltaic Solar Energy Conference 2009*, Hamburg, pp. 55-61, 2009.

[22] S. Goya, Y. Nakano, N. Yamashita, S. Morita, and Y. Yonekura, "Development of Amorphous Silicon/ microcrystalline Silicon Tandem Solar Cells," *Proc. of 3rd World Conf. on Photovoltaic Energy Conversion 2003*, Osaka, pp. 1570-1573, 2003.

[23] K. W. J. Barnham, and G. Duggan, "A New Approach to High-efficiency Multi-band-gap Solar Cells," *J. Appl. Phys.*, vol. 67, pp. 3490-3493, 1990.

[24] K. Barnham, J. Connolly, P. Griffin, G. Haarpaintner, J. Nelson, E. Tsui, A. Zachariou, J. Osborne, C. Button, G. Hill, M. Hopkinson, M. Pate, J. Roberts, and T. Foxon, "Voltage Enhancement in Quantum Well Solar Cells," *J. Appl. Phys.*, vol. 80, pp. 1201-1206, 1996.

[25] M. Mazzer, K. W. J. Barnham, I. M. Ballard, A. Bessiere, A. Ioannides, D. C. Johnson, M. C. Lynch, T. N. D. Tibbits, J. S. Roberts, G. Hill, and C. Calder, "Progress in Quantum Well Solar Cells," *Thin Solid Films*, vol. 511-512, pp. 76-83, 2006.

[26] P. V. Kamat, "Quantum Dot Solar Cells. Semiconductor Nanocrystals as Light Harvesters," *J. Phys. Chem. C*, vol. 112, pp. 18737-18753, 2008.

[27] A. Kongkanand, K. Tvrdy, K. Takechi, M. K. Kuno, and P. V. Kamat, "Quantum Dot Solar Cells. Tuning Photoresponse through Size and Shape Control of CdSe-TiO_2 Architecture," *J. Am. Chem. Soc.*, vol. 130, pp. 4007-4015, 2008.

[28] R. T. Ross, and A. J. Nozik, "Efficiency of Hot-carrier Solar Energy Converters," *J. Appl. Phys.*, vol. 53, pp. 3813-3818, 1982.

[29] R. D. Schaller, and V. I. Klimov, "High Efficiency Carrier Multiplication in PbSe Nnaocrystals: Implications for Solar Energy Conversion," *Phys. Rev. Lett.*, vol. 92, pp. 186601-1 - 186601-4, 2004.

[30] R. D. Schaller, V. M. Agranovich, and V. C. Klimov, "High Efficiency Carrier Multiplication through Direct Photogeneration of Multi-excitons via Virtual Single-exciton States," *Nat. Phys.*, vol. 1, pp. 189-195, 2005.

[31] W. Shockley, and H. J. Queisser, "Detailed Balance Limit of Efficiency of p-n Junction Solar Cells," *J. Appl. Phys.*, vol. 32, pp. 510-519, 1961.

[32] Standard Tables for Reference Solar Spectral Irradiances: Direct Normal and Hemispherical on 37˚ Tilted Surface, ASTM G173-03-2008.

[33] D. Ding, Thermal Dynamic Analysis and Determination of Spontaneous Emission Quantum Efficiency for Luminescence Refrigeration in Semiconductors, Ph.D. Dissertation, Arizona State University, 2008.

[34] M. A. Green, "The Path to 25% Silicon Solar Cell Efficiency: History of Silicon Cell Evolution," *Prog. Photovolt: Res. Appl.*, vol. 17, pp. 183-189, 2009.

[35] A. Flat, and A. G. Milnes, "Optimization of Multi-layer Front-contact Grid Patterns for Solar Cells," *Solar Energy*, vol. 23, pp. 289-299, 1979.

[36] H. B. Serreze, "Optimizing Solar Cell Performance by Simultaneous Consideration of Grid Pattern Design and Interconnection Configuration," in *Conf. Record of 13th IEEE Photovoltaic Specialists Conf.*, pp. 609-614, 1978.

[37] W. Beyer, J. Hupkes, and H. Stiebig, "Transparent Conducting Oxide Films for Thin Film Silicon Photovoltaics," *Thin Solid Films*, vol. 516, pp. 147-154, 2007.

[38] T. J. Coutts, D. L. Young, X. Li, W. P. Mulligan, and X. Wu, "Search for Improved Transparent Conducting Oxides: A Fundamental Investigation of CdO, Cd_2SnO_4, and Zn_2SnO_4," *J. Vac. Sci. Technol. A*, vol. 18, pp. 2646-2660, 2000.

[39] L. Hu, D. S. Hecht, and G. Gruner, "Infrared Transparent Carbon Nanotube Thin Films," *Appl. Phys. Lett.*, vol. 94, pp. 081103-1 – 081103-3, 2009.

[40] M. A. Contreras, T. Barnes, J. van de Lagemaat, G. Rumbles, T. J. Coutts, C. Weeks, P. Clatkowski, I. Levitsky, J. Peltola, and D. A. Britz, "Replacement of Transparent Conductive Oxides by Single-wall Carbon Nanotubes in Cu(In,Ga)Se_2-based Solar Cells," *J. Phys. Chem. C*, vol. 111, pp. 14045-14048, 2007.

[41] C. M. Chong, S. R. Wenham, and M. A. Green, "High-efficiency, Laser Textured, Buried Contact Silicon Solar Cell," *Appl. Phys. Lett.*, vol. 52, pp. 407-409, 1988.

[42] S. R. Wenham, B. O. Chan, C. B. Hongsberg, and M. A. Green, "Beneficial and Constraining Effects of Laser Scribing in Buried-contact Solar Cells," *Prog. Photovolt: Res. Appl.*, vol. 5, pp. 131-137, 1997.

[43] M. D. Lammert, and R. J. Schwartz, "The Integrated Back Contact Solar Cell: A Silicon Solar Cell for Use in Concentrated Sunlight," *IEEE Transactions on Electron Devices*, vol. 24, pp. 337-342, 1977.

[44] E. van Kerschaver, and G. Beaucame, "Back-contact Solar Cells: A Review," *Prog. Photovolt: Res. Appl.*, vol. 14, pp. 107-123, 2006.

[45] F. W. Sexton, "Plasma Nitride AR Coatings for Silicon Solar Cells," *Solar Energy Mater.*, vol. 7, pp. 1-14, 1982.

[46] R. Kishore, S. N. Singh, and B. K. Das, "PECVD Grown Silicon Nitride AR Coatings on Polycrystalline Silicon Solar Cells," *Solar Energy Mater. Sol. cells*, vol. 26, pp. 27-35, 1992.

[47] Z. Chen, P. Sana, J. Salami, and A. Rohatgi, "A Novel and Effective PECVD SiO_2/SiN Antireflection Coating for Si Solar Cells," *IEEE Trans. Electron Devices*, vol. 40, pp. 1161-1165, 1993.

[48] K. Ram, S. N. Singh, and B. K. Das, "Screen Printed Titanium Oxide and PECVD Silicon Nitride as Antireflection Coating on Silicon Solar Cells," *Renewable Energy*, vol. 12, pp. 131-135, 1997.

[49] C. Battaglin, F. Caccavale, A. Menelle, M. Montecchi, E. Nichelatti, and F. Nicoletti, "Characterization of Antireflective TiO_2//SiO_2 Coatings by

Complementary Techniques," *Thin Solid Films*, vol. 351, pp. 176-179, 1999.

[50] U. Gangopadhyay, K. Kim, D. Mangalaraj, and J. Yi, "Low Cost CBD ZnS Antireflection Coating on Large Area Commercial Mono-crystalline Silicon Solar Cells," *Appl. Surf. Sci.*, vol. 230, pp. 364-370, 2004.

[51] I. O. Parm, K. Kim, D. G. Lim, J. H. Lee, J. H. Heo, J. Kim, D. S. Kim, S. H. Lee, and J. Yi, "High-density Inductively Coupled Plasma Chemical Vapor Deposition of Silicon Nitride for Solar Cell Application," *Solar Energy Mater. Sol. cells*, vol. 74, pp. 97-105, 2002.

[52] C. Martinet, V. Paillard, A. Gagnaire, and J. Joseph, "Deposition of SiO_2 and TiO_2 Thin Films by Plasma enhanced Chemical Vapor Deposition for Antireflection Coating," *Non-Crystalline Solids*, vol. 216, pp. 77-82, 1997.

[53] H. Nagel, A. Metz, and R. Hezel, "Porous SiO_2 Films Prepared by Remote Plasma-enhanced Chemical Vapor Deposition – a Novel Antireflection Coating Technology for Photovoltaic Modules," *Sola Energy Mater. Sol. cells*, vol. 65, pp. 71-77, 2001.

[54] S.-Y. Lien, D.-S. Wuu, W.-C. Yeh, and J.-C. Liu, "Tri-layer Antireflection Coatings (SiO_2/SiO_2-TiO_2/TiO_2) for Silicon Solar Cells Using a Sol-gel Technique," *Sol. Energy Mater. Sol. cells*, vol. 90, pp. 2710-2719, 2006.

[55] C. Baur, A.W. Bett, F. Dimroth, G. Siefer, M. Meusel, W. Bensch, W. Kostler, and G. Strobl, "Triple-junction III-V Based Concentrated Solar Cells: Perspectives and Challenges," *J. Sol. Energy Eng.*, vol. 129, pp. 258-265, 2007.

[56] S.-N. Wu, D. Ding, S. R. Johnson, S.-Q. Yu, and Y.-H. Zhang, "Four-junction Solar Cells Using Lattice-matched II-VI and III-V Semiconductors," *Prog. Photovolt: Res. Appl.*, vol.18, pp.328-333, 2010.

[57] S. Wang, D. Ding, X. Liu, X.-B. Zhang, D. J. Smith, J. K. Furdyna, and Y.-H. Zhang, "MBE Growth of II-VI Materials on GaSb Substrates for Photovoltaics Applications," *J. Cryst. Growth*, vol. 311, pp. 2116-2119, 2009.

[58] S. V. Ivanov, "Novel Materials and Designs for Long-Living II-VI Blue-Green Lars," *phys. stat. sol. (a)*, vol. 192, pp. 157-165, 2002.

[59] M. Ozawa, F. Hiei, M. Takasu, A. Ishibashi, and K. Akimoto, "Low Resistance Ohmic Contacts for p-type ZnTe," *Appl. Phys. Lett.*, vol. 64, pp. 1120-1122, 1994.

[60] J. H. Chang, T. Takai, B. H. Koo, J. S. Song, T. Handa, and T. Yao, "Aluminum-doped n-type ZnTe Layer Grown by Molecular-beam Epitaxy," *Appl. Phys. Lett.*, vol. 79, pp. 785-787, 2001.

[61] K. Katayama, H. Matsubara, F. Nakanishi, T. Nakamura, H. Doi, A. Saegusa, T. Mitsui, T. Matsuoka, M. Irikura, T. Takeke, S. Nishine, and T. Shirakawa, "ZnSe-based White LEDs," *J. Cryst. Growth*, vol. 214-215, pp. 1064-1070, 2000.

[62] R. R. King, D. C. Law, K. M. Edmondson, C. M. Fetzer, G. S. Kinsey, H. Yoon, R. A. Sherif, and N. H. Karam, "40% Efficient Metamorphic GaInP/GaInAs/Ge Multijunction Solar Cells," *Appl. Phys. Lett.*, vol. 90, pp. 183516-1 – 183516-3, 2007.

[63] W. Guter, J. Schone, S. P. Philips, M. Steiner, G. Siefer, A. Wekkeli, E. Welser, E. Oliva, A. W. Bett, and F. Dimroth, "Current-matched Triple-Junction Solar Cell Reaching 41.1% Conversion Efficiency under Concentrated Sunlight," *Appl. Phys. Lett.*, vol. 94, pp. 223504-1 – 223504-3, 2009.

[64] J. F. Geisz, S. Kurtz, M. W. Wanlass, J. S. Ward, A. Duda, D. J. Friedman, J. M. Olson, W. E. McMahon, T. E. Moriarty, and J. T. Kiehl, "High-efficiency GaInP/GaAs/InGaAs Triple-junction Solar Cells Grown Inverted with a Metamorphic Bottom Junction," *Appl. Phys. Lett.*, vol. 91, pp. 023502-1 – 023502-3, 2007.

[65] J. F. Geisz, D. J. Friedman, J. S. Ward, A. Duda, W. J. Olavarria, T. E. Moriarty, J. T. Kiehl, M. J. Romero, A. G. Norman, and K. M. Jones, "40.8% Efficient Inverted Triple-junction Solar Cell with Two Independently Metamorphic Junctions," *Appl. Phys. Lett.*, vol. 93, pp. 123505-1 – 123505-3, 2008.

[66] D. B. Jackrel, S. R. Bank, H. B. Yuen, M. A. Wistey, J. S. Harris, A. J. Ptak, S. W. Johnston, D. J. Friedman, and S. R. Kurtz, "Dilute Nitride GaInNAs and GaInNAsSb Solar Cells by Molecular Beam Epitaxy," *J. Appl. Phys.*, vol. 101, pp. 114916-1 – 114916-8, 2007.

[67] R. R. King, D. C. Law, K. M. Edmondson, C. M. Fetzer, G. S. Kinsey, H. Yoon, D. D. Kurt, J. H. Ermer, R. A. Sherif, and N. H. Karam, "Advances in High-efficiency III-V Multijunction Solar Cells," *Advances in OptoElectronics*, vol. 2007, pp. 29523-1 – 29523-8, 2007.

[68] A. J. Ptak, D. J. Friedman, S. Kurt, and R. C. Reedy, "Low-acceptor-concentration GaInNAs Grown by Molecular-beam Epitaxy for High-current *p-i-n* Solar Cell Applications," *J. Appl. Phys.*, vol. 98, pp. 94501-1 – 94501-5, 2005.

[69] W. Lin, A. Cavus, L. Zeng, and M. C. Tamargob, "N-type Doping of Lattice-Matched ZnCdSe and $Zn_xCd_yMg_{1-x-y}Se$ Epilayers on InP Using $ZnCl_2$," *J. Appl. Phys.*, vol. 84, pp. 1472-1475, 1998.

[70] W. Lin, S. P. Guo, and M. C. Tamargob, "P-type Doping of (Zn, Mg, Cd)Se Alloys Using a Radio Frequency Discharge Nitrogen Plasma Source," *J. Vac. Sci. Technol. B*, vol. 18, pp. 1534-1537, 2000.

[71] S. Adachi, Properties of group-IV, III-V and II-VI semiconductors, West Sussex: Wiley, 2005.

[72] N. Yu. Gordeev, S. V. Ivanov, V. I. Kopchatov, I. I. Novikov, T. V. Shubina, N. D. Il'inskaya, P. S. Kopev, G. Reuscher, A. Waag, and G. Landwehr, "Improved Degradation Stability of Blue–Green II–VI Light-Emitting Diodes with Excluded Nitrogen-Doped ZnSe-Based Layers," *Semiconductors*, vol. 35, pp. 1340–1344, 2001.

[73] S. V. Ivanov, "Novel Materials and Designs for Long-Living II–VI Blue-Green Lasers," *phys. stat. sol. (a)*, vol. 192, pp. 157–165, 2002.

[74] M. Adachi,, Z. M. Aung, K. Minami, K. Koizumi, M. Watanabe, S. Kawamoto, T. Yamaguchi, H. Kasada, T. Abe, K. Ando, K. Nakano, A. Ishibashi, S. Itoh, "Microscopic Defect Induced Slow-mode Degradation

in II-VI based Blue-green Laser Diodes," *J. of Crystal Growth*, vol. 214/215, pp. 1035-1039, 2000.

[75] K. Kishino, I. Nomura, Y. Ochiai, and S.-B. Che, "ZnCdTe/ZnTe LED with CdSe n-Type Contact Layers Grown on ZnTe Substrates by Molecular Beam Epitaxy," *phys. stat. sol. (b)*, vol. 229, pp. 991-994, 2002.

[76] I. W. Tao, M. Jurkovic, and W. I. Wang, "Doping of ZnTe by Molecular Beam Epitaxy," *Appl. Phys. Lett.*, vol. 64, pp. 1848-1849, 1994.

[77] M. Nishio, Q. Guo, H. Ogawa, "Ohmic Ccontacts to p-type ZnTe Using Electroless Pd," *Thin Solid Films*, vol. 343-344, pp. 508-511, 1999.

[78] T. Ohtsuka, M. Yoshimura, K. Morita, and M. Koyama, T. Yao, "Low Resistance Ohmic Contact for p-type ZnTe Using Au Electrode," *Appl. Phys. Lett.*, vol. 67, pp. 1277-1279, 1995.

[79] K. Mochizuki, A. Terano, M. Momose, A. Taike, M. Kawata, J. Gotoh, and Shin-ichi Nakatsuka, "Crystallographic Microstructure and Electrical Characteristics of Au/Pt/Ti/Ni Ohmic Contacts on p-type (001) ZnTe Layers," *J Appl. Phys.*, vol. 78, pp. 3216-3220, 1995.

[80] J. F. Chen, and A. Y. Cho, "Characterization of Te-doped GaSb Grown by Molecular Beam Epitaxy Using SnTe," J. Appl. Phys., vol. 70, pp. 277-281, 1991.

[81] R. Wiersma, J. A. H. Stotz, O. J. Pitts, C. X. Wang, M. L. W. Thewalt, and S. P. Watkins, "P-type Carbon Doping of GaSb," *J. Electronic Materials*, vol. 30, pp. 1429-1432, 2001.

[82] K. F. Longenbach, S. Xin, W. I. Wang, "P-type Doping of GaSb by Ge and Sn Grown by Molecular Beam Epitaxy," *J. Appl. Phys.*, vol. 69, pp. 3393-3395, 1991.

[83] K. Hayashida, M. Nishio, Y. Mitsuishi, Q. Guo, Qixin; H. Ogawa, "Growth of n-type ZnTe Films and Formation of Ohmic Contacts," *Proc. SPIE 4th International Conf. on Thin Film Phys. and Applications*, vol. 4086, pp. 248-251, 2000.

[84] T. Nakamura, K. Katayama, H. Mori, and S. Fujiwara, "Novel Cladding Structure for ZnSe-based White LEDs with Longer Lifetime over 10,000 Hours," *phys. stat. sol. (b)*, vol. 241, pp. 2659–2663, 2004.

[85] H. S. Hajghassem and W. D. Brown, "Stable Ohmic Contacts to Zinc Telluride," *Microelectronics and Reliability*, vol. 27, pp. 677-684, 1987.

[86] M. Ozawa, F. Hiei, A. Ishibashi, and K. Akimoto, "Au(Pt)Pd Ohmic Contacts to p-ZnTe," *Elec. Lett.*, vol. 29, pp. 503-505, 1993.

[87] E Janik and R Triboulet, "Ohmic Contacts to p-type Cadmium Telluride and Cadmium Mercury Telluride," *J. Phys. D: Appl. Phys.*, vol. 16 pp. 2333-2340, 1983.

[88] S. J. Eglash, H. K. Choi, G. W. Turner, and M. C. Finn, "MBE Growth of GaInAsSb/AlGaAsSb Double Heterostructures for Diode Lasers Emitting beyond 2 μm," *Mat. Res. Soc. Symp. Proc.*, vol. 216, pp. 207-212, 1991.

[89] S. J. Eglash, and H. K. Choi, "Efficient GaInAsSb/AlGaAsSb Diode Lasers Emitting at 2.29 μm," *Appl. Phys. Lett.*, vol. 57, pp. 1292-1294, 1990.

[90] X. B. Zhang, S. Wang, D. Ding, X. Liu, J.-H. Tan, J. K. Furdyna, Y.-H. Zhang, and D. J. Smith, "Structural Characterization of Integrated II-VI and III-V Heterostructures for Solar Cell Applications," *J. Electronic Materials*, vol. 38, pp. 1558-1562, 2009.

[91] C. H. Henry, "Limiting Efficiencies of Ideal Single and Multiple Energy Gap Terrestrial Solar Cells," *J. Appl. Phys.*, vol. 51, pp. 4494-4500, 1980.

[92] ATLAS User's Manual Device Simulation Software Copyright 2007, SILVACO International, 2007.

[93] D. Vasileska, and S. M. Goodnick, *Computional Electronics*, 1st ed. Morgan & Claypool, 2006.

[94] S. R. Johnson, and T. Tiedje, "Temperature Dependence of the Urbach Edge in GaAs," *J. Appl. Phys.*, vol. 78, pp. 5609-5613, 1995.

[95] R. A. Abram, G. N. Childs, and P. A. Saunderson, "Bang Gap Narrowing due to Many-Body Effects in Silicon and Gallium Arsenide," *J. Phys. C: Solid State Phys.*, vol. 17, pp. 6105-6125, 1984.

[96] C.-H. Wu, S.-M. Liao, and K.-C. Chang, "Ni/Pd/Au Ohmic Contact for p-GaAs and its Application in Red RCLED," *Mater. Sci. Eng. B*, vol. 117, pp. 205-209, 2005.

[97] R. Williams, *Modern GaAs Processing Methods*, Norwood, MA: ARTEC HOUSE, 1990, pp. 222-226.

[98] S. R. Lunt, G. N. Ryba, P. G. Santangelo, and N. S. Lewis, "Chemical Studies of the Passivation of GaAs Surface Recombination Using Sulfides and Thiols," *J. Appl. Phys.*, vol. 70, pp. 7449 - 7467, 1991.

[99] S. Adachi, "Band Gaps and Refractive Indices of AlGaAsSb, GaInAsSb, and InPAsSb: Key Properties for a Variety of the 2–4-μm Optoelectronic Device Applications," *J. Appl. Phys.*, vol. 61, pp. 4869 - 4876, 1987.

[100] E. D. Palik, *Handbook of Optical Constants of Solids*, New York: Academic Press, 1985.

[101] T. Yamada, E. Tokumitsu, K. Saito, T. Akatsuka, M. Miyauchi, M. Konagai, and K. Takahashi, "Heavily Carbon Doped p-Type GaAs and GaAlAs Grown by Metalorganic Molecular Beam Epitaxy," *J. Cryst. Growth*, vol. 95, pp. 145-149, 1989.

[102] K. Jandieri, S. D. Baranovskii, W. Stolz, F. Gebhard, W. Guter, M. Hermle, and A. W. Bett, "Fluctuations of the Peak Current of Tunnel Diodes in Multi-Junction Solar Cells," *J. Phys. D: Appl. Phys.*, vol. 42, pp. 155101-1 – 155101-8, 2009.

[103] M. Hermle, G. Létay, S. P. Philipps, A. W. Bett, "Numerical Simulation of Tunnel Diodes for Multi-Junction Solar Cells," *Progress in Photovoltaics: Research and Application*s, vol. 16, pp. 409 – 418, 2008.

[104] P. Pringsheim, "Zwei Bemerkungen über den Unterschied von Lumineszenzund Temperature-strahlung," *Z. Phys.*, vol. 57, pp. 739-746, 1929.

[105] H. R. I. Epstein, M. I. Buchwald, B. C. Edwards, T. R. Gosnell, and C. E. Mungan, "Observation of Laser-induced Fluorescent Cooling of a Solid," *Nature (London)*, vol. 377, pp. 500-503, 1995.

[106] M. Sheik-Bahae, and R. I. Epstein, "Can Laser Light Cool Semiconductors?" *Phys. Rev. Lett.*, vol. 92, pp. 247403-1 – 247403-4, 2004.

[107] E. Finkeißen, M. Potemski, P. Wyder, L. Vina, and G. Weimann, "Cooling of a Semiconductor by Luminescence Up-conversion", *Appl. Phys. Lett.*, vol. 75, pp. 1258-1260, 1999.

[108] D.-H. Huang, T. Apostolova, P. M. Alsing, and D.A. Cardimona, "Theoretical Study of Laser Cooling of a Semiconductor", *Phys. Rev. B*, vol. 70, 033203-1 – 033203-4, 2004.

[109] G. C. Dousmanis, C. W. Mueller, H. Nelson, and K.G. Petzinger, "Evidence of Refrigerating Action by Means of Photon Emission in Semiconductor Diodes," *Phys. Rev.* vol. 133, pp. A316-A318, 1964.

[110] K. P. Pipe, R. J. Ram, and A. Shakouri, "Bias-dependent Peltier Coefficient and Internal Cooling in Bipolar Devices", *Phys. Rev. B*, vol. 66, pp. 125316-1 – 125316-11, 2002.

[111] A. G. Mal'shukov and K. A. Chao, "Opto-Thermionic Refrigeration in Semiconductor Heterostructures," *Phys. Rev. Lett*. vol. 86, 24, pp. 5570-5573, 2001.

[112] S.-Q. Yu, Gallium Arsenide Based Optoelectronic Devices, Ph.D. Dissertation, Arizona State University, 2005.

[113] D. Ding, S. R. Johnson, J. -B. Wang, S. -Q. Yu, and Y. -H. Zhang, "Determination of Spontaneous Emission Quantum Efficiency in

InGaAs/GaAs Quantum Well Structures," *Proc. of the SPIE*, vol. 6841, pp. 68410D-1 - 68410D-8, 2007.

[114] I. Schnitzer, E. Yablonovitch, C. Caneau, T. J. Gmitter, and A. Scherer, "30% External Quantum Efficiency from Surface Textured, Thin Film Light-Emitting Diodes," *Appl. Phys. Lett.*, vol. 63, pp. 2174-2176, 1993.

[115] H. Luo, J. K. Kim, and E. F. Schubert, J. Cho, C. Sone, and Y. Park, "Analysis of High Power Packages for Phosphor-Based White-Light-Emitting Diodes," *Appl. Phys. Lett.*, vol. 86, pp. 243505-243507, 2005.

[116] A. A. Erchak, D. J. Ripin, S. Fan, P. Rakich, J. D. Joannopoulos, E. P. Ippen, G. S. Petrich, and L. A. Kolodziejski, "Enhanced Coupling to Vertical Radiation Using a Two-Dimensional Photonic Crystal in a Semiconductor Light-Emitting Diode," *Appl. Phys. Lett.*, vol. 78, pp. 563-565, 2001.

[117] J. J. Wierer Jr., A. David, and M. M. Megens, "III-Nitride Photonic-Crystal Light-Emitting Diodes with High Extraction Efficiency," *Nature Photonics*, vol. 3, pp. 163-169, 2009.

[118] J.-B. Wang, Electronic and Optical Properties of Novel Semiconductor Heterostructures, Ph.D. Dissertation, Arizona State University, 2005.

[119] S.-L. Chuang, *Physics of Optoelectronic Devices*, New York: Wiley, 1995.

[120] Ü. Özgür, Ya. I. Alivov, C. Liu, A. Teke, M. A. Reshchikov, S. Doğan, V. Avrutin, S.-J. Cho, and H. Morkoç, "A Comprehensive Review of ZnO Materials and Devices," *J. Appl. Phys.*, vol. 98, pp. 041301-1 – 041301-103, 2005.

[121] W. G. Spitzer, and J. M. Whelan, "Infrared Absorption and Electron Effective Mass in N-type Gallium Arsenide" *Phys. Rev.*, vol. 114, pp. 59-63, 1959.

[122] J.-B. Wang, D. Ding, S. R. Johnson, S.-Q. Yu, and Y.-H. Zhang, "Determination and Improvement of Spontaneous Emission Quantum

Efficiency in GaAs/AlGaAs Heterostructures Grown by Molecular Beam Epitaxy," *phys. stat. sol.* (*b*), vol. 244, pp. 2740-2751, 2007.

[123] Z. D. Popovic, R. A. Sprague, and G. A. Neville Connell, "Technique for Monolithic Fabrication of Microlens Arrays," *Appl. Opt.*, vol. 27, pp. 1281-1284, 1988.

[124] B.-K. Lee, K. J. Cha, and T. H. Kwon, "Fabrication of Polymer Micro/Nano-Hybrid Lens Array by Microstructured Anodic Aluminum Oxide (AAO) Mold," *Microelectronic Engineering*, vol. 86, pp. 857-860, 2009.

[125] C. Y. Chang, S. Y. Yang, and J. L. Sheh, "A Roller Embossing Process for Rapid Fabrication of Microlens Arrays on Glass Substrates," *Microsyst. Technol.*, vol. 12, pp. 754-759, 2006.

[126] J. D. Rogers, A. H. O. Karkkainen, T. Tkaczyk, J. T. Rantala, and M. R. Descour, "Realization of Refractive Microoptics through Grayscale Lithographic Pattering of Photosensitive Hybrid Glass," *Optics Express*, vol. 12, pp. 1294-1303, 2004.

[127] E. Bonaccurso, H.-J. Butt, B. Hankeln, B. Niesenhaus, and K. Graf, "Fabrication of Microvessels and Microlenses from Polymers by Solvent Droplets," *Appl. Phys. Lett.*, vol. 86, pp. 124101-124103, 2005.

[128] K. Naessens, H. Ottevaere, P. Van Daele, and R. Baets, "Flexible Fabrication of Microlenses in Polymer Layers with Excimer Laser Ablation," *Appl. Surface Sci.*, vol. 208-209, pp. 159-164, 2003.

[129] J. Tan, M. Shan, C. Zhao, and J. Liu, "Design and Fabrication of Diffractive Microlens Arrays with Continuous Relief for Parallel Laser Direct Writing," *Appl. Opt.*, vol. 47, pp. 1430-1433, 2008.

[130] Y. Fu, and N. K. Bryan, "Semiconductor Microlenses Fabricated by One-step Focused Ion Beam Direct Writing," *IEEE Trans. on Semicon. Manufacturing*, vol. 15, pp. 229-231, 2002.

[131] E. M. Strzelecka, G. D. Robinson, M. G. Peters, F. H. Peters, and L. A. Coldren, "Monolithic Integration of Vertical-cavity Laser Diodes with Refractive GaAs Microlenses," *Electron. Lett.*, vol. 31, pp. 724-725, 1995.

[132] M. Eisner, and J. Schwider, "Transferring Resist Microlenses into Silicon by Reactive Ion Etching," *Opt. Eng.*, vol. 35, pp. 2979-2982, 1996.

[133] T. N. Oder, J. Shakya, J. Y. Lin, and H. X. Jiang, "Nitride Microlens Arrays for Blue and UV Wavelength Applications," *Appl. Phys. Lett.*, vol. 82, pp. 3692-3694, 2003.

[134] Si-Hyun Park, Heonsu Jeon, Youn-Joon Sung, and Geun-Young Yeom, "Refractive Sapphire Microlenses Fabricated by Chlorine-Based Inductively Coupled Plasma Etching," *Appl. Opt.*, vol. 40, pp. 3698-3702, 2001.

[135] E. Gu, H. W. Choi, C. Liu, C. Griffin, J. M. Girkin, I. M. Watson, M. D. Dawson, G. McConnell and A. M. Gurney, "Reflection/transmission Confocal Microscopy Characterization of Single Crystal Diamond Microlens Arrays," *Appl. Phys. Lett.*, vol. 84, pp. 2754-2756, 2004.

[136] H. Nishiyama, J. Nishii, M. Mizoshiri, and Y. Hirata, "Microlens Arrays of High-refractive-index Glass Fabricated by Femtosecond Laser Lithography," *Appl. Surface Sci.*, vol. 255, 9750-9753, 2009.

[137] C.-F. Chen, S.-D. Tzeng, H.-Y. Chen, and S. Gwo, "Silicon Microlens Structures Fabricated by Scanning-probe Gray-scale Oxidation," *Opt. Lett.*, vol. 30, pp. 652-654, 2005.

[138] Y.-S. Kim, J. Kim, J.-S. Choe, Y.-G. Rob, H. Jeon, and J. C. Woo, "Semiconductor Microlenses Fabricated by One-Step Wet Etching," *IEEE Photonics Tech. Lett.*, vol. 12, pp. 507-509, 2000.

[139] W. N. Carr, and G. E. Pittman, "One-watt GaAs p-n Junction Infrared Source," *Appl. Phys. Lett.*, vol. 3, pp. 173-175, 1963.

[140] V. A. Nemchinsky, "Size and Shape of the Liquid Droplet at the Molten Tip of an Arc Electrode," *J. Phys. D: Appl. Phys.*, vol. 27, pp. 1433-1442, 1994.

[141] *AZ4620 Photoresist Material Safety Data Sheet*, HOECHST CELANESE Corporation.

[142] J. G. Speight, *Lange's Handbook of Chemistry*, 16th ed. New York: McGraw-Hill, 2005, pp. 226–230, 272-286.

[143] J. C. Butcher, *Numerical Methods for Ordinary Differential Equations*, 2nd ed. (John Wiley & Sons, West Sussex, England), pp. 90, 2003.

[144] M. N. Yoder, "Ohmic contacts in GaAs," *Solid-State Electronics*, vol. 23, pp. 117-119, 1980.

[145] N. F. Masse, A. R. Adams, and S. J. Sweeney, "Experimental Determination of the Band Gap Dependence of Auger Recombination in InGaAs/InP Multiple Quantum Well Lasers at Room Temperature," *Appl. Phys. Lett.*, vol. 90, p. 161113, 2007.

[146] U. Strauss, W. W. Rühle, and K. Köhler, "Auger Recombination in Intrinsic GaAs, " *Appl. Phys. Lett.*, vol. 62, pp. 55-57, 1993.

APPENDIX I

BASIC MODLES AND NUMERICAL IMPLEMENTATIONS FOR SOLAR CELL SIMULATION

In the numerical simulation of electronic devices, the main goal is to calculate the position dependent carrier concentration and potential inside the device under certain electrical and optical bias conditions. The most accurate way to solve this problem is to directly solve the n-body Schrödinger equation [93], which is rather challenging and beyond the scope of this work. Therefore, a semi-classical approach based on the Boltzmann Transport Equation (BTE) is used instead.

However, directly solving BTE is still difficult and various approximations can be made to simplify the calculations, resulting in drift-diffusion (DD) and energy balance models. In any of these simplified models, three types of coupled differential equations are derived and form the basic physics in device simulation including, Poisson's equation, continuity equation and transport equation [93]. Then these equations are discretized and solved self consistently using various numerical schemes.

Among these simplified models, the DD model is the easiest to implement, which is good for conventional devices down to 0.5 μm [93]. For smaller devices, the energy balance model is needed, where the carrier temperature or average carrier energy is quite different from the lattice temperature [92]. In this work, the DD model is adopted to simulate the p-n junction solar cell and the

three groups of coupled differential equations are discussed in detail as follows.

The first one is the Poisson's equation, which relates the electrostatic potential inside the device with charge density and is given as [92]

$$\nabla \bullet \left(\varepsilon \nabla V \right) = -q\left(p - n + N_D^+ - N_A^- \right) \quad , \tag{I.1}$$

where ε is the local permittivity, V is the electrostatic potential, q is the absolute value of electron charge, p is the hole density, n is the electron density, N_D^+ is the ionized donor density, N_A^- is the ionized acceptor density. The second one is the continuity equation based on DD model for electrons and holes given as [92]

$$\frac{\partial n}{\partial t} = \frac{1}{q}\nabla \bullet \overrightarrow{J_n} + G_n - R \quad , \tag{I.2}$$

$$\frac{\partial p}{\partial t} = -\frac{1}{q}\nabla \bullet \overrightarrow{J_p} + G_p - R \quad , \tag{I.3}$$

where $\overrightarrow{J_n}$, G_n, R_n are electron current density, generation rate and recombination rate, respectively. $\overrightarrow{J_p}$, G_p, R_p are hole current density, generation rate and recombination rate, respectively. The continuity equation describes the particle conservation law. The last one is the transport equation for electrons and holes given as [92]

$$\overrightarrow{J_n} = qn\mu_n \nabla V + qD_n \nabla n \quad , \tag{I.4}$$

$$\overrightarrow{J_p} = qp\mu_p \nabla V - qD_p \nabla p \quad , \tag{I.5}$$

where μ_n and D_n are electron mobility and diffusion coefficient, respectively. μ_p and D_p are hole mobility and diffusion coefficient, respectively. In the case of small deviation from equilibrium, Einstein relation can be used to related the mobility and diffusion coefficient given as [92]

$$D_n = \frac{kT_L}{q}\mu_n \quad , \tag{I.6}$$

$$D_p = \frac{kT_L}{q}\mu_p \quad , \tag{I.7}$$

where T_L is the lattice temperature, k is the Boltzmann constant. It can be seen that the right hand side of Eq. I.4 and I.5 describes the driving force for the current. Moreover, this driving force can be empirically attributed to the drift and diffusion part caused by electric field and carrier density gradient, respectively.

Equations I.1 to I.5 provide the general framework for device simulation. Moreover, carrier statistical relations are also needed to relate various quantities with carrier concentration. Equations are needed to specify particular physical models for generation and recombination, which can be included in the calculation as needed through the generation and recombination terms in Eq. I.2 and I.3. In the solar cell simulation, the Shockley-Reed-Hall (SRH) recombination, radiative recombination and optical generation are included.

These secondary equations are discussed in detail as follows.

Inside a semiconductor material, carrier statistical properties are governed by the carrier distribution function, which describes the probability of finding a carrier with momentum $\vec{k}$, at position $\vec{r}$ at time t. Various moments of the distribution function give the carrier density, current density, energy density, etc [93]. In practice, approximations are usually made to the distribution function and two approaches are commonly used, namely quasi-Fermi level and displaced-Maxwellian approximations. In this work, the quasi-Fermi level approach is adopted. The basic idea is that the carrier distribution under small deviations from equilibrium can be described by the equilibrium carrier distribution from either Boltzmann or Fermi-Dirac statistics. But the chemical potential or Fermi level for each carrier type is shifted and called quasi-Fermi level.

Assuming Boltzmann statistics, the expression for carrier density under non-equilibrium condition is given as [92]

$$n = n_{ie} \exp\left[\frac{q(V-\phi_n)}{kT_L}\right] \quad , \tag{I.8}$$

$$p = n_{ie} \exp\left[\frac{q(\phi_p - V)}{kT_L}\right] \quad , \tag{I.9}$$

where ϕ_n and ϕ_p are electron and hole quasi-Fermi levels, respectively. n_{ie}

is the intrinsic carrier concentration given as [92]

$$n_{ie} = \sqrt{N_C N_V} \exp\left(\frac{-E_g}{2kT_L}\right) \quad , \tag{I.10}$$

where E_g is the energy bandgap. N_C and N_V are the effective density of states for conduction and valence bands, respectively. The effective density of state can be expressed as [92]

$$N_C = 2\left(\frac{2\pi m_e^* kT_L}{h^2}\right)^{3/2} \quad , \tag{I.11}$$

$$N_V = 2\left(\frac{2\pi m_h^* kT_L}{h^2}\right)^{3/2} \quad , \tag{I.12}$$

where m_e^* and m_h^* are electron and hole effective mass, respectively. Although the calculations are simplified by using Boltzmann statistics, Fermi-Dirac statistics is necessary when the carrier concentration is high.

The SRH recombination is due to the transitions of carriers to the defect levels within the forbidden gap of the semiconductor and usually dominates the recombination is solar cells. It can be described as [92]

$$R_{SRH} = \frac{pn - n_{ie}^2}{\tau_{p0}\left[n + n_{ie}\exp\left(\frac{E_t - E_i}{kT_L}\right)\right] + \tau_{n0}\left[p + n_{ie}\exp\left(\frac{E_i - E_t}{kT_L}\right)\right]} \quad , \tag{I.13}$$

where τ_{p0} and τ_{n0} are hole and electron lifetimes, which can be defined by the user. E_i is the intrinsic Fermi level. E_t is the defect energy level and is

usually set to E_i corresponding to the most efficient recombination center.

Radiative recombination is another important recombination mechanism for direct bandgap solar cells. It is given as [92]

$$R_{Radiative} = B\left(np - n_{ie}^2\right) \quad , \tag{I.14}$$

where B is the radiative recombination coefficient. In the simulation, photon recycling is not considered, which means photons generated by radiative recombination are considered as loss.

Optical generation is responsible for producing photo current and is given as [92]

$$G = \eta_0 \frac{P\lambda}{hc} \alpha e^{-\alpha y} \quad , \tag{I.15}$$

where η_0 is the number of electron-hole pairs generated per absorbed photon, λ is the wavelength, h is the Planck constant, c is the speed of light, α is the absorption coefficient. P is the ray intensity factor, which contains the cumulative effects of reflection, transmission, and loss due to absorption over the ray path.

The above equations are sometimes strongly coupled and a numerical scheme is needed to solve them self consistently. This includes: i) meshing, ii) discretization, and iii) iterative scheme. Silvaco produces numerical solutions to the above equations by firstly defining a mesh of points within the device

structure. Then the equations are discretized and the values of unknowns on the meshing points are calculated iteratively. In the limit of small separations between meshing points, the calculation results should approximately recover the original continuous situation. The specification of meshes involves a trade-off between calculation accuracy and speed. In practice, more meshing points are usually attributed to areas where physical quantities change rapidly and less points to areas where physical quantities change slowly to achieve both faster convergence and better accuracy [92]. This usually leads to non-uniform meshing and care must be taken to insure the conservation of the physical quantities such as, carrier number, current, generation rate, etc.

After meshing and discretization are defined in the device, iteration techniques are usually used to solve the equations since they are usually coupled together. Among all the iteration approaches, Gummel, Newton and Block methods are adopted in Silvaco [92]. Gummel's method solves the coupled Eq. I.1 to I.5 via a decoupled procedure, where Eq. I.1 to I.5 are solved one by one during each Gummel iteration. When solving a particular equation, only one variable is solved while the other variables are kept constant. After one round of iteration is finished, the updated values of the variables are substituted back into the equations to start another round of iteration. The iteration stops after the

values of variables are stable enough to meet the calculation tolerance. The Gummel iteration typically converges slowly, but it often tolerates poor initial guess [92]. The default in Silvaco is the Newton's method, which is a coupled procedure that solves the equations simultaneously. One round of Newton iteration typically involves one matrix inversion and takes longer to complete. But usually the convergence is faster if the initial guess is close to the final solution. A Block method is also provided by Silvaco, which solves some of the equations fully coupled, while the others decoupled. In practice, sometimes it is useful to run a few rounds of Gummel iteration to get a good initial guess and then switch to Newton method for faster convergence.

APPENDIX II

MATERIAL PARAMETERS FOR SOLAR CELL SIMULATION

Table II.1. Effective masses and room temperature Γ valley bandgaps for selected II-VI and III-V binary compound semiconductors [71].

	Electron effective mass (m_e / m_o)	Heavy-hole effective mass (m_{hh} / m_o)	Light-hole effective mass (m_{lh} / m_o)	Room temperature Γ valley bandgap energy E^{Γ}_{g} (eV)
CdSe	0.119	0.57	0.11	1.664
CdTe	0.09	0.82	0.145	1.531
ZnSe	0.13	0.82	0.154	2.698
ZnTe	0.117	0.67	0.159	2.295
AlAs	0.124	0.81	0.16	3.099
AlSb	0.14	0.9	0.13	2.386
GaAs	0.063	0.55	0.083	1.424
GaSb	0.039	0.37	0.043	0.726

Table II.2. Bandgap bowing parameters for selected ternary compounds.

	b_g (eV)		b_g (eV)
ZnCdTe	0.44 [71]	AlAsSb	0.8 [99]
ZnCdSe	0.51 [71]	AlGaAs	0.37 [99]
CdSeTe	0.94 [71]	AlGaSb	$- 0.044 + 1.22x_{Al}$ [99]
ZnSeTe	1.23 [71]	GaAsSb	1.43 [99]

Table II.3. Low field mobility and SRH lifetime for selected II-VI and III-V binary compound semiconductors [71].

	Electron low field mobility μ_n ($cm^2/(V \cdot s)$)	Hole low field mobility μ_p ($cm^2/(V \cdot s)$)	Electron SRH lifetime τ_n (s)	Hole SRH lifetime τ_p (s)
CdSe	900	50	1×10^{-7} *	1×10^{-7} *
CdTe	1050	104	1×10^{-7} *	1×10^{-7} *
ZnSe	1500	250	1×10^{-7} *	1×10^{-7} *
ZnTe	600	100	1×10^{-7} *	1×10^{-7} *
AlAs	294	105	1×10^{-7} *	1×10^{-7} *
AlSb	200	420	1×10^{-7} *	1×10^{-7} *
GaAs	1750	322	5×10^{-9}	1×10^{-8}
GaSb	2800	1150	1×10^{-7}	5×10^{-9}

* These values are difficult to find, therefore a general number is assumed.

Table II.4. Radiative and Auger recombination coefficients for selected II-VI and III-V binary compound semiconductors.

	Radiative recombination coefficient B (cm^3/s)	Auger recombination coefficient C (cm^6/s)
CdSe	1×10^{-10} *	1×10^{-10} *
CdTe	1×10^{-10} *	1×10^{-10} *
ZnSe	1×10^{-10} *	1×10^{-10} *
ZnTe	1×10^{-10} *	1×10^{-10} *
AlAs	1×10^{-10} *	1×10^{-10} *
AlSb	1×10^{-10} *	1×10^{-10} *
GaAs	7.2×10^{-10} [71]	1×10^{-30} [71]
GaSb	1×10^{-10} *	1×10^{-10} *

* These values are difficult to find, therefore a general number is assumed.

Table II.5. Extinction coefficient for selected II-VI binary compounds [100].

CdSe		CdTe		ZnSe		ZnTe	
Photon energy (eV)	Extinction coefficient	Photon energy (eV)	Extinction coefficient	Photon energy (eV)	Extinction coefficient	Photon energy (eV)	Extinction coefficient
2.96	0.63	2.81	0.673	4.021	0.7	3.57	1.7
2.86	0.606	2.71	0.636	3.921	0.62	3.47	1.35
2.76	0.581	2.61	0.5805	3.821	0.54	3.37	1.05
2.66	0.55	2.51	0.525	3.721	0.46	3.27	0.75
2.56	0.5345	2.41	0.38	3.621	0.38	3.17	0.62
2.46	0.512	2.31	0.34	3.521	0.3	3.07	0.5
2.36	0.493	2.21	0.3	3.421	0.29	2.97	0.42
2.26	0.479	2.11	0.2805	3.321	0.27	2.87	0.34
2.16	0.482	2.01	0.261	3.221	0.25	2.77	0.26
2.06	0.433	1.91	0.238	3.121	0.23	2.67	0.23
1.96	0.342	1.81	0.288	3.021	0.21	2.57	0.21
1.86	0.262	1.71	0.338	2.921	0.19	2.47	0.19
1.76	0.2405	1.61	0.185	2.821	0.17	2.37	0.16
1.66	0.17	1.51	0.125	2.721	0.16	2.27	0.14
1.56	3.70E-05	1.41	5.00E-05	2.621	0.000151	2.17	5.00E-05
1.46	7.00E-06	1.31	5.00E-05	2.521	9.00E-05	2.07	5.00E-05
1.36	7.00E-06	1.21	5.00E-05	2.421	8.16E-05	1.97	5.00E-05
1.26	7.00E-06	1.11	5.00E-05	2.321	6.38E-05	1.87	5.00E-05
1.16	7.00E-06	1.01	5.00E-05	2.221	4.45E-05	1.77	5.00E-05
1.06	7.00E-06	0.91	5.00E-05	2.121	2.33E-05	1.67	5.00E-05

Table I.6. Extinction coefficient for selected III-V binary compounds [100].

AlAs		AlSb		GaAs		GaSb	
Photon energy (eV)	Extinction coefficient	Photon energy (eV)	Extinction coefficient	Photon energy (eV)	Extinction coefficient	Photon energy (eV)	Extinction coefficient
4.31	2.52	3.57	2.81	2.73	0.789	2.024	1.378
4.21	2.63	3.47	2.69	2.63	0.595	1.924	1
4.11	2.68	3.37	2.64	2.53	0.476	1.824	0.65
4.01	2.49	3.27	2.69	2.43	0.398	1.724	0.5
3.91	2.15	3.17	2.47	2.33	0.337	1.624	0.43
3.81	1.3	3.07	2.12	2.23	0.294	1.524	0.36
3.71	0.752	2.97	1.97	2.13	0.251	1.424	0.32
3.61	0.519	2.87	2.06	2.03	0.223	1.324	0.3
3.51	0.334	2.77	1.58	1.93	0.187	1.224	0.28
3.41	0.233	2.67	0.92	1.83	0.168	1.124	0.25
3.31	0.139	2.57	0.63	1.73	0.127	1.024	0.22
3.21	0.115	2.47	0.46	1.63	0.097	0.924	0.2
3.11	0.113	2.37	0.33	1.53	0.085	0.824	0.15
3.01	0.11	2.27	0.24	1.43	0.07	0.724	0.1
2.91	1.00E-02	2.17	1.00E-02	1.33	0.0001	0.624	0.001
2.81	5.00E-05	2.07	0.006	1.23	5.00E-05	0.524	5.00E-05
2.71	5.00E-05	1.97	0.004	1.13	5.00E-05	0.424	5.00E-05
2.61	5.00E-05	1.87	0.003	1.03	5.00E-05	0.324	5.00E-05
2.51	5.00E-05	1.77	5.00E-05	0.93	5.00E-05	0.224	5.00E-05
2.41	5.00E-05	1.67	5.00E-05	0.83	5.00E-05	0.124	5.00E-05

APPENDIX III

MATERIAL PARAMETERS FOR SEMICONDUCTOR LUMINESCENCE DEVICE SIMULATION

There are three materials used in the simulation of semiconductor luminescence refrigeration device, namely $In_{0.202}Ga_{0.798}As$, GaAs, and $Al_xGa_{1-x}As$. For $In_{0.202}Ga_{0.798}As$, the temperature dependent SRH lifetime, bandgap, and electron affinity are listed in Table III.1. It should be noted that the strain effect is included in the calculation of $In_{0.202}Ga_{0.798}As$ bandgap and electron affinity. For GaAs, the temperature dependent SRH lifetimes are listed in Table III.2 and the corresponding values for $Al_xGa_{1-x}As$ are assumed the same. The 300 K Auger recombination coefficients of the three materials are listed in Table III.3. All the other parameters for the three materials are taken from the default values provided by Silvaco user manual [92].

Table III.1. Temperature dependent material parameters for $In_{0.202}Ga_{0.798}As$.

Temperature T (K)	SRH lifetime τ (s)	Γ valley bandgap energy E^{Γ}_{g} (eV)	Electron affinity χ_e (eV)
150	2.9×10^{-7} [33]	1.272 [118]	4.138 [118]
200	1.1×10^{-7} [33]	1.254 [118]	4.147 [118]
250	4.4×10^{-8} [33]	1.235 [118]	4.156 [118]
300	2.5×10^{-8} [33]	1.216 [118]	4.165 [118]

Table III.2. Temperature dependent SRH lifetimes for GaAs.

Temperature (K)	SRH lifetime (s)
150	2.9×10^{-7} [33]
200	1.1×10^{-7} [33]
250	4.4×10^{-8} [33]
300	2.5×10^{-8} [33]

* The SRH lifetimes of $Al_xGa_{1-x}As$ take are assumed to be the same as GaAs.

Table III.3. Auger recobimation coefficiencts at 300 K.

	Electron Auger recombination coefficient C (cm^6/s)	Hole Auger recombination coefficient (cm^6/s)
$In_{0.202}Ga_{0.798}As$	1.0×10^{-29} [145]	1.0×10^{-29} [145]
GaAs	7.0×10^{-30} [146]	7.0×10^{-30} [146]
$Al_xGa_{1-x}As$	7.0×10^{-30} [*]	7.0×10^{-30} [*]

* The Auger recombination coefficients of $Al_xGa_{1-x}As$ take are assumed to be the same as GaAs.